[illegible]

Environment of Mars, 1988

(NASA-TM-100470) ENVIRONMENT OF MARS, 1988 N89-14187
(NASA) 71 p CSCL 03B

Unclas
G3/88 0183469

October 1988

NASA

NASA Technical Memorandum 100470

Environment of Mars, 1988

David Kaplan, Compiler
Lyndon B. Johnson Space Center
Houston, Texas

U.S. Geological Survey
Flagstaff, Arizona

ORIGINAL PAGE
COLOR PHOTOGRAPH

Acknowledgements

Many individuals have contributed their scholarly knowledge to this document. In particular, it is a pleasure to acknowledge the contributions of Dr. David E. Pitts (NASA/Lyndon B. Johnson Space Center), Dr. Henry J. Moore (U.S. Geological Survey), Dr. Bruce M. Jakosky (University of Colorado), Dr. Richard W. Zurek (Jet Propulsion Laboratory), and Dr. Christopher P. McKay (NASA/Ames Research Center).

In addition, the document has been enhanced through the review of preliminary drafts by several persons who contributed comments and corrections. In particular, gratitude is expressed to Dr. Donald G. Rea (Project Manager, Mars Rover and Sample Return; Jet Propulsion Laboratory), Dr. Roger D. Bourke (Mission Design Manager, Mars Rover and Sample Return; Jet Propulsion Laboratory), and Dr. Theodore Sweetser (Mission Design Section; Jet Propulsion Laboratory).

Lastly, this work would not have been possible without the encouragement and assistance of Dr. Michael Carr (Chairman, Mars Rover and Sample Return Science Working Group; U.S. Geological Survey), Mr. Mark K. Craig (Manager, Lunar and Mars Exploration Office; NASA/Lyndon B. Johnson Space Center), and Mr. Ronald C. Kahl (Lead, Mars Rover and Sample Return Project Office; NASA/Lyndon B. Johnson Space Center).

CONTENTS

Section Page

1 INTRODUCTION 1-1
1.1 DOCUMENT REVISION AND CONTROL 1-1

2 MARS ATMOSPHERIC MODEL 2-1
2.1 INTRODUCTION 2-1
2.2 ATMOSPHERIC PROPERTIES 2-1
2.2.1 General 2-1
2.2.2 Atmospheric Composition 2-2
2.3 REVISED COSPAR MODELS 2-2
2.4 VIKING 1 AND VIKING 2 ENTRY MODEL ATMOSPHERES 2-3
2.5 ONE DIMENSIONAL, VERTICAL MODELS FOR DUST AND SEASONAL EFFECTS 2-5
2.5.1 Viking Lander 1, Summer, Low Dust Models 2-6
2.5.2 Viking Lander 2, Winter, Medium Dust Models 2-6
2.5.3 Viking Lander 1, Winter, Medium Dust Models 2-6
2.5.4 Viking Lander 1, Winter, Dust Storm Models 2-7
2.6 ATMOSPHERIC WAVE MODEL 2-8
2.7 WINDS 2-9
2.7.1 Surface Winds 2-9
2.7.2 Wind Velocity Variation with Altitude 2-9
2.7.3 Dust Devils 2-10
2.8 CLOUDS 2-10
2.8.1 Composition and Properties 2-10
2.8.2 Frequency of Occurrence 2-11
2.8.3 Dust in the Atmosphere 2-11
2.9 GREAT DUST STORMS 2-13
2.9.1 Dust Storm Evolution 2-13
2.9.2 Local Dust Storms 2-14
2.10 SOLAR IRRADIANCE AT THE MARS SURFACE 2-14
2.10.1 Solar Ultraviolet Flux at the Mars Surface 2-15
2.11 REFERENCES 2-16

3 MARS SURFACE MODEL 3-1
3.1 INTRODUCTION 3-1
3.2 VIKING LANDING SITES 3-1
3.2.1 General Physical Description 3-1
3.2.2 Chemical Properties of Surface Materials 3-2
3.2.3 Physical Properties of Surface Materials 3-3
3.2.3.1 Drift Material 3-4
3.2.3.2 Crusty to Cloddy Material 3-5
3.2.3.3 Blocky Material 3-5
3.2.3.4 Rocks 3-6
3.2.4 Average Bulk Density 3-8
3.2.5 Dielectric Constants 3-8
3.2.6 Thermal Inertias 3-9
3.2.7 Surface and Soil Temperatures 3-11
3.3 GLOBAL COMPARISONS 3-13
3.3.1 Thermal Model 3-16
3.4 SPECIAL CASES 3-16
3.4.1 Canyons and Valleys 3-16
3.4.2 Blocky Craters and Crater BlockFields 3-16
3.4.3 Sand Dunes 3-16
3.4.4 Lava Flows 3-16
3.4.5 Polar Regions 3-16
3.5 REFERENCES 3-21

PRECEDING PAGE BLANK NOT FILMED

PAGE iv INTENTIONALLY BLANK

Section Page

4 MARS ASTRODYNAMIC MODEL 4-1
4.1 INTRODUCTION 4-1
4.2 GENERAL CONSTANTS 4-1
4.2.1 Time Systems 4-1
4.2.2 Standard Reference Coordinate Systems 4-1
4.2.2.1 Earth Mean Equator and Equinox of 1950.0 (EME50) 4-1
4.2.2.2 Earth Mean Ecliptic and Equinox of 1950.0 (EM050) 4-1
4.2.3 Table of General Constants 4-1
4.2.4 Planetary Ephemerides 4-2
4.2.4.1 Precision Planetary Ephemerides 4-2
4.2.4.2 Analytical Ephemerides of Mars and Earth 4-2
4.3 EARTH MODEL 4-2
4.3.1 Earth Gravitational Field 4-2
4.3.2 Earth Topographic Sites 4-2
4.3.2.1 Launch Site 4-2
4.3.2.2 Deep Space Network Station Sites 4-2
4.4 MARS MODEL 4-2
4.4.1 Shape 4-2
4.4.1.1 Equatorial Radius 4-2
4.4.1.2 Reference Mapping Surface 4-3
4.4.2 Orientations 4-4
4.4.2.1 Mean Orbit Pole 4-4
4.4.2.2 Mean Rotation Pole 4-4
4.4.2.3 Prime Meridian 4-4
4.4.2.4 Rotation Rate 4-4
4.4.3 Gravitational Field 4-5
4.4.3.1 Gravitational Harmonics 4-5
4.4.3.2 Gravity Anomalies 4-5
4.4.4 Martian Time Systems 4-5
4.4.4.1 Martian Seasonal Time 4-5
4.4.4.2 Martian Solar Time 4-5
4.5 MARTIAN SATELLITES 4-6
4.5.1 Phobos and Deimos Physical Data 4-6
4.5.2 Satellite Ephemerides 4-7
4.6 COORDINATE SYSTEMS 4-7
4.6.1 Introduction 4-7
4.6.2 Mars-Centered Coordinate Systems 4-8
4.6.2.1 Mars Equator and Equinox of Epoch 4-8
4.6.2.2 Mars Equator and Prime Meridian of Date 4-8
4.6.2.3 Mars Mean Equator and IAU-Vector of Epoch (or Date) 4-9
4.6.2.4 Areographic Coordinate System 4-9
4.6.2.5 In-Orbit Radial-Crosstrack-Downtrack System 4-9
4.6.3 Spacecraft-Centered Reference System 4-9
4.6.3.1 Orbital Phases Nadir Coordinate System 4-9
4.7 REFERENCES 4-10

FIGURES

Figure		Page
2-1	Surface pressure versus time for Viking landers 1 and 2 (Tillman, 1988)	2-2
2-2	Comparison of atmospheric density for the revised COSPAR Northern Hemisphere mean Mars model and the 1962 U.S. Standard Earth atmosphere	2-4
2-3	Comparison of atmospheric temperature for the revised COSPAR Northern Hemisphere mean Mars model (with an extension above 100 km using Stewart's model) and the 1962 U.S. Standard Earth atmosphere	2-4
2-4	Percent atmosphere density deviations of the revised COSPAR low-cool model and the revised COSPAR high-warm model as compared with the revised COSPAR Northern Hemisphere mean model	2-5
2-5	Comparison of atmosphere temperature structure of the COSPAR low-cool and COSPAR high-warm models with extension above 100 km provided by Stewart's model	2-5
2-6	Percent atmospheric density deviations of the Viking 1 entry conditions as compared with the revised COSPAR Northern Hemisphere mean model	2-6
2-7	Percent atmospheric density deviations of the Viking 2 entry conditions as compared with the revised COSPAR Northern Hemisphere mean model	2-6
2-8	Morning and afternoon density profiles calculated by Pollack for VL-1 location during the summer for optical depth = 0.25	2-7
2-9	Morning and afternoon density profiles calculated by Pollack for VL-2 location during the winter for optical depth = 0.5	2-7
2-10	Morning and afternoon density profiles calculated by Pollack for VL-1 location during the winter for optical depth = 0.5	2-7
2-11	Morning density profile calculated by Pollack for VL-1 location during winter for optical depth = 5.0	2-8
2-12	Afternoon density profile calculated by Pollack for VL-1 location during the winter for optical depth = 5.0	2-8
2-13	Temperature and wind structure of the wintertime NorthernHemisphere (Hanel et al., 1972)	2-10
2-14	Optical depth as measured for Viking landers 1 and 2 as a function of areocentric longitude (L_s); Zurek, 1982	2-12
2-15	A comparison of the radiation incident on the martian atmosphere and at the surface for 50° N spring and 50° N winter (Kuhn and Atreya, 1979)	2-15
2-16	Latitudinal distribution of daily solar radiation at various wavelengths reaching the martian surface (Kuhn and Atreya, 1979)	2-15
3-1	Photographs illustrating surface materials at the Viking landing sites	3-4
3-2	VL-1 photographs illustrating relative strengths of blocky and drift materials	3-7
3-3	Model relation between dielectric constant or quasi-specular echo reflectivity and bulk density	3-10
3-4	Daily maximum, minimum, and average surface temperatures at the two Viking landing sites through a martian year.(Kieffer, 1976)	3-12
3-5	Temperatures for the soils at the Viking lander sites	3-12
3-6	Correlation between quasi-specular echo reflectivity (and dielectric constant) and thermal inertia	3-14
3-7	Diurnal surface temperature mean and extremes for the primaryViking thermal model (Kieffer et al., 1977)	3-17
3-8	Profile of Ius Chasm (Moore, 1988)	3-20
4-1	IAU specification of prime meridian	4-5
4-2	Hour angle of equinox for specifying prime meridian	4-5
4-3	Longitude of Sun (L_s)	4-6
4-4	Local true solar time	4-7
4-5	Local mean solar time definition	4-8
4-6	Mars mean equator and IAU-vector of Epoch coordinate system	4-9
4-7	Areographic coordinate system	4-9
4-8	In-orbit radial-crosstrack-downtrack coordinate system	4-9
4-9	Nadir coordinate system	4-10

TABLES

Table Page

2-1 COMPOSITION OF THE ATMOSPHERE OF MARS 2-2
2-2 VIKING ENTRY GROUND TRACKS 2-4
2-3 ZONAL WIND CUMULATIVE PROBABILITIES VERSUS SEASON (m/sec, + from West) 2-9
2-4 MERIDIONAL WIND CUMULATIVE PROBABILITIES VERSUS SEASON (m/sec, + from South) 2-9
2-5 MARTIAN GREAT DUST STORMS (Zurek, 1982) 2-14

3-1 ESTIMATED MECHANICAL PROPERTIES AND REMOTE SENSING SIGNATURES OF THE SURFACE MATERIALS IN THE SAMPLE FIELDS AT THE VIKING LANDING SITES 3-3

4-1 TABLE OF GENERAL CONSTANTS 4-3
4-2 ANALYTIC EPHEMERIDES OF EARTH AND MARS 4-4
4-3 COORDINATES OF DEEP SPACE NETWORK STATION SITES 4-4
4-4 MARS GRAVITY ANOMALIES AND ERROR ASSESSMENT 4-6
4-5 TABLE OF MARTIAN SEASONS 4-7
4-6 PHYSICAL DATA OF PHOBOS AND DEIMOS 4-8
4-7 ORBIT OF PHOBOS AND DEIMOS 4-8

Viking Lander 1 photograph of Chryse Planitia; camera is facing southeast.

ORIGINAL PAGE
COLOR PHOTOGRAPH

Introduction

This document provides a compilation of scientific knowledge about the planet Mars. The most recent references available have been collected, reviewed, and incorporated. Comprehensive descriptions are given of the atmosphere of Mars, the surface of Mars, and the astrodynamics of Mars.

The materials presented herein are not tied to any particular mission, but rather are intended to be a data base for the development of engineering models which support exploration missions to Mars. The document does not, for example, make recommendations as to what type of rock distribution profile a rover vehicle should be designed to encounter. Rather, it presents a compilation of the latest scientific thought concerning the environment of Mars.

1.1 DOCUMENT REVISION AND CONTROL

New information about Mars may be forthcoming in the future from new analysis of previously collected data, from new Earth-based observations, or from future flight missions (American, Soviet, or others). As new information becomes available, it will be incorporated into future versions of this document.

This document was prepared by, and is under the control of, the NASA Lyndon B. Johnson Space Center, Lunar and Mars Exploration Office. It was developed to support the Mars Rover and Sample Return Project Office.

Comments concerning this document should be directed to NASA/Lyndon B. Johnson Space Center; Lunar and Mars Exploration Office; Code IZ3; and marked "ATTN: Mars Environment Model Cognizant Engineer."

ORIGINAL PAGE IS
OF POOR QUALITY

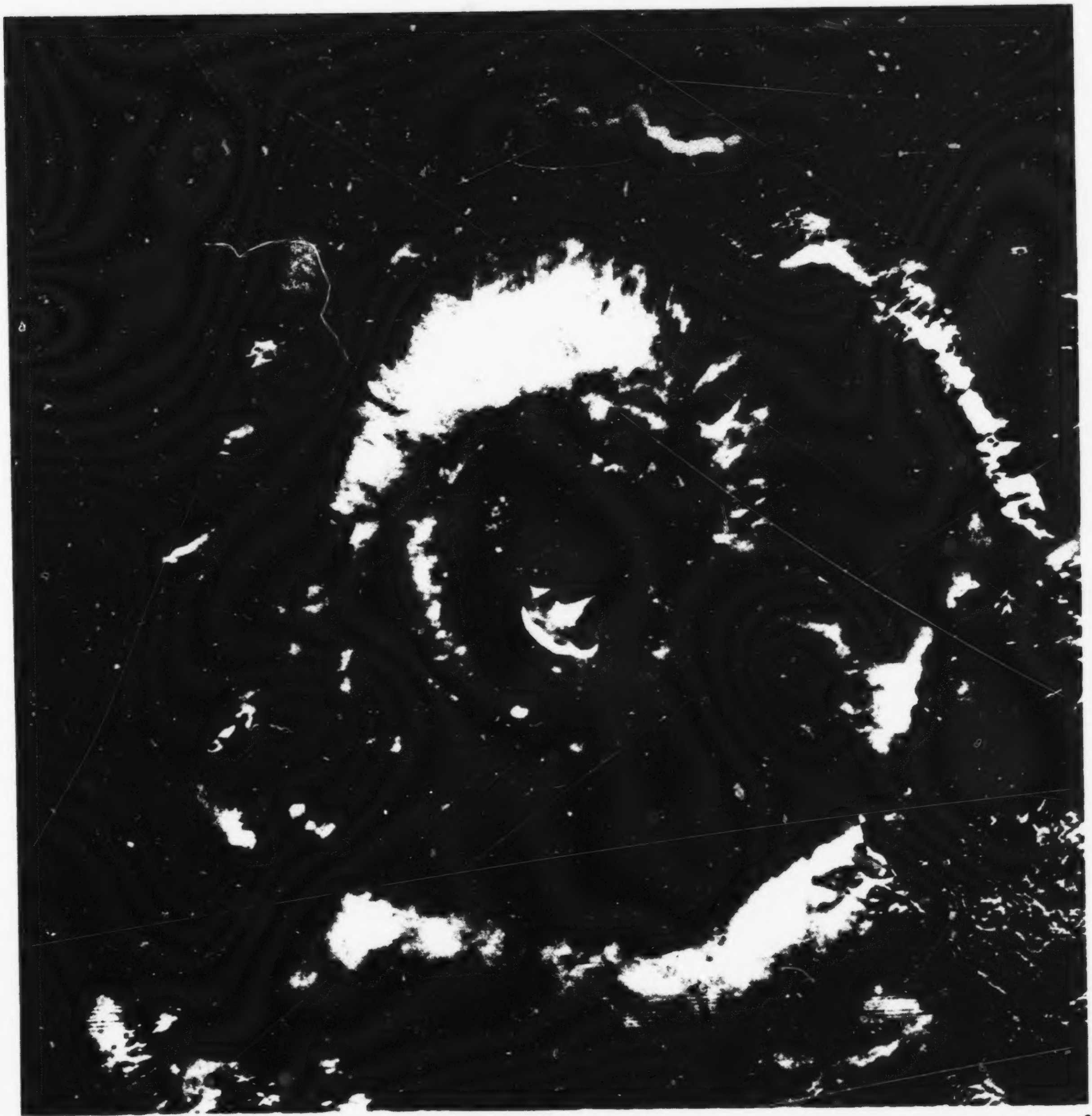

Olympus Mons - single frame;
surface dimensions: 798 km x 899 km

~~PRECEDING PAGE BLANK NOT FILMED~~

ORIGINAL PAGE IS
OF POOR QUALITY

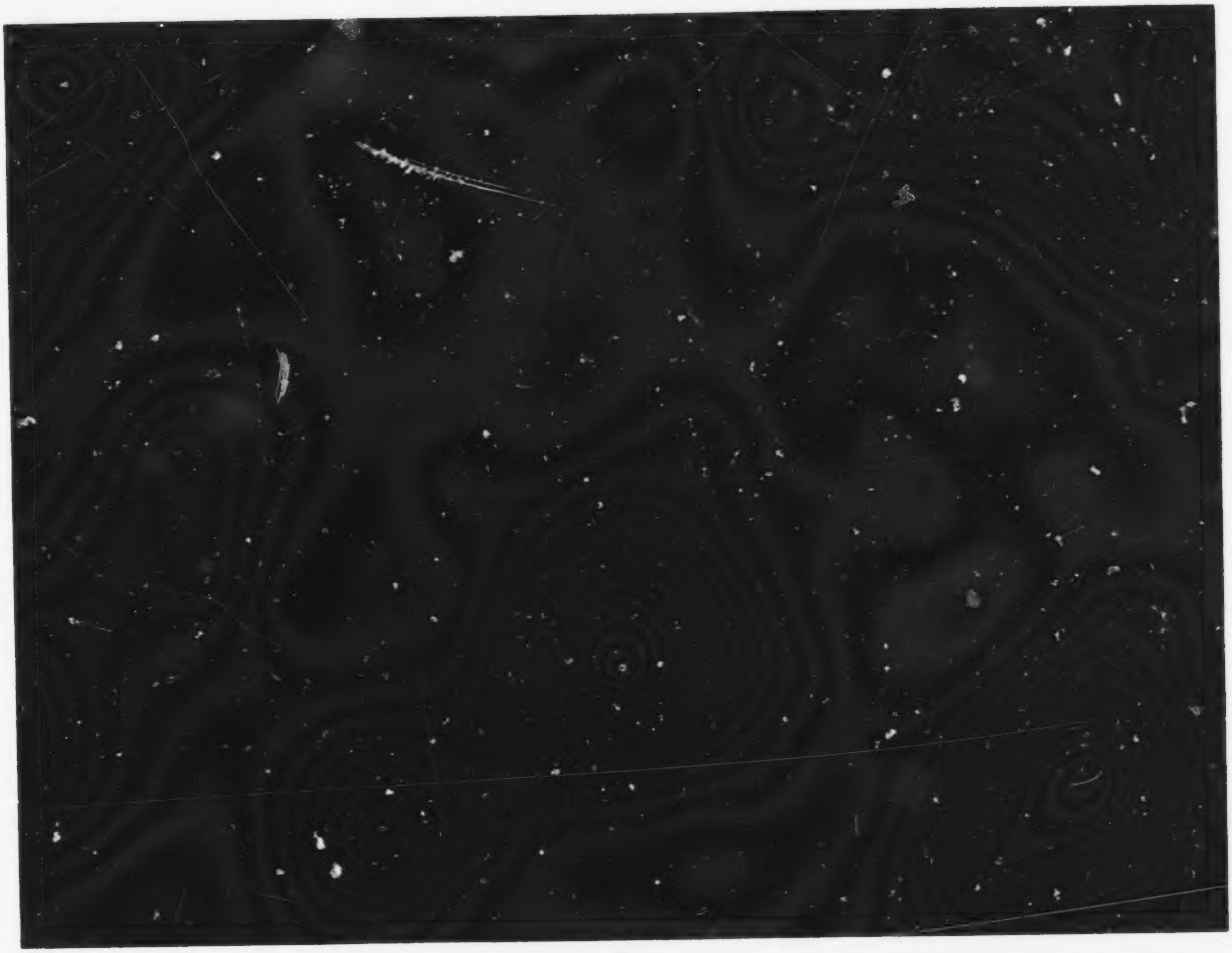

Olympus Mons and surroundings (mosaic)

ORIGINAL PAGE IS
OF POOR QUALITY

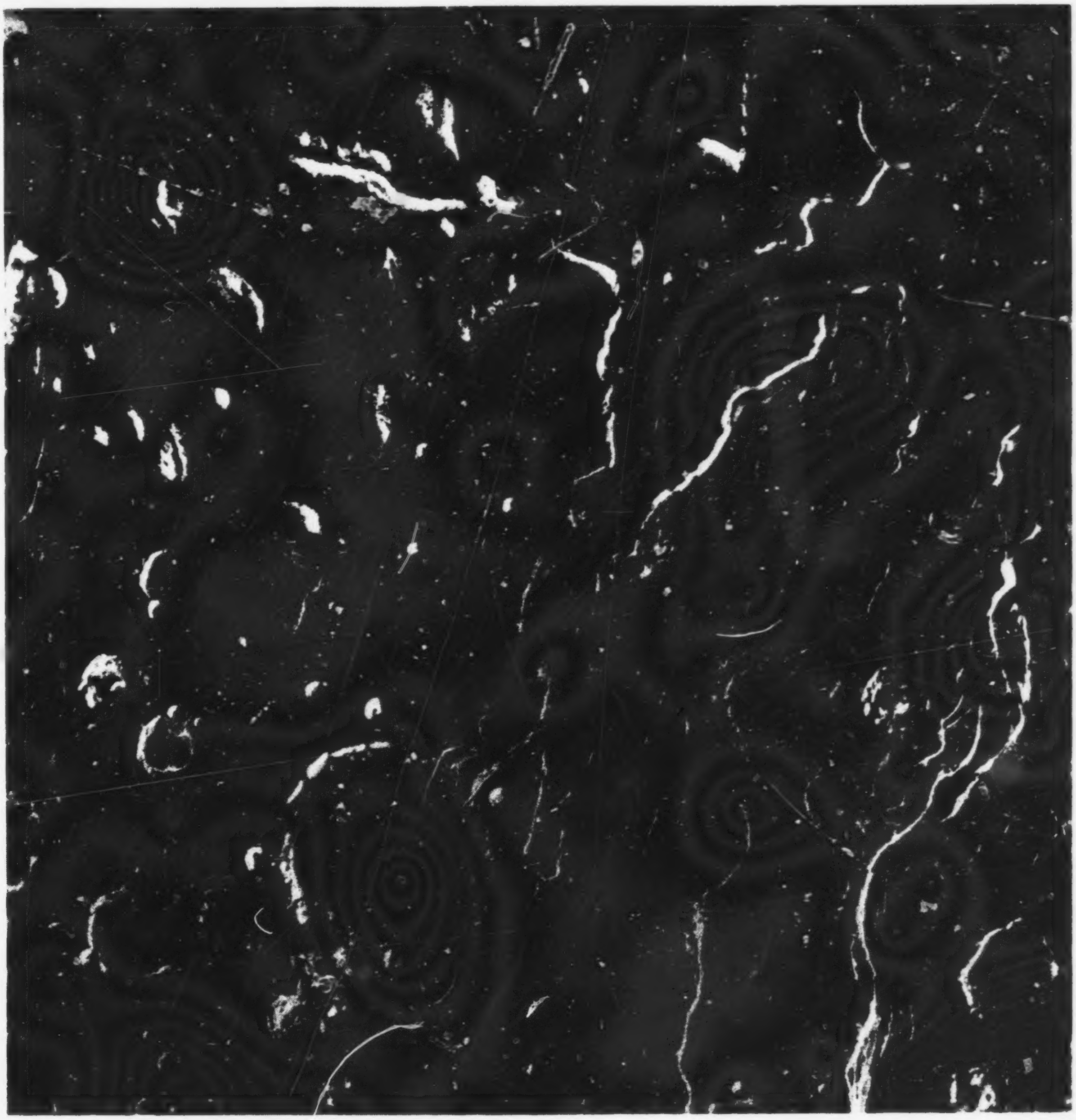

Upper Mangala Vallis;
longitude: 150° W - 155° W
latitude: 2.5° S - 7.5° S

ORIGINAL PAGE IS
OF POOR QUALITY

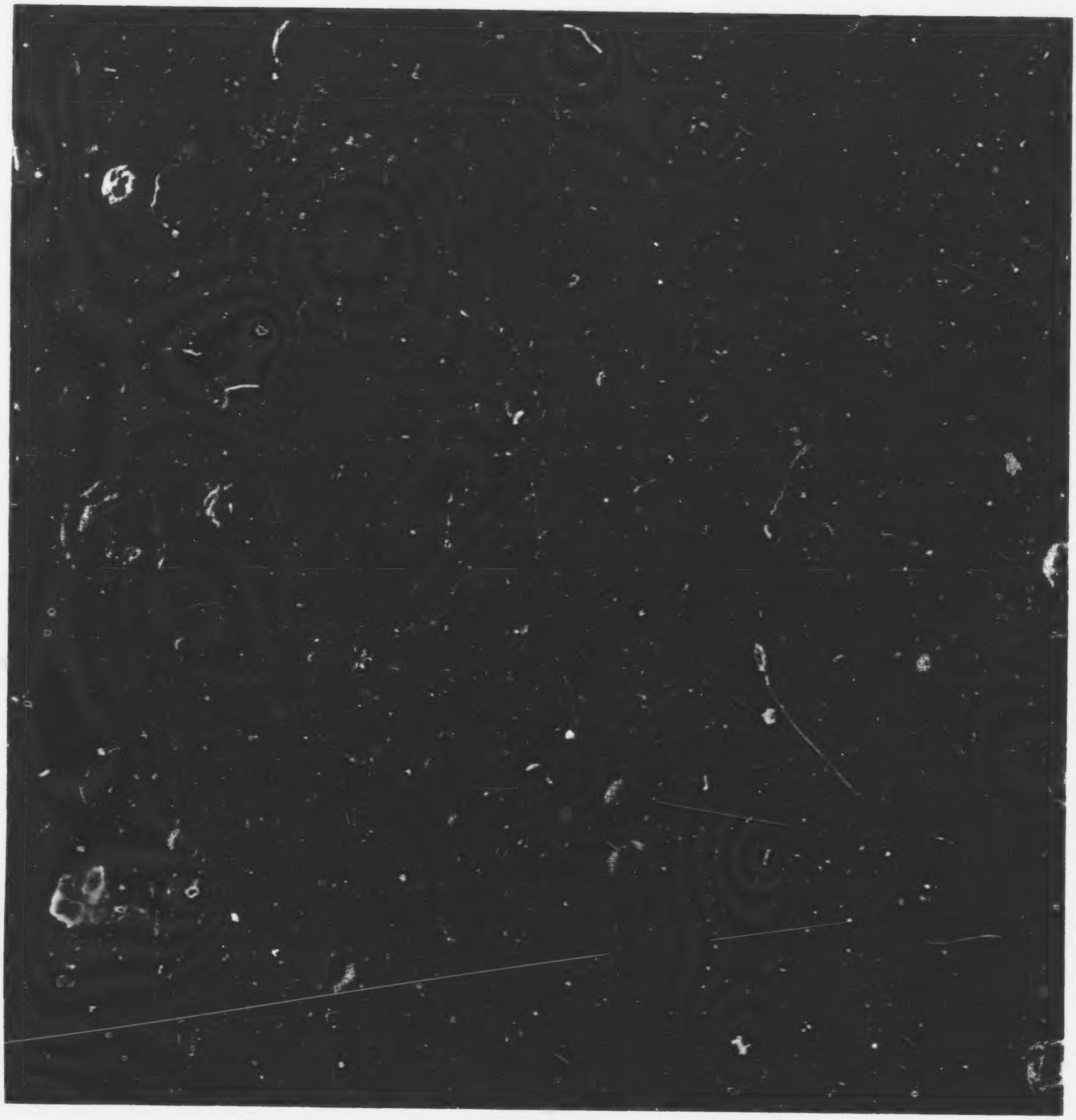

Lower Mangala Vallis;
Longitude: 150° W - 155° W
Latitude: 7.5° S - 12.5° S

ORIGINAL PAGE IS
OF POOR QUALITY

Mars Atmospheric Model[1]

2.1 INTRODUCTION

Model atmospheres are required for engineering design studies of vehicles that operate within or through the atmosphere. Lifetime studies of vehicles on orbit, aerobraking studies of entry vehicles, design of parachute descent systems, design of landers and automated vehicles on the surface, and studies of ascent and rendezvous of vehicles through the atmosphere all require knowledge of the atmospheric structure and dynamics. Atmospheric density is of paramount importance in all regimes since the drag on a vehicle is proportional to the density and the square of the velocity of the vehicle. Dust and cloud particles suspended in the atmosphere can impact and damage high-speed vehicles and can reduce the effectiveness of solar power generation systems. At lower vehicle speeds, atmospheric winds become an important design criteria since they affect factors such as surface operations, parachute descent, and launch.

Because of the highly variable nature of the Mars atmosphere, several model atmospheres are presented here. These model atmospheres are patterned after the 1962, 1966, and 1976 (COESA, 1962; COESA, 1966; COESA, 1972) models of the Earth's atmosphere. Mean, maximum, and minimum models are presented as well as models which address the diurnal, seasonal, dust storm, and latitudinal variability of the Mars atmosphere.

The first models described here are enhancements of the COSPAR models (Seiff, 1982). These will serve as baselines, representing the general range of variability expected for daily-mean, summer, and midlatitude conditions. The second set of models represents the actual entry conditions as measured by Vikings 1 and 2, and provides a testing mechanism for aerobraking systems against the expected wave structure seen in the Viking entries between about 30 km and 100 km. The third set of models represents the diurnal, seasonal, latitudinal, and dust effects present in the Mars atmosphere.

2.2 ATMOSPHERIC PROPERTIES

2.2.1 General[2]

The Mars atmosphere is highly variable on a daily, seasonal and annual basis. The thinness of the atmosphere and solar heating (which is 44 percent of terrestrial values) guarantees a large daily temperature range at the surface under clear conditions. On an annual basis, the atmospheric pressure at the surface changes by ±15 percent due to condensation and sublimation of the CO_2; see figure 2-1.

Since upper atmosphere pressure and density are directly related to changes in the surface pressure, accurate specification of surface pressure is very important. Although (1) Mars atmospheric pressure is approximately 1.0 percent that of Earth, (2) Mars is much colder than Earth, and (3) Mars has no liquid water, nonetheless many of its meteorological features are similar to terrestrial ones. Water-ice clouds are present, and fronts with wind shifts and associated temperature changes similar in nature to those on Earth can be found. The main differences between Earth and Mars atmospheres are that the Mars atmosphere does not transfer as much heat, and it cools much faster by radiation; Mars surface diurnal temperature cycle is larger than Earth's (190 to 240 K during the summer, but stabilized near 150 K (the CO_2 frost point) during the winter); and Mars has local dust storms of at least a few hundred kilometers in extent every year and, in some years, has "great" dust storms which can span most of one or both hemispheres.

Global dust storms, which tend to occur near perihelion, absorb solar radiation high in the atmosphere and thereby both decrease the surface maximum temperature and increase the upper atmospheric temperature. This phenomenon causes large scale expansion of the atmosphere and substantial increases of atmospheric density at orbital and entry altitudes. Also, the decrease in surface temperature causes the surface atmospheric density to increase.

Temperature gradients from equator to pole and the coriolis force tend to cause jet streams to form in middle latitude regions. These jets are larger by a factor of four than the tropospheric jets on Earth. However, the Mars jet streams occur at atmospheric densities two orders of magnitude lower than for Earth, which lowers their importance for vehicle design criteria.

Water ice clouds occur due to many different causes just as on Earth. Nighttime radiation cooling produces fogs; afternoon heating causes updrafts which adiabatically cools the air and causes condensation; clouds form in association with frontal systems; flow over topography causes gravity wave clouds; and cooling in the winter polar region causes clouds.

---

[1] Most materials of part 2 are excerpted from the document "Model Profiles of the Mars Atmosphere for the Mars Rover and Sample Return Mission," by D.E. Pitts, J.E. Tillman, J. Pollack, and R. Zurek, 1988 to be published by NASA as a technical memorandum.

[2] Since there are no oceans on Mars to aid in describing a mean geopotential reference surface, an oblate spheroid describing the 6.1 mbar level in the atmosphere from the Mariner 9 measurements is used for this purpose (Cain et al., 1973). This oblate spheroid has an equatorial radius (re) of 3393.4 km and a polar radius (rp) of 3375.7 km.

2.2.2 Atmospheric Composition

Atmospheric composition on Mars was determined from measurements with the mass spectrometers on the Viking landers (Owen et al., 1977). Table 2-1 describes this composition in terms of the gases present and their mole fraction.

Water vapor abundance was continuously mapped from the Viking orbiters for 1.5 Mars years (Jakosky and Farmer, 1982). Large amounts of water vapor (100 mm, i.e., 100 precipitable micrometers) have been observed over the summer northern polar region, with essentially zero being observed in the winter. There is a net transport from the summer polar cap toward the winter polar cap. Water vapor appears somewhat uniformly mixed with altitude (Davies, 1979a) and the tenuous atmosphere may be near water vapor saturation much of the time (Davies, 1979b).

Ozone amounts range from 57 mm over the polar hood during winter to less than 3 mm during summer (Barth, 1974). (Both ozone and water vapor are likely to be not uniformly mixed with the other atmospheric gases; for this reason, ozone and water vapor are not included in table 2-1.)

Gas	Mole fraction
CO_2	0.955 ± 0.0065
N_2	0.027 ± 0.003
Ar	0.016 ± 0.003
O_2	0.0015 ± 0.005
CO	0.0007
Ne	2.5 ppm
Kr	0.3 ppm
Xe	0.08 ppm

TABLE 2-1.- Composition of the Atmosphere of Mars

2.3 REVISED COSPAR MODELS

The COSPAR warm-high and cool-low models described by Seiff et al., 1982, provide envelopes around the excursions of temperature and density measured by the Viking probes during aerobraking and parachute descent. Although they apply to the Northern Hemisphere summer, the season of the Viking entries, they represent the best

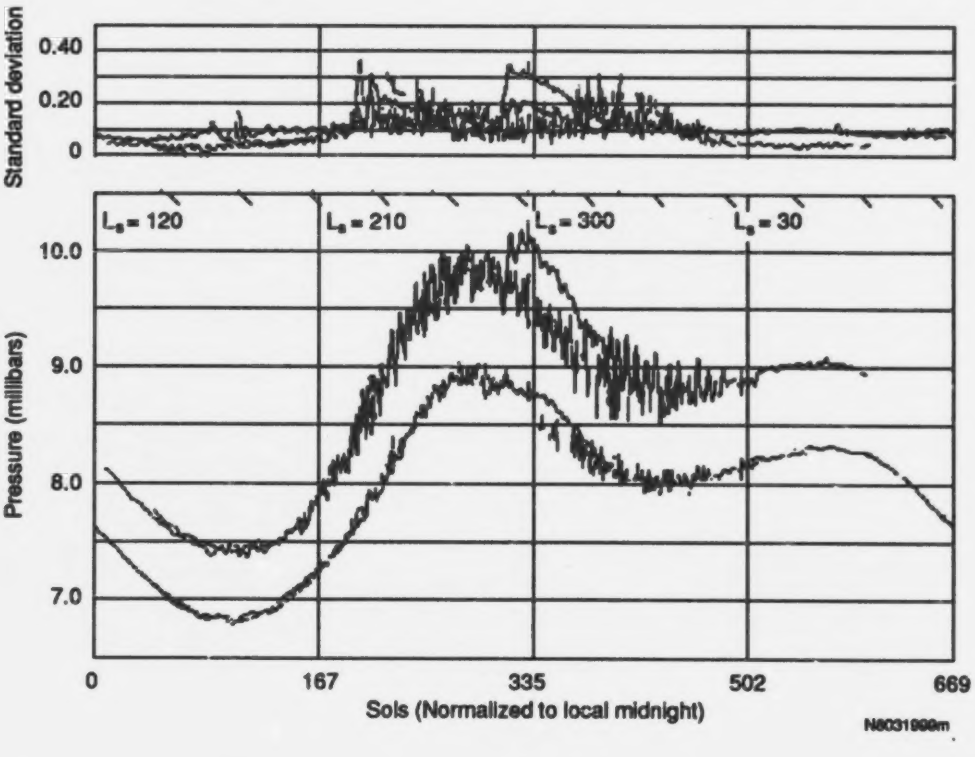

Figure 2-1.- Surface pressure versus time for Viking Landers 1 and 2 (Tillman, 1988).

The lower panel plots the daily average pressure at landers 1 and 2. The difference in pressure between the landers is due to the difference in altitude of the two sites. The upper panel illustrates the standard deviation around the daily average pressure, and is an indicator of weather fronts, dust storms, and global oscillations.

knowledge of the range of temperature and density from near 100 km down to the surface of Mars.

Because of the large amount of relief present on the surface of Mars, the COSPAR models have been extended below the mean aeroid to -5 km, an altitude below that which is appropriate for Hellas (-4.3 km), which is one of the lowest regions on the planet, (Lindal et al., 1979). Relative to the mean aeroid, Viking Lander 1 (VL-1) (23° N, 48° W) sits at -1.5 km and Viking Lander 2 (VL-2) (48° N, 226° W) sits at -2.5 km. (The local radius of the reference ellipsoid, selected for the original COSPAR models (R_o= 3390 km), is also adopted here for the revised COSPAR models. The acceleration due to gravity as calculated for latitude 30° by Seiff et al., 1978, is 372.95 cm/sec^2, and this value is also used for the revised models.)

In order to ensure completeness for entry and orbital decay studies, the COSPAR data are extended above 120 km using the program developed by Stewart, 1987, for orbital lifetime and sustenance studies of the Mars Observer spacecraft. Stewart's model specifies the atmosphere structure above a pressure of 1.24 nbar (1.24 x 10^{-3} dynes/cm^2), usually near 120 km, as a function of latitude, local solar time, and longitude of the Sun with respect to the Mars vernal equinox (Ls, called "areocentric longitude"). The Ls is the predominant cause of changes in the atmospheric density above 100 km since it determines the distance to the Sun which affects the solar flux received by Mars dramatically. The Ls is also indicative of the seasons (which determine the global pressure change due to sublimation of carbon dioxide at the poles), and the onset of the global dust storms which heat the upper stratosphere. Latitude appears to have only a small effect on atmospheric density above the 1.24 nbar level. Only atomic oxygen is known to have a diurnal effect, and this is small compared to the seasonal effects just discussed.

The upper atmosphere is most significantly affected by the ultraviolet radiation from the Sun. The ultraviolet insolation has a greater effect on exospheric temperature and density than does the surface pressure effect. A method for estimating the ultraviolet solar insolation is to measure the solar flux at a wavelength of 10.7 cm. Hence, the 10.7 cm flux is chosen as the parameter of interest in constructing the upper and lower envelopes for the upper regions of the revised COSPAR atmospheres.

In order to provide an envelope of upper atmospheric densities which are consistent with the established COSPAR profiles, extreme condition envelopes are used with Stewart's model. An L_s of 245° is used with the warm-high COSPAR model giving the maximum 10.7 cm solar flux for the Mars orbit under normal solar conditions. This is coupled with +1s (standard deviation) conditions for both long and short-term effects for exospheric temperature, overall oxygen concentration, diurnal oxygen concentration, the altitude of the base of the thermosphere, and the effect of dust in the stratosphere. An L_s of 65° is used with the cool-low COSPAR model giving the minimum 10.7 cm solar flux. This is coupled with -1s conditions in the exosphere, as described previously, to create a lower bounds of atmospheric density for the upper atmosphere. The mean COSPAR model is extended upward with Stewart's baseline upper atmosphere profile using mean conditions above the 1.24 nbar level. These upper atmosphere temperature and molecular weight profiles are added to the COSPAR models to give upper, lower, and mean profiles calculated using the model of Pitts, 1969.

These revised COSPAR models (Mars Northern Hemisphere mean, warm-high, and cool-low) are shown in figures 2-2, 2-3, 2-4, and 2-5.

Appendix C of Pitts et al., 1988, lists the input data for the various atmospheric models. Specifically, table C-I provides temperature and molecular weight distribution as a function of height for the revised COSPAR Northern Hemisphere Mean atmosphere; table C-II lists these input data for the revised COSPAR Cool-Low atmosphere; and table C-III gives the data for the revised COSPAR warm-high atmosphere. Each table also gives the following calculated quantities (as a function of height): pressure, density, speed of sound, density scale height, number density, mean free path, viscosity, pressure scale height, mean particle velocity, collision frequency, and columnar mass. (Appendix A of Pitts et al., 1988 provides a FORTRAN-callable routine which generates these calculated quantities from the input data.)

2.4 VIKING 1 AND VIKING 2 ENTRY MODEL ATMOSPHERES

Seiff and Kirk, 1977, describe the atmospheric measurements made during aerobraking and parachute descent. Accelerometers onboard the landers measured atmospheric density from 120 km down to 26 km. Atmospheric pressure was measured on the aeroshell from 90 km to 6 km, and atmospheric temperature on the aeroshell was measured from 27 km to 6 km. After jettisoning of the aeroshell and deployment of the parachute, pressure and temperature were measured from 6 to 1.5 km and 3.8 to 1.5 km, respectively. These measurements have excellent consistency and provide a description of the northern summer atmosphere of Mars at two latitudes and two local solar times. The Viking 1 entry occurred on July 20, 1976 (L_s = 96°), and the Viking 2 entry occurred on Sept. 3, 1976 (L_s =117°). The entry ground track is described in table 2-2 from the NSSDC[3] Data Set 75-075C-02A and 75-083C-02A.

---

[3] National Space Science Data Center; NASA/Goddard Space Flight Center, Greenbelt, Maryland.

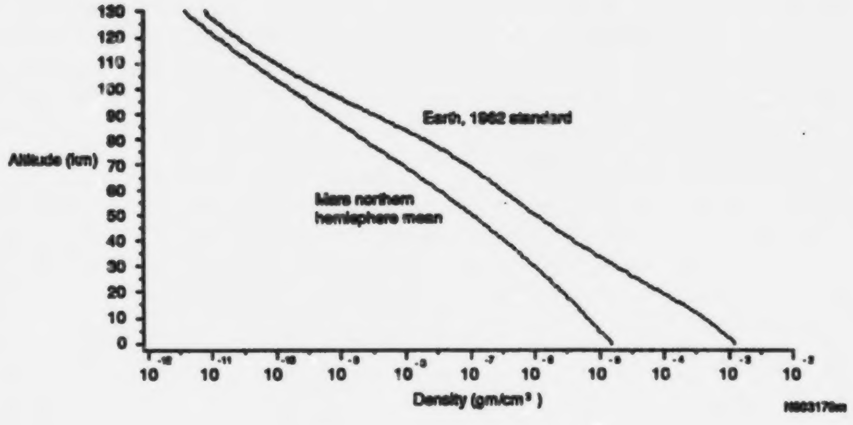

Figure 2-2.- Comparison of atmospheric density for the revised COSPAR Northern Hemisphere mean Mars model and the 1962 U.S. Standard Earth atmosphere.

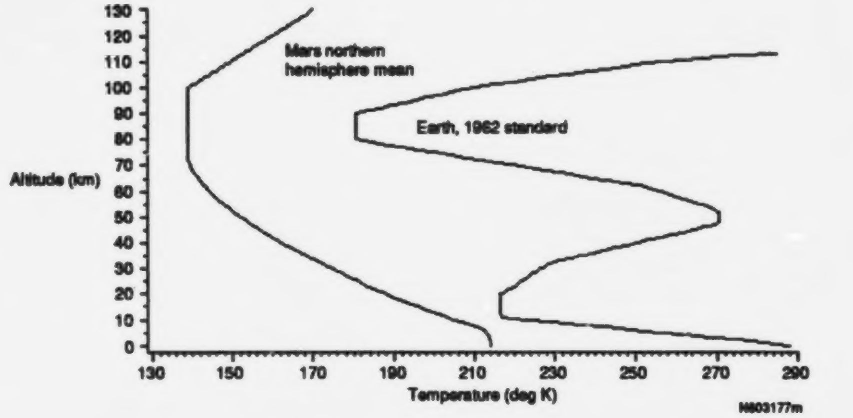

Figure 2-3.- Comparison of atmospheric temperature for the revised COSPAR Northern Hemisphere mean Mars model (with an extension above 100 km using Stewart's model) and the 1962 U.S. Standard Earth atmosphere.

These entry measurements present atmospheric structural details that are averaged out in models describing average conditions, such as the COSPAR models. Yet, some of these details can be very important for vehicle design considerations. Viking temperature profiles (Seiff, 1982) show dramatic oscillatory structure, from approximately 30 km to 120 km, which may cause concern in the design of automated guidance systems for aerobraking.

For altitudes above the Viking accelerometer measurements, data from the neutral gas mass spectrometer (Nier and McElroy, 1977) were used together with Stewart's upper atmosphere model. Viking 1 measurements of an exospheric temperature of 185 K (Nier and McElroy, 1977) were made at an L_s of 96°, when the Solar and Terrestrial Data Service of the National Oceanic and Atmospheric Administration estimated the 10.7 flux to be 28×10^{-22} W/cm². Likewise, during the Viking 2 entry, the Viking measurements gave an exospheric temperature of 135 K at an L_s of 117°, while the Earth-based network measured the 10.7 cm flux to be 32×10^{-22} W/cm². These values for 10.7 cm solar flux, L_s, and exospheric temperatures were used as inputs to Stewart's model for defining temperature and molecular weight structure above the exobase (1.24 nbars).

	Radar altitude (km)	Latitude (deg)	Longitude (deg)
Viking 1	131.7	16.1	-57.24
	26.878	21.0	-49.87
	0.0	22.4	-48
Viking 2	126.93	41.22	-236.79
	28.017	45.99	-229.81
	0.0	47.9	-226.

TABLE 2-2.- Viking entry ground tracks

Figure 2-6 presents percentage atmospheric density deviations of the Viking 1 entry conditions as compared with the revised COSPAR Northern Hemisphere mean model; figure 2-7 presents the same information for the Viking 2 entry conditions.

Appendix C of Pitts et al., 1988, lists the input data for the various atmospheric models. Specifically, table C-IV provides temperature and molecular weight distribution as a function of height for the Viking 1 entry model atmosphere; and table C-V gives the data for the Viking 2 entry model atmosphere. Each table also gives the following calculated quantities (as a function of height): pressure, density, speed of sound, density scale height, number density, mean free path, viscosity, pressure scale height, mean particle velocity, collision frequency, and columnar mass. (Appendix A

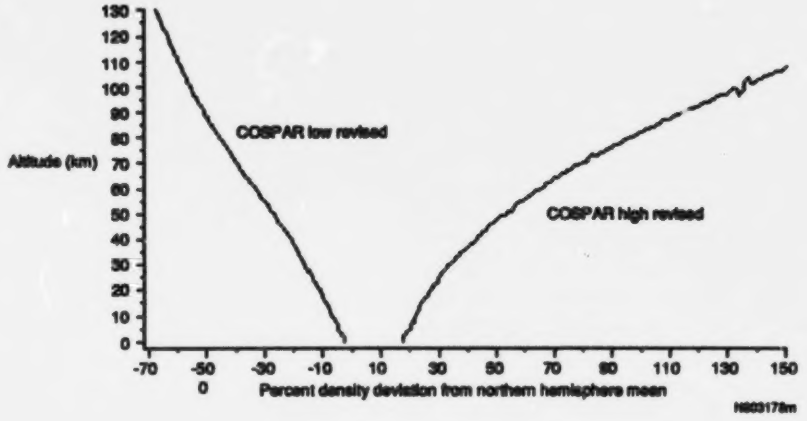

Figure 2-4.- Percent atmosphere density deviations of the revised COSPAR low-cool model and the revised COSPAR high-warm model as compared with the revised COSPAR Northern Hemisphere mean model.

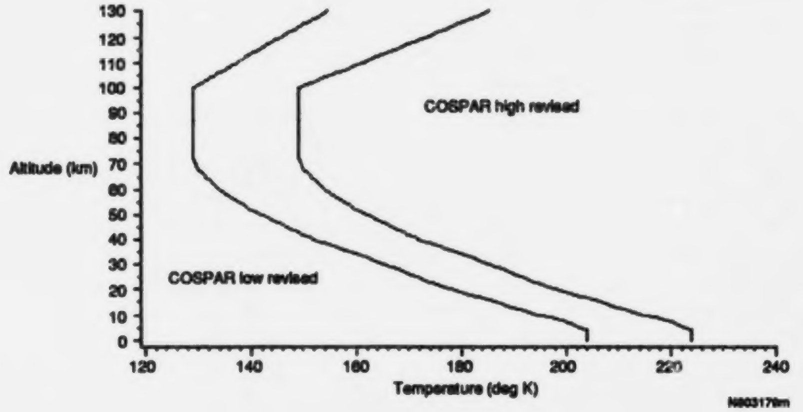

Figure 2-5.- Comparison of atmosphere temperature structure of the COSPAR low-cool and COSPAR high-warm models with extension above 100 km provided by Stewart's model.

of Pitts et al., 1988, provides a FORTRAN-callable routine which generates these calculated quantities from the input data.)

2.5 ONE DIMENSIONAL, VERTICAL MODELS FOR DUST AND SEASONAL EFFECTS

The models described in the following section are included in order to provide the user with a tool to evaluate the importance of seasonal, latitudinal, time of day, and dust storm effects on engineering design. These eight models are the results of one-dimensional circulation computations by Dr. James B. Pollack (Theoretical Studies Branch, NASA/Ames Research Center). They are based on lower boundary conditions at the Viking 1 and 2 lander locations and are calculated for the mean aeroid. Outputs are averaged over longitude and are provided from 0.0 to 80 km geopotential altitude. The models are presented as four pairs, each pair having a morning and afternoon model to allow the user to assess diurnal environmental effects on engineering designs. Because the two landers experienced very similar conditions during Northern Hemisphere summer, only one model pair: Viking 1 summer, low optical depth ($t = 0.25$) is needed. However, during winter, considerable differences were apparent between the latitude of the VL-1 and VL-2, thereby requiring two model pairs to represent medium dust conditions ($t = 0.5$). One global dust storm model pair is presented: VL-1 for ($t = 5.0$). In each case the seasonal surface pressure as measured by the appropriate lander during the first year of data is used in place of the 6.1 mbar at the mean aeroid. Surface pressure changes during the day are not included. In each case, Stewart's upper atmosphere model is utilized above 120 km. Information between 80 km (the upper bound of the Pollack models) and 120 km (the lower bound of the Stewart model) is interpolated.

Tables in appendix C of Pitts et al., 1988, list the input data for the various atmospheric models. For each model, a table lists the temperature and molecular weight distribution as a function of height. Each table also gives the following calculated quantities (as a function of height): pressure, density, speed of sound, density scale height, number density, mean free path, viscosity, pressure scale height, mean particle velocity, collision frequency, and columnar mass. (Appendix A of Pitts et al., 1988, provides a FORTRAN-callable routine which generates these calculated quantities from the input data.)

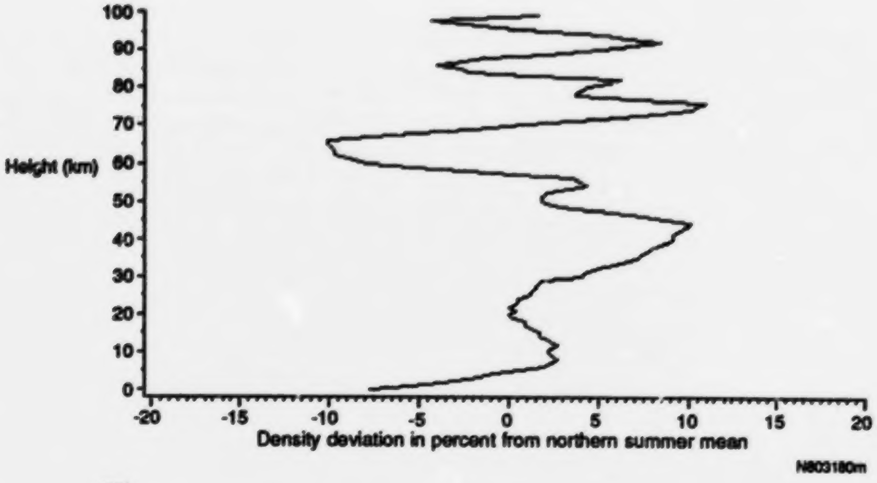

Figure 2-6.- Percent atmospheric density deviations of the Viking 1 entry conditions as compared with the revised COSPAR Northern Hemisphere mean model.

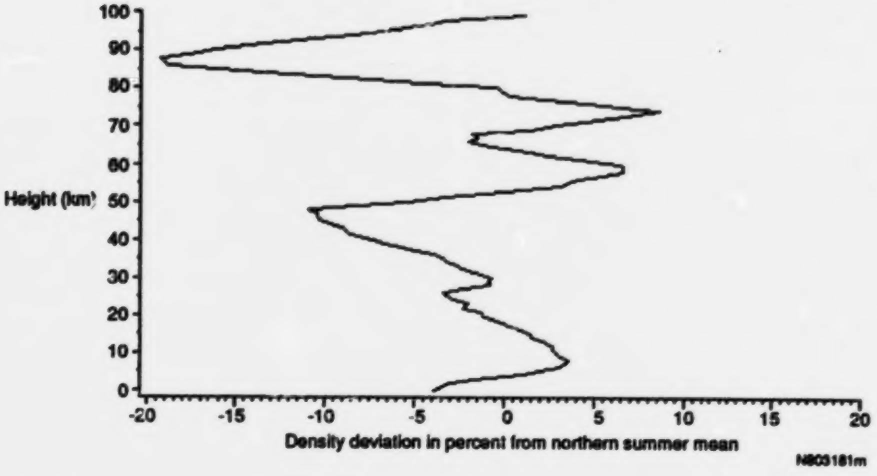

Figure 2-7.- Percent atmospheric density deviations of the Viking 2 entry conditions as compared with the revised COSPAR Northern Hemisphere mean model.

2.5.1 Viking Lander 1, Summer, Low-Dust Models

The surface pressure of 7.794 ± 0.1013 mbar which was calculated for $83.08° < L_s < 96.69°$ is used for both morning and afternoon models, (Johnson and Tillman, 1988). Stewart's model was run using $L_s = 90°$. Table C-VIII of Pitts et al., 1988, gives information for the morning VL-1, summer, low-dust model; table C-IX provides data for the afternoon VL-1, summer, low-dust model.

For these models, figure 2-8 shows little diurnal density difference near the surface, increasing to about 80 percent near 100 km.

2.5.2 Viking Lander 2, Winter, Medium-Dust Models

The surface pressure of 9.886 ± 0.0907 mbar which was calculated for $252.87° < L_s < 272.35°$ is used for both morning and afternoon models, (Johnson and Tillman, 1988). Stewart's model was run using $L_s = 270°$. Table C-X of Pitts et al., 1988, gives information for the morning VL-2, winter, medium-dust model; table C-XI provides data for the afternoon VL-2, winter, medium-dust model.

For these models, figure 2-9 shows very high densities near the surface (+120 percent of the COSPAR Northern Hemisphere mean density) falling off to less than -70 percent of the COSPAR Northern Hemisphere mean density above 70 km altitude. These atmospheres would provide considerably different entry conditions than those experienced in the northern summer entries of Viking 1 and 2.

2.5.3 Viking Lander 1, Winter, Medium-Dust Models

The surface pressure of 8.884 ± 0.0751 mbar which was calculated for $253.85° < L_s < 273.32°$ is used for both morning and afternoon models (Johnson and Tillman, 1988). Stewart's model was run using $L_s = 270°$. Table C-XII of Pitts et al., 1988, gives information for the morning VL-1, winter, medium-dust model; table C-XIII provides data for the afternoon VL-1, winter, medium-dust model.

For these models, figure 2-10 shows greater density at the surface during the morning and evening than the summer models. Conditions during the morning for regions high in the atmosphere are similar to the mean model, while afternoon conditions are greatly increased. Latitudinal density

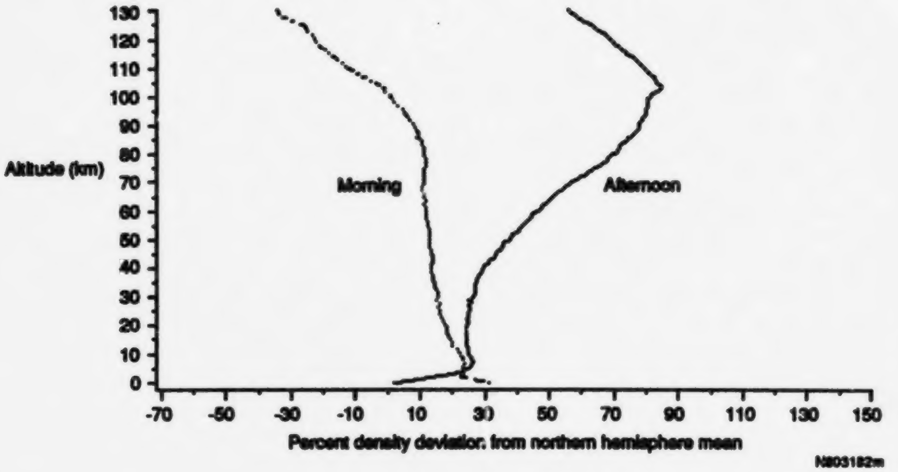

Figure 2-8.- Morning and afternoon density profiles calculated by Pollack for VL-1 location during the summer for optical depth = 0.25.

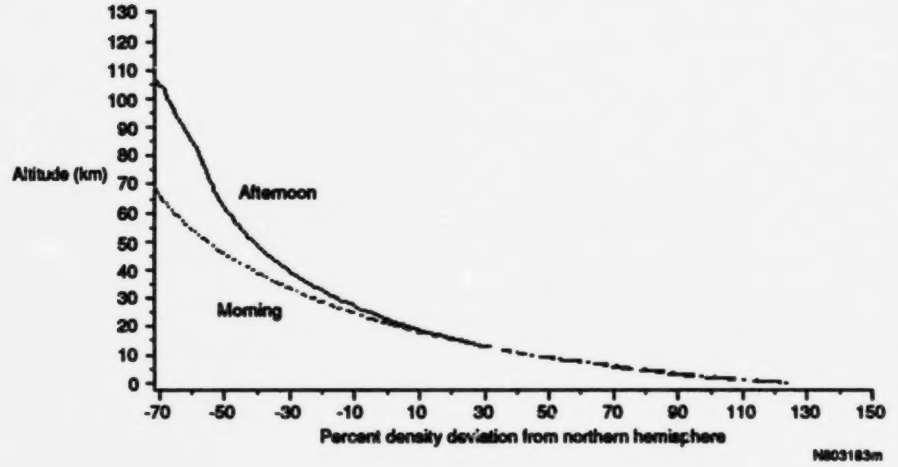

Figure 2-9.- Morning and afternoon density profiles calculated by Pollack for VL-2 location during the winter for optical depth = 0.5.

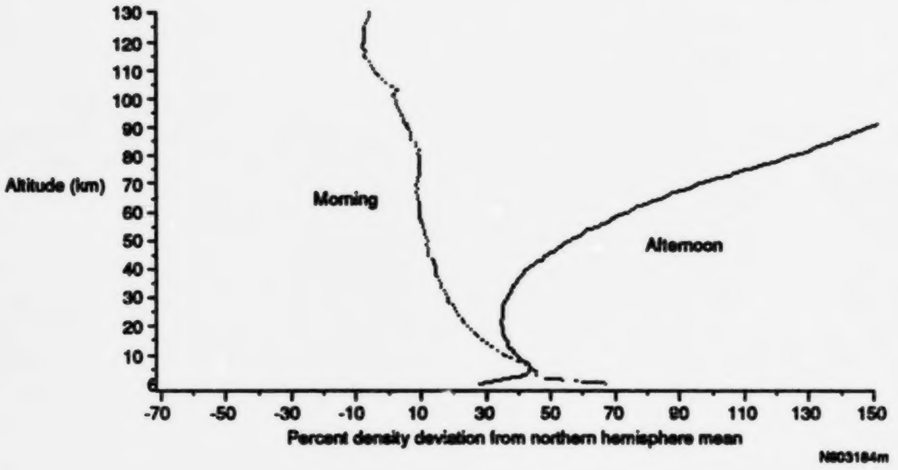

Figure 2-10.- Morning and afternoon density profiles calculated by Pollack for VL-1 location during the winter for optical depth = 0.5.

gradients during the winter months may be appreciated by comparing figures 2-9 and 2-10. In the 26 deg of latitude between the Viking 2 and Viking 1, the density at 50 km has changed by 50 percent in the morning and 80 percent in the afternoon.

2.5.4 Viking Lander 1, Winter, Dust Storm Models

The surface pressure of 8.716 ± 0.07 mbar which was calculated for $287.34° < L_s < 306.9°$ is used for both morning and afternoon models (Johnson and Tillman, 1988). Stewart's

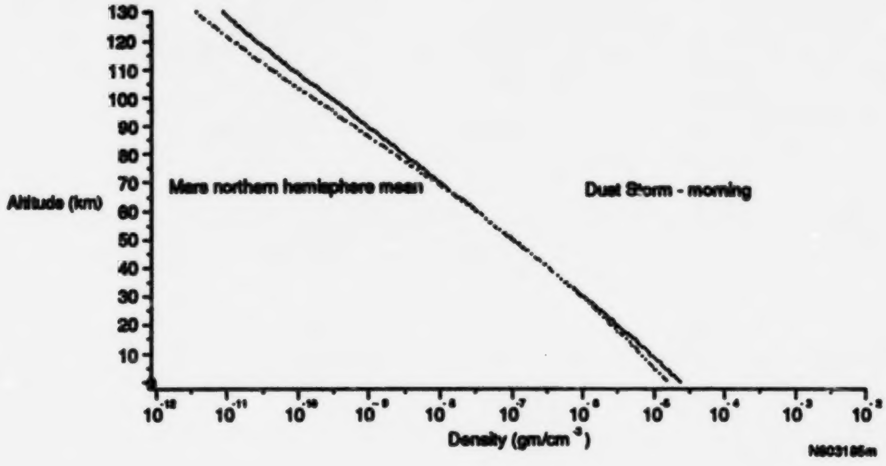

Figure 2-11.- Morning density profile calculated by Pollack for VL-1 location during winter for optical depth = 5.0.

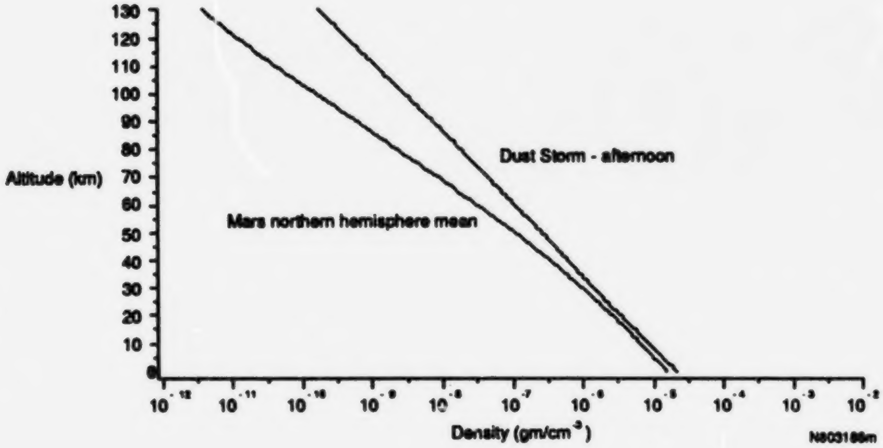

Figure 2-12.- Afternoon density profile calculated by Pollack for VL-1 location during the winter for optical depth = 5.0.

model was run using L_s = 297°. This is coupled with +1s (standard deviation) conditions for both long and short-term effects for: the exospheric temperature, the overall oxygen concentration, the diurnal oxygen concentration, the altitude of the base of the thermosphere, and the effect of dust in the stratosphere.

Table C-VI of Pitts et al., 1988, gives information for the morning VL-1, winter, dust storm model; table C-VII provides data for the afternoon VL-1, winter, dust storm model.

Because of the large differences in density from the mean model, the plots for these models (figs. 2-11 and 2-12) are drawn in log space. The morning conditions shown in figure 2-11 are greater than the mean near the surface and above 50 km. The dust storm afternoon conditions increase by an order-of-magnitude or more in the upper atmosphere due to efficient absorption of solar radiation by the airborne dust particles. Comparing figure 2-9 to 2-12 shows that extremely large horizontal density gradients would be encountered in a Northern Hemisphere entry with high inclination when a global dust storm was in the rapid growth stage in the equatorial to northern midlatitude regions.

2.6 ATMOSPHERIC WAVE MODEL

Waves in atmospheric density were measured during both Viking 1 and Viking 2 entries between 40 and 100 km altitude (Seiff and Kirk, 1977). Atmospheric temperature derived from the density profile also displays an oscillatory nature which appears to be a complex superposition of wavelengths of varying phases. Zurek, 1988, has provided a model which will allow this wave structure to be superimposed upon any of the atmospheres presented here. In that model, an amplitude and phase for both a diurnal and a semidiurnal component are provided for dusty atmospheres, and a diurnal component alone is given for "clear" atmospheres. The model provides temperatures as a function of altitude, latitude, and local time; see Pitts et al., 1988.

L_s (deg)	0.1%	1.%	10.%	50.%	90.%	99.%	99.9%	# Obs.
270-299	-13.3	-9.7	-4.5	0.7	7.4	13.3	15.6	2217
299-329	-12.0	-8.7	-4.0	0.8	9.3	16.3	19.5	2400
329-360	-17.4	-10.7	-6.2	-0.3	10.0	16.9	20.0	1892
0-29	-15.4	-8.5	-4.8	-1.1	3.7	10.0	14.8	1461
29-59	-6.7	-5.0	-2.6	-0.7	2.0	4.0	4.9	1615
59-89	-6.1	-4.9	-2.4	-0.7	1.5	2.5	3.1	289
89-119	-6.2	-4.9	-3.0	-1.0	1.0	2.5	3.3	1240
119-149	-6.3	-5.2	-3.1	-0.9	2.1	4.1	5.1	2843
149-179	-7.2	-5.6	-3.0	-1.0	3.0	5.2	6.7	2484
179-209	-13.9	-9.7	-5.5	-1.2	3.5	8.4	11.0	2187
209-239	-12.7	-9.0	-4.8	-0.1	7.7	14.6	18.4	2161
239-270	-10.6	-6.0	-1.8	1.6	7.8	14.7	16.5	2360

TABLE 2-3. - Zonal wind cumulative probabilities versus season (m/sec, + from west)

L_s (deg)	0.1%	1.%	10.%	50.%	90.%	99.%	99.9%	# Obs.
270-299	-15.1	-13.6	-7.7	-0.9	4.0	9.8	11.7	2217
299-329	-13.9	-11.9	-6.7	-0.9	5.0	10.4	13.7	2400
329-360	-17.6	-14.7	-9.9	-1.4	6.6	12.0	15.0	1892
0-29	-12.7	-11.2	-5.9	-0.3	3.3	6.9	9.0	1461
29-59	-4.6	-3.4	-1.9	-0.3	3.1	5.0	5.9	1615
59-89	-2.7	-2.5	-1.6	-0.3	2.9	4.0	4.6	289
89-119	-3.6	-3.0	-2.0	-0.4	3.1	4.5	5.0	1240
119-149	-5.8	-4.2	-2.4	-0.7	2.9	5.1	6.3	2843
149-179	-7.9	-5.5	-3.0	-0.5	2.3	5.4	6.7	2484
179-209	-16.2	-12.2	-7.6	-0.9	3.5	7.3	9.4	2187
209-239	-16.2	-12.5	-7.5	-0.5	5.5	9.7	11.7	2161
239-270	-10.8	-7.9	-4.2	0.5	5.1	9.8	14.1	2360

TABLE 2-4.- Meridional wind cumulative probabilities versus season (m/sec, + from South)

2.7 WINDS

2.7.1 Surface Winds

Winds measured by the VL-2 for approximately 1000 sols were analyzed by Tillman, 1988b. Tables 2-3 and 2-4 present information on zonal (east-west) and meridional (north-south) wind cumulative probabilities, respectively. The time periods were arbitrarily divided into 30 deg increments in L_s where $299° > L_s > 270°$ is the period following the Northern Hemisphere winter solstice (i.e., analogous to January on the Earth); L_s=0 is the vernal equinox on Mars. (For example, as shown from the first row of table 2-3, during the time period when $270° < L_s < 299°$, 2217 observations were made, 99.9 percent of the time, the winds were from the west at a velocity of less than 15.6 m/sec; 50 percent of the time, mean winds were from the west at a velocity less than 0.7 m/sec; and only 0.1 percent of the time were the winds from the east at a velocity greater than 13.3 m/sec.)

2.7.2 Wind Velocity Variation With Altitude

Hanel et al., 1972, used the Italian Research Interim Stage (IRIS) instrument on Mariner 9 to make measurements of the atmospheric thermal emission spectra (5 to 50 mm) in order to derive vertical temperature profiles in the Mars atmosphere. Since the horizontal gradient of temperature provides an estimate of the vertical wind shear (in an atmosphere obeying hydrostatic and geostrophic equilibrium), collections of vertical temperature profiles along a north-south line provide an estimate of wind structure in a meridional plane, see figure 2-13 (Hanel, 1972). Two jet axes are evident in this figure: one at 45° north with peak winds at 25 km (120 m/sec from the west) and another jet appears above 30 km at about 60° north (140 m/sec from the west). The vertical wind shear is directly proportional to the acceleration due to gravity and horizontal temperature gradient and inversely proportional to the coriolis parameter. Since the mean solar day of Mars is nearly the same as Earth (one sol = 24 hours 39.35 min), the coriolis

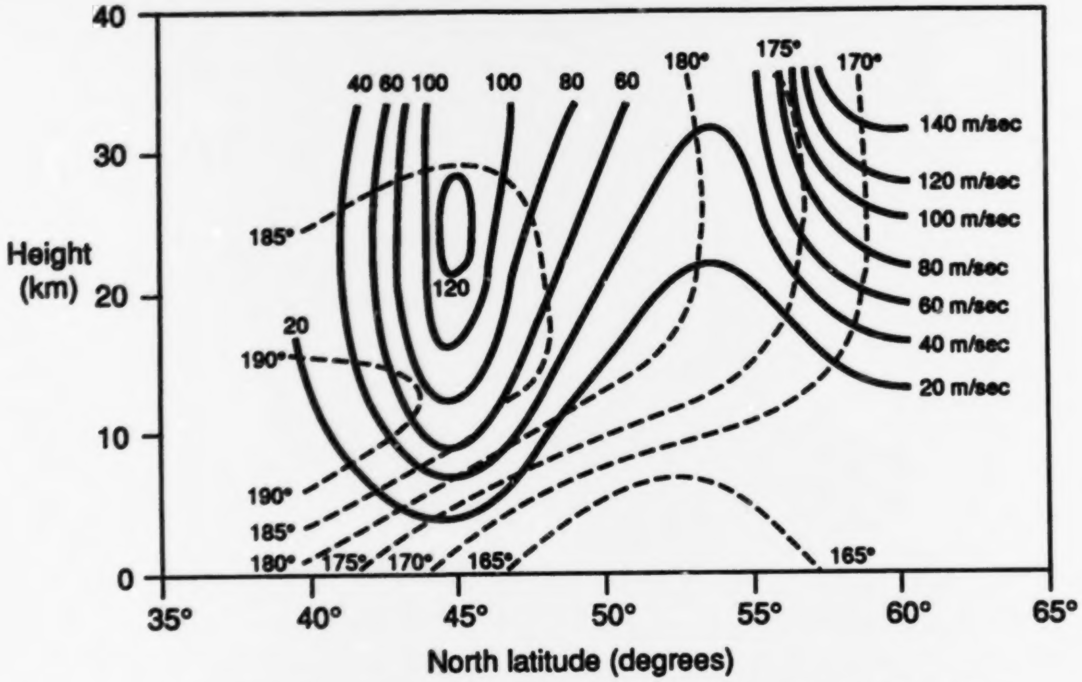

Figure 2-13.- Temperature and wind structure of the wintertime Northern Hemisphere (Hanel et al., 1972).

Temperature of wintertime martian atmosphere, plotted in a meridional plane, has been derived from infrared measurements made by Mariner 9. The temperatures, given in degrees kelvin, can be used to infer the distribution of the east-to-west component of the winds, given in meters per second. (Note that 100 m/s equals 224 mph.)

force is about the same. The acceleration due to gravity is about 1/3 of that on Earth, thereby indicating that the higher wind speeds on Mars are probably due to larger north-south temperature gradients. The data collected from Mariner 9 are such that soundings are not routinely available along a meridian at the same time of day. Consequently, figure 2-13 is the only information on vertical wind structure available. For the purpose of engineering design, the meridional winds (north-south) should probably be assumed to be a few meters per second or less, although significant advection of water vapor is known to occur in the north-south direction. These meridional wind velocities are probably much less than the velocities estimated in the east-west direction in Hanel's analysis.

Pollack et al., 1979, note that meridional movement of the edge of the global dust cloud during rapid growth phase can be tracked at 10 m/sec, but that dust-free meridional winds should be about 1 m/sec. Strong atmospheric thermal gradients around the periphery of the polar caps and the sublimation of carbon dioxide are thought to cause strong winds (Leovy, 1973) which may be the cause of local dust storms in the Southern Hemisphere, (Peterfreund and Keiffe, 1979). Topographic winds (upslope during the day, downslope during night) were measured with the Viking Lander, (Hess et al., 1977). Increasing optical depth due to dust causes greater atmospheric stability which causes winds driven by topographic heating and cooling to diminish (Pollack, 1979).

2.7.3 Dust Devils

Ninety-seven dust devils were detected on high resolution stereo images made from the Viking orbiters (Thomas and Gierasch, 1985). The size and shape of the shadow were used to infer the altitude (< 7 km, mode = 2 km) and width (<250 m). These were observed to occur within 20° latitude of the subsolar point in the afternoon during summer. Wind speed in these dust devils was not estimated.

2.8 CLOUDS

2.8.1 Composition and Properties

Due to the low pressure in the Mars atmosphere, water clouds will occur as ice crystals, which will form as hexagons. The size distribution of these Mars atmospheric ice crystal clouds isn't known because proper wavelength and scattering angle data were not acquired from the Viking landers or orbiters. However, the low atmospheric density probably allows the larger particles to rapidly settle out of the atmosphere. Because of this, crude estimates of the upper limit for ice crystal sizes are 10 mm, with a "best guess" of about 1 mm (Pitts et al., 1988).

In the Earth's atmosphere, cirrus clouds often are composed of either long hexagonal needles, hundreds of micrometers in length, and tens of micrometers in diameter, or plates hundreds of micrometers wide, and tens of micrometers thick, depending upon the temperature of formation (Ono, 1969, 1970). Riming or dendritic buildup often causes unusual additions to the crystals as they fall through the atmosphere while maintaining an orientation that maximizes their falling resistence. Large vertical velocities around terrestrial thunderstorms increase the time these hexagons can remain in the upper atmosphere.

In the absence of additional information, it may be assumed that ice crystals of 1 µm can form in the Mars atmosphere. In order for these clouds to be seen, optical depths of about 0.5 are required, thereby giving about 10^{-8} g/cm³. Shadows of these cirrus clouds seen south of Valles Marineris indicate altitudes up to 50 km with sizes of 50 to 100 km (Spitzer ,1980). It is possible that such high altitude clouds are carbon dioxide, not water ice.

The mountains Olympus Mons and Arsia Mons extend some 27 km above the mean aeroid (Fjeldb et al., 1977), and are often seen in the Viking Orbiter photographs protruding thru extensive 19 km altitude cloud layers of water ice crystals. Wave clouds (both bow-type and shock) have been observed near mountains and craters on Mars (Briggs and Leovy, 1974). These waves occur near the top of temperature inversions because of a perturbation by a mountain or crater. High altitude cloud layers of condensates and/or dust are observed in the 25 to 40 km altitude range in images of the Mars limb. Cirrocumulus and stratocumulus clouds are quite common in the north polar hood region. Early morning water ice fogs occur probably due to nighttime radiational cooling.

2.8.2 Frequency of Occurrence

Analysis of Viking lander wind data and Viking orbiter imagery of afternoon convective clouds indicate convective boundary layer which is several kilometers deep during the late afternoon in the summers (Tillman, 1977).

Mariner 9 cloud photos showed evidence of synoptic patterns similar to terrestrial frontal systems (Leovy et al., 1972). Tillman et al., 1972, analyzed one such disturbance in detail and found that it had the characteristics of a barolinic instability (frontal system), and that spectral analysis of daily average pressure indicated that similar systems appeared to pass over the lander each 3.3 sols. Ryan et al., 1978, found that the winds and pressure changes were consistent with eastward moving systems, similar to those found on Earth.

2.8.3 Dust in the Atmosphere

Sun diode data from each lander (Tillman et al., 1979; Zurek, 1982) provide an estimate of atmospheric optical depth (τ_λ) for each wavelength (λ) that is sensed. Figure 2-14 shows the optical depth data for the visible spectrum for both Viking landers for 2 Mars years.

Optical depth allows the attenuation of a signal I_o to be calculated as it traverses a plane parallel atmosphere at a zenith angle θ

$$I = I_o \exp(-\tau_\lambda/\cos\theta)$$

Studies of the optical depth versus wavelength, and the appearance of the global dust storm scattering as it appears when imaged from the Viking orbiters at various phase angles, allow estimates of the dust particle size and the vertical distribution to be made. The following information is provided by Zurek, 1988. Assuming a peak dust storm optical depth of 4, a scale height of 10 km, and a uniform mass mixing ratio up to 40 km gives a mass density (m_o, i.e., columnar mass above 1 cm²) of about 2×10^{-3} g/cm² at the surface. The mass density (m) above an altitude (Z) can then be described as:

$$m = m_o \exp(-Z/H)$$

where Z is altitude (km) and H is the scale height (km).

The following formula is used to calculate the mass volume density (M) in g/cm³

$$M = 10^{-5}\, m_o \exp(-Z/H)/H$$

When dust storms are not present, optical depths in the visible are typically about 0.5 (fig. 2-14) , thus decreasing m_o by a factor of 8.

Local dust storms are expected to be lower in height (15-20 km), but more dense by a factor of 2 (i.e., $m_o = 4 \times 10^{-3}$ g/cm²) than the value which is appropriate for global dust storms.

Thomas and Gierasch, 1985, estimated the dust loading in dust devils to be 3×10^{-8} g/cm³ (optical depth of .3 to .5), or about 10^{-3} g/cm².

The airborne particles in the Mars atmosphere are probably clay silicates, and would probably be very similar to the soil-derived aerosols (Kaolinite, Illite, and Montmorillonite) measured in the Earth's atmosphere, (Patterson and Gillette, 1977a). Patterson and Gillette found that these aerosols fit a log normal distribution (see below) with a surface mean radius (r_n) of 1.5 mm and a geometric standard deviation (s) of 2.2.

$$dN/d(\log r) = 0.424 * N_o * \exp\left[-(\log r - \log r_n)^2 / 2 * \log^2\sigma\right] / \left[(2\pi)^{1/2}\log\sigma\right]$$

where N_o is the number of particles per unit volume and r is the radius of the particles. The distributions for heavy

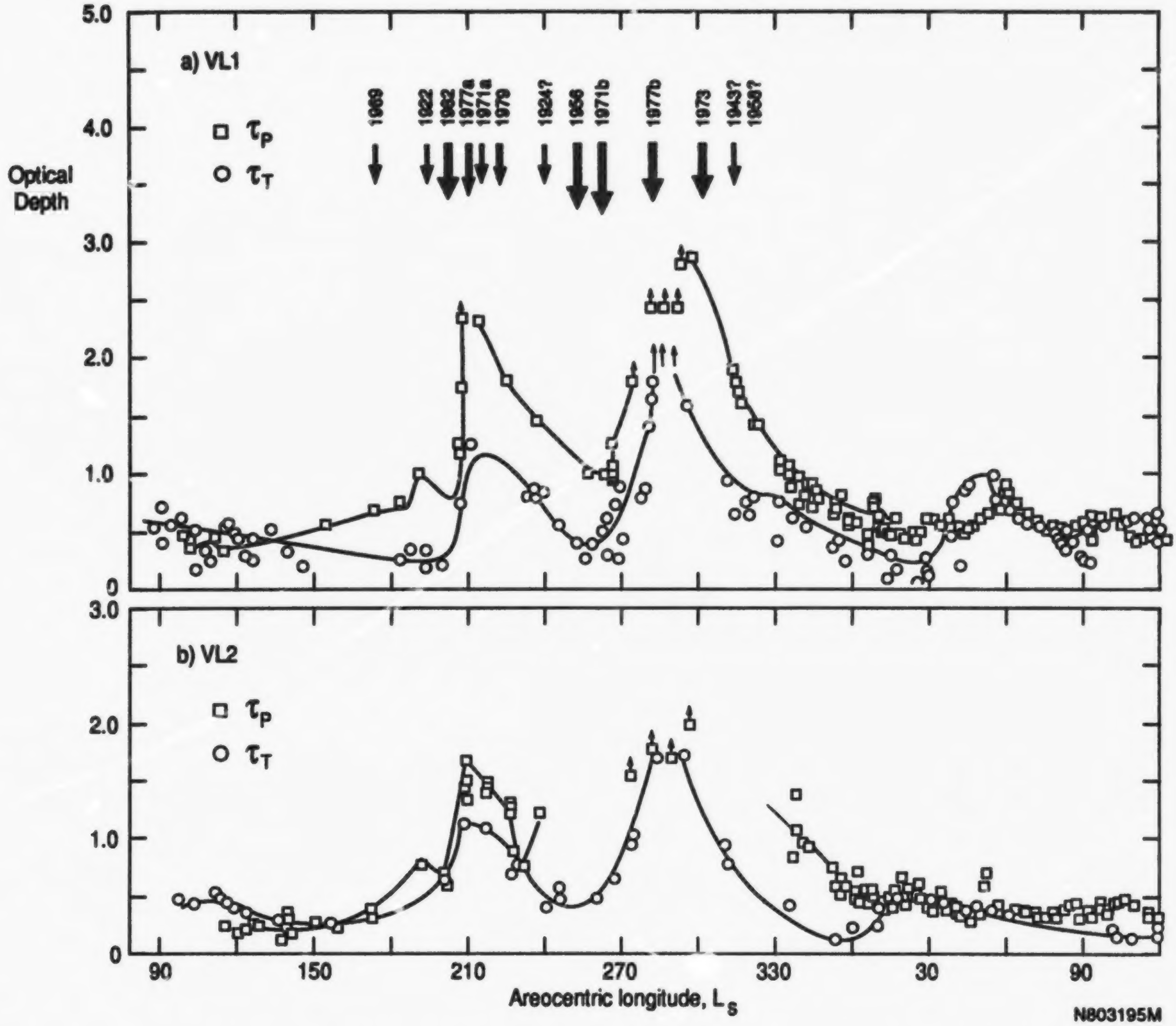

Figure 2-14.- Optical depth as measured for Viking landers 1 and 2 as a function of areocentric longitude (L_s); Zurek (1982).

Normal-incidence optical depth τ of the dust haze above VL-1 (top) and VL-2 (bottom) as a function of areocentric longitude L_s (L_s = 90° and 270° corresponding to northern and southern summer solstices, respectively) for the first Mars year of Viking observations. The τ_p values are the afternoon values determined by Pollack et al., 1979, from imaging the Sun's disk with the Viking lander imaging systems. The τ_T values are computed by Thorpe, 1981, from modeling the scene reflectance and contrast modulation observed with the Viking Orbiter cameras using red and clear filters. Small arrows mark periods when only lower bounds to the τ_p, τ_T values were estimated. The L_s values for the observed onsets of great dust storms on Mars (identified by the year in which they occurred) are also marked.

aerosol loading were found to be the sum of two distributions — a background of small size aerosols and another group of larger particles representing the newly injected particles. Measurements carried out in the high plains of West Texas by Gillette and Walker, 1977, have particles at 1.5 m elevation ranging from .5 to 100 mm, with densities as high as 2.5×10^{-7} g/cm^3.

Pollack et al., 1979, modeled the Mars dust size distribution with a modified Gamma function where r_m is the modal particle radius:

$$n(r) = C\, r^{\alpha} \exp\left[- (\alpha/\gamma)\, (r/r_m)\gamma \right]$$

$$\text{and } \alpha = 2, \gamma = 1/2, r_m = 0.4\ \mu\text{m},$$

$$C = \text{constant of proportionality.}$$

The above distribution gives a mean radius of 2.5 µm. Analysis by Pollack et al. of optical depth data from the Viking landers and high resolution spectra from the IRIS experiment from Mariner 9 imply plate-like clay particles such as Montmorillonite.

Conrath, 1975, and Toon et al., 1977, both indicate that considerable vertical mixing (eddy diffusion coefficient $\approx 10^7$ cm^2/sec) is required to maintain dust in the Mars atmosphere as observed in the Mariner 9 data. Various estimates of particles in the atmosphere range from 2 to 10 µm (Toon et al., 1977). Analysis by Toon et al., 1977, of IRIS high resolution spectra suggested that the dust is a mixture of materials, igenous silicates with greater than 60 percent SiO_2 or clay minerals. The size distribution of dust between 1 and 10 mm was similar to terrestrial airborne dust removed from the parent location by considerable distance (Toon et al., 1977).

2.9 GREAT DUST STORMS [4]

A "great" dust storm is one that will span most of one or both hemispheres of Mars. Table 2-5 provides a listing of great dust storms which have been observed. This observational record shows that one, or occasionally two dust storms of planetary scale may occur each martian year. The duration and extent of these storms vary greatly. Also, the table shows that there have been many years in which no great dust storms have been detected. Unfortunately, neither Earth-based nor spacecraft observations have been systematic enough to quantify the frequency of dust storm occurrence or even the true extent of many individual storms.

There is no reliable method for prediction of when a great dust storm will occur. However, when they do arise, the great dust storms occur during southern spring and summer. This seasonal timing appears to be related to the fact that perihelion ($L_s = 253°$) occurs just prior to the southern summer solstice ($L_s = 270°$). (Figure 2-14 gives the L_s values for the observed onset of great dust storms and also identifies the year in which each storm occurred.) Due to the eccentricity of the martian orbit, the incident solar radiation at perihelion is fully 45 percent stronger than at aphelion. Since the martian atmosphere tends to be in radiative equilibrium, this intense period of summertime radiation — along with features of variation in Mars surface topography — apparently triggers the global dust storms.

The opacity of the dust cloud in the visible wavelengths may be quite high, reaching an optical depth (τ_l) of 5 (Hunt, 1979).

The great dust storms are long-lived. Optical depths (τ_λ) for the 1971b and 1977a,b great dust storms were larger than 1 (at the visible wavelengths) for more than 100 sols for each storm.

2.9.1 Dust Storm Evolution

The maximum solar insolation for Mars occurs at the time of the southern summer solstice. Around that time, the subsolar point is between 8° and 25° south of the equator. During relatively clear periods, the increased surface heating within this latitudinal zone will enhance atmospheric convection during the day and will strengthen winds induced by the thermal effects of topography.

The "classical" view for the evolution of great dust storms (summarized by Gierasch, 1974) is initiated with one or more regional dust storms developing during southern spring or summer. Three preferential locations for these regional dust storms are: (1) the sloping plains between the northwest rim of Hellas and the Noachis uplands, where both the 1956 and 1971 great dust storms originated; (2) the sloping plains to the west, south, and southeast of Claritas Fossae, where the main centers of the 1973 and 1977a storms developed; and (3) the low-lying Isidis Planitia to the east of Syrtis Major; see table 2-5. These regions are characterized by their location in low and subtropical latitudes, by the presence of large east-facing slopes, by strong gradients in surface albedo or thermal inertia, and perhaps by regional sources of the most easily moved surface materials.

These local dust clouds expand slowly during an initial phase lasting, typically, 4 days. Expansion becomes more rapid during the next 4 days as new centers of activity develop and old ones coalesce. At first, expansion occurs largely in an east-west direction; after an additional 5 to 10 days, the dust haze has encircled the planet. Many of the core regions established during the early phases

---

[4] The materials of section 2.9 are excerpted from "Martian Great Dust Storms: An Update," by Richard W. Zurek. Icarus, vol. 50, pp. 288-310, and personal communications with Dr. Zurek.

ORIGINAL PAGE IS
OF POOR QUALITY

Year		Citation	L_s[4]	Initial location
1909	(Aug)	2,3	—	—
1911	(Nov)	2,3	—	—
1922		1,2	192	—
1924a	(Oct)	3	—	—
1924b	(Dec)	1,2,3	237	Isidis Plannitia
1939[5]		2,3	—	Utopia?
1941[5]	(Nov)	3	—	South of Isidis
1943		1	310	Isidis
1956		1,2,3	250	Hellespontus
1958		1,3	310	Isidis
1971a	(July)	1	213	Hellespontus
1971b	(Sep)	1,3, Mariner 9	260	Hellespontus
1973		1	300	Solis Planum, Hellespontus
1977a	(Feb)	Viking	205	Thaumasia Fossae
1977b	(June)	Viking	275	—
1979		Viking	225?	—
1982		Viking	—	—

1 Briggs et al., 1979.

2 Capen, 1971.

3 Michaux and Newburn, 1972. This reference also cites several "major" dust storms identified only on Lowell Observatory photographic plates and not referenced elsewhere. These events (October, 1909; September, 1911; 1926; August, 1941) are not listed above.

4 Longitude of the Sun in Mars-centered (areocentric) coordinates; seasonal date of the regional onset of the great dust storms.

5 These clouds may have remained localized phenomena.

TABLE 2-5.- Martian great dust storms
(from Zurek (1982)).

remain active and distinguishable during the later stages of the great storm.

Using a zonally symmetric circulation model, Haberle et al., 1982, found that dust is raised up to 20 km or more before significant northward transport occurs. During the truly global 1971b storm, Mariner 9 television images of the limb of Mars indicated that dust was mixed at up to 40-60 km of altitude (Leovy et al., 1972).

Once the dust storm has obscured most of one hemisphere and perhaps much of the other, the atmosphere begins to clear. This decay process is generally attributed to the increasing static stability above the regions where dust is raised (Pollack et al., 1979; Leovy and Zurek, 1979). This increased static stability should effectively suppress boundary layer turbulence and/or decouple near-surface winds from those aloft. Observations (Conrath et al., 1973; Lindal et al., 1979; Martin and Kieffer, 1979) clearly show that the martian atmosphere is certainly more isothermal and thus stable during the decay phase. Even if local storms were still active, the greatly enhanced stability would limit the ability of such storms to convectively raise dust high into the atmosphere where it could most easily spread. Opacities greater than one ($\tau_\lambda > 1$) will also suppress surface heating (Pollack et al., 1979) and its associated diurnal temperature variation and convection.
The time estimated for the decay phase of the 1971b storm was 60 sols (Conrath, 1975); for the 1977a storm, the decay phase was 75 sols, and for the 1977b storm it was 51 sols (Pollack et al., 1979).

2.9.2 Local Dust Storms

Local dust storms, which may affect regions encompassing up to 10^6 km^2, have been observed on Mars during all seasons (Gifford, 1964; Capen, 1974; Briggs and Leovy, 1974; Peterfreund and Kieffer, 1979). However, they have been observed to occur most frequently in the approximate latitude belts 10° to 20° N and 20° to 40° S, with more clouds seen in the south than in the north and with more frequent sightings during southern spring and summer (Michaux and Newburn, 1972). Thus, local storms are apparently most likely to occur during the same periods as the great dust storms.

Winds exceeding 25 m/sec were observed (Ryan et al., 1981) by the VL-1 meteorological instruments 1.6 m above the surface during the only local dust storm observed at the lander sites (James and Evans, 1981). (Winds exceeding 25 m/sec were otherwise rarely seen at the lander sites.)

2.10 SOLAR IRRADIANCE AT THE MARS SURFACE

The solar irradiance incident on the surface of Mars is composed of two components: the direct beam, and diffuse component. The direct beam irradiance is affected by scattering and absorption along the path. Measurement of the optical depth of the atmosphere (Zurek, 1982) allows an estimate of the absorption and scattering out of the beam. The following equations will permit estimates of the irradiance as a function of season, latitude, time of day, and optical depth of the atmosphere.

The mean solar radiation at Mars (σ) is 590 W/m^2; at perihelion (L_s = 249°) the value is 718 W/m^2, and at aphelion (L_s = 69°) the value is 493 W/m^2.

Direct solar radiation, S, on the surface as affected by simple single scattering of the atmosphere is:

$$S = \sigma \cos(\theta) \exp(-\tau_\lambda / \cos\theta)$$

where:

$$\cos(\theta) = \sin(\varnothing)\sin(\delta) + \cos(\varnothing)\cos(\delta)\cos(h)$$

θ = latitude,

δ (solar declination) = -24.8° at L_s = 270° (Northern Hemisphere winter),

δ (solar declination) = +24.8° at L_s = 90° (Northern Hemisphere summer)

h = hour angle (0 at Zenith, + to west, range 0 - 2π
[day = 24 hr, 39 min]

$$\sigma\,(\text{watts/m}^2) = 590\,(1 + \text{ecc}.\,(\cos(L_s - 245°))^2/(1 - \text{ecc}^2)^2$$

$$\text{ecc} = 0.093377$$

Because of the tendency for considerable forward scattering by small particles in the Mars atmosphere, and because of the diffuse skylight, the estimate for total solar irradiance at the surface will probably be larger than the value for direct solar radiance, S, by 10 percent or more.

2.10.1 Solar Ultraviolet Flux at the Mars Surface

The solar flux incident at the surface is a function of the wavelength in question, the distance of the planet from the Sun, and the location in latitude, longitude, and altitude. Because of the tenuous nature of the Mars atmosphere, the ultraviolet radiation which reaches the surface is much greater than on Earth. However, some absorption by the Mars atmosphere does occur. Below 2000 Å, virtually no solar radiation reaches the surface due to absorption by carbon dioxide. Minor constituents such as water vapor, molecular oxygen, and ozone also absorb ultraviolet radiation, but their contribution is small compared with carbon dioxide. Figure 2-15 shows a comparison of the radiation incident on the top of the atmosphere with that radiation calculated by Kuhn and Atreya, 1979, to be present at the martian surface (for northern spring and winter at 50° N latitude).

Latitudinal distribution of daily solar radiation calculated by Kuhn and Atreya, 1979, for three different wavelengths is shown in figure 2-16.

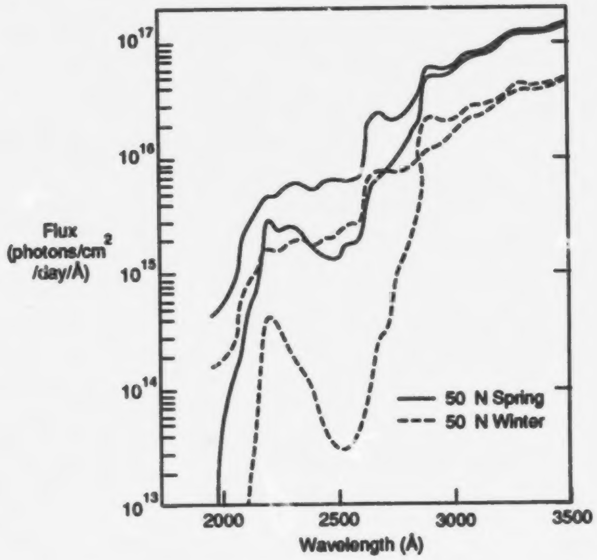

◄ Figure 2-15.- A comparison of the radiation incident on the martian atmosphere and at the surface for 50° N spring and 50° N winter. The uppermost curve for each season corresponds to the radiation incident on the atmosphere (Kuhn and Atreya, 1979).

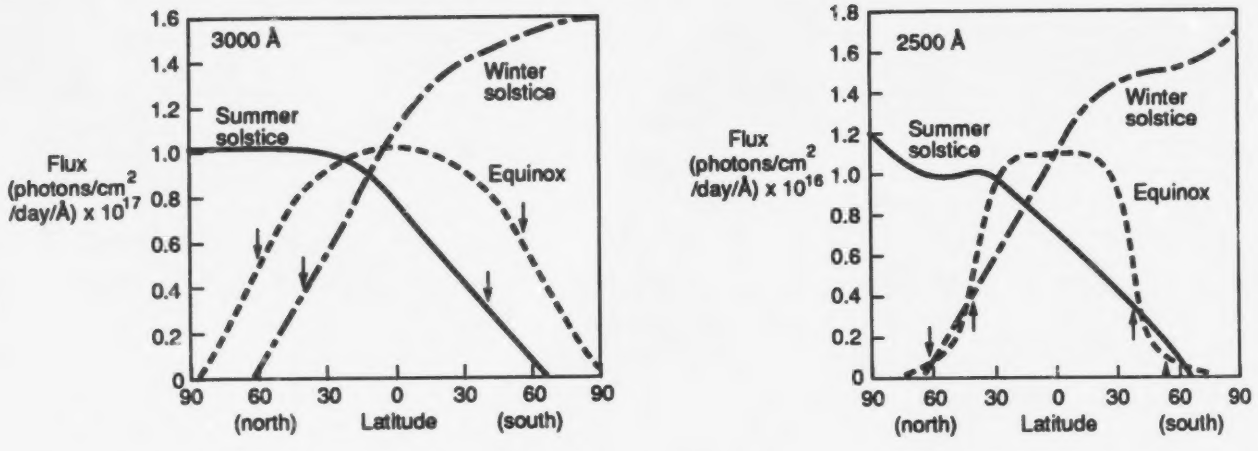

▲ Figure 2-16.- Latitudinal distribution of daily solar radiation at various wavelengths reaching the martian surface. The arrows refer to the edge of the polar hood (Kuhn and Atreya, 1979). ►

(a) 3000 Å (b) 2500 Å (c) 2000 Å

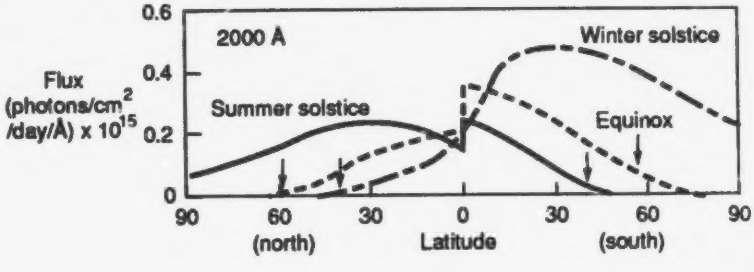

2.11 REFERENCES

Arvidson, R. E.; Guines, E. A.; Moore, H. J.; Tillman, J. E; and Wall, S. D.; 1983: Three Mars Years: Viking Lander 1 Imaging Observations. Science, vol. 222, pp. 463-468.

Barth, C. A.; 1974: The Atmosphere of Mars. Annu. Rev. Earth Planet. Sci., vol 2, p. 333.

Briggs, G. A.; and Leovy, C. B.; 1974: Mariner 9 Observations of the Mars North Polar Hood. Bull. American Meteorol. Soc., vol. 55, no. 4, Apr., pp. 278-296.

Cain, A. J.; Kliore, B. L.; Seidel, B. L.; Sykes, R. J.; and Woiceshyn., P. M.; 1973: Approximations to the Mean Surface of Mars and Mars Atmosphere Using Mariner 9 Occultations. J. Geophys. Res., vol. 78, p. 4352.

Capen, C.F.; 1974: The Martian Yellow Cloud of July 1971. Icarus, vol. 22, pp. 345-362.

Chamberlain, T. E.; Cole, H. L.; Dutton, R. G.; Greene, G. C.; and Tillman, J. E.; 1976: Atmospheric Measurements on Mars: The Viking Meteorology Experiment. Bull. Amer. Met. Soc., vol. 57, p. 1094.

COESA, U. S. Standard Atmosphere, 1962.

COESA, U. S. Standard Atmosphere Supplements, 1966.

COESA, U. S. Standard Atmosphere, 1972.

Conrath, B .J.; Curran, R.; Hanel, R.; Kunde, V.; Maguire, W.; Pearl, J.; Pirraglia, J.; Welker, J.; and Burke, T.; 1973: Atmospheric and Surface Properties of Mars Obtained by Infrared Spectroscopy on Mariner 9. J. Geophys. Res., vol. 78, pp. 4267-4278.

Conrath, B. J.; 1975: Thermal Structure of the Martian Atmosphere During the Dissipation of the Dust Storm of 1971. Icarus, vol. 24, pp. 36-46.

Davies, D. W.; 1979a: The Vertical Distribution of Mars Water Vapor. J. Geophys. Res., vol. 84, no. B6, pp. 2875.

Davies, D. W., 1979b: The Relative Humidity of Mars' Atmosphere. J. Geophys. Res. vol. 84, no B14, pp. 8335-8340.

Fjeldbo, G.; Sweetnam, D.; Brenkle, J.; Christensen, E.; Farless, D.; Mehta, J.; Seidel, B.; Michael, W.; Wallio, A.; and Grossi, M.; 1977: Viking Radio Occultation Measurements of the Martian Atmosphere and Topography: Primary Mission Coverage. J. Geophys. Res., vol. 82, no. 28, pp. 4317 - 4324.

Gierasch, P.J.; 1974: Martian Dust Storms. Rev. Geophys. Space Phys., vol. 12, pp. 730-734.

Gifford, F.A., 1964: A Study of Martian Yellow Clouds that Display Movement. Mon. Weather Rev., vol. 92, pp. 435-440.

Gillette, D. A.; and Walker, T. R.; 1977: Characteristics of Airborne Particles Produced by Wind Erosion of Sandy Soil, High Plains of West Texas. Soil Science, vol. 123, no. 2, pp. 97-110.

Haberle, R.M.; Leovy, C.B.; and Pollack, J.B.; 1982: Some Effects of Global Dust Storms on the Atmospheric Circulation on Mars. Icarus, vol. 50, pp. 322-367.

Haltiner, G. J.; 1971: Numerical Weather Prediction. John Wiley, New York, p. 159.

Hanel, R.; Conrath, B.; Hovis, W.; Kunde, V.; Lowman, P.; Maguire, W.; Pearl, J.; Pirraglia, J.; Prabhakara, C.; Schlachman, B.; Levin, G.; Stratt, P.; and Burke, T.; 1972 : Investigation of the Martian Environment by Infrared Spectroscopy on Mariner 9. Icarus, vol. 17, pp. 423-442.

Hanel, R.; Schlachman, B.; Breihan, E.; Bywaters, R.; Chapman, F.; Rhodes, M.; Rodgers, D.; and Vanous, D.; 1972: Mariner 9 Michelson Interferometer. Applied Optics, vol. 11, pp. 2625-2634.

Hunt, G.E.; 1979: Thermal Infrared Properties of the Martian Atmosphere. Predictions of the Presence of Dust and Ice Clouds from Viking IRTM Spectral Measurements. J. Geophys. Res., voi. 84, pp. 2865-2874.

Jakosky, B. M.; and Farmer, C. B.; 1982: The Seasonal and Global Behavior of Water Vapor in the Mars Atmosphere: Complete Global Results of the Viking Atmospheric Water Detector Experiment. J. Geophys. Res., vol. 87, no. B4, pp. 2999-3019.

James, P.B.; and Evans, N.; 1981: A Local Dust Storm in the Chryse Region of Mars: Viking Orbiter Observations. Geophys. Res., Lett., vol. 8, pp. 903-906.

Johnson and Tillman, 1988: Private communications.

Kuhn, W.R.; and Atreya, S.K.; 1979: Solar Radiation Incident on the Martian Surface. Journal of Molecular Evolution, vol. 14, pp. 57-64.

Leovy, C. B.; Briggs, G. A.; Young, A. T.; Smith, B. A.; Pollack, J. B.; Shipley, E. N.; and Widley, R. L.; 1972: The Martian Atmosphere: Mariner 9 Television Experiment Progress Report. Icarus, vol. 17, pp. 373-393.

ORIGINAL PAGE IS
OF POOR QUALITY

Leovy, C. B.; Tillman, J. E.; Guest, W. R.; and Barnes, J.; 1985: Interannual Variability of Martian Weather, Recent Advances in Planetary Meteorology, ed. Garry Hunts. Proceedings of Seymour Hess Memorial Symposium, IUGG Hamburg 1983. Cambridge University Press, pp. 69-84.

Leovy, C.B.; and Zurek, R.W.; 1979: Thermal Tides and Martian Dust Storms: Direct Evidence for Coupling. J. Geophys. Res., vol. 84, pp. 2956-2968.

Leovy, C. B.; 1977: The Atmosphere of Mars. Scientific American, vol. 237, July 1977, pp. 34-43.

Lindal, G. F.; Hotz, H. B.; Sweetnam, D. N.; Shippony, Z.; Brenkle, J. P.; Hartsell, G. V.; and Spear, R. T.; 1979: Viking Radio Occultation Measurements of the Atmosphere and Topography of Mars: Data Acquired During 1 Martian Year of Tracking. J. Geophys. Res., vol. 84, no. B14, pp. 8443-8456.

Martin, T.Z.; and Kieffer, H.H.; 1979: Thermal Infrared Properties of the Martian Atmosphere. The 15-mm Band Measurements. J. Geophys. Res., vol. 84, pp. 2843-2852.

Michaux, C.M.; and Newburn, Jr., R. L.; 1972: Mars Scientific Model. JPL document no. 606-1, Jet Propulsion Laboratory, Pasadena, California.

Nier, A. O.; and McElroy, M. B.; 1977: Composition and Structure of Mars' Upper Atmosphere: Results from the Neutral Mass Spectrometers on Viking 1 and 2. J. Geophys. Res., vol. 82, pp. 4341-4249.

Ono, A.; 1970: Growth Mode of Ice Crystals in Natural Clouds. Journal of the Atmospheric Sciences, vol. 27, pp. 649-658.

Ono, A.; 1969: The Shape and Riming Properties of Ice Crystals in Natural Clouds. J. of Amospheric Sciences, vol. 26, no. 1, pp. 138-147.

Owen, T. C.; Biemann, K.; Rushneck, D. R.; Biller, J. E.; Howarth, D. W.; and Lefleur, A. L.; 1977: The Composition of the Atmosphere at the Surface of Mars. J. Geophys. Res., vol. 82, pp. 4635-4639.

Patterson, E. M.; and Gillette, D. A.; 1977: Commonalities in Measured Size Distributions for Aerosols Having a Soil-Derived Component. J. Geophys. Res., vol. 82, no. 15, pp. 2074-2082.

Peterfreund, A.R.; and Kieffer, H.H.; 1979: Thermal Infrared Properties of the Martian Amosphere, 3. Local Dust Clouds. J. Geophys. Res., vol. 84, pp. 2853-2863.

Pitts, D.E., Tillman, J.E.; Pollack, J.; Zurek, R.W.; 1988: Model Profiles of the Mars Atmosphere for the Mars Rover and Sample Return Mission. PRELIMINARY DRAFT

Pitts, D. E. and Kyle, K. D.; 1969: A Model Atmosphere for Earth Resources Applications, NASA TMX-58033.

Pitts, D. E.; 1968: A Computer Program for Calculating Model Planetary Atmospheres. NASA TND-4292.

Pollack, J. B.; Colburn, D. S.; Flasar, F. M.; Kahn, R.; Carlston, C. E.; and Pidek, D.; 1979: Properties and Effects of Dust Particles Suspended in the Martian Atmosphere. J. Geophys. Res., vol. 84, no. B6, pp. 2929-2945.

Ryan, J.A.; Sharman, R.D.; and Lucich, R.D.; 1981: Local Mars Dust Storm Generation Mechanism. Geophys. Res. Lett., vol 8. pp. 899-901.

Ryan, J. A.; Hess, S. L.; Henry, R. M.; Leovy, C. B.; Tillman, J. E.; and Walcek, C.; 1978: Mars Meteorology: Three Seasons at the Surface. Geophys, Res. Lett., vol. 5, pp. 715-718 and 815.

Seiff, A.; 1982: Post Viking Models for the Summer Atmosphere of Mars. Adv. Space Res., vol. 2, pp. 3-17.

Seiff, and Kirk, D. B.; 1977: Structure of the Atmosphere of Mars in Summer at Mid-Laitudes. J. Geophys. Res., vol. 82, no. 28, pp. 4364-4377.

Spitzer, C. R., ed.; 1980: Viking Orbiter Views of Mars, NASA SP-441.

Stewart, Ian; 1987: Revised Time Dependent Model of the Martian Atmosphere for Use in Orbit Lifetime and Sustenance Studies. Laboratory for Atmospheric and Space Physics, the University of Colorado, JPL PO # NQ-802429, Final Report.

Thomas, P.; and Gierasch, P. J.; 1985: Dust Devils on Mars. Science, Oct. 11, pp. 175-177.

Tillman, J. E.; Henry, R. M.; Hess, S. L.; 1979: Frontal Systems During Passage of the Martian North Polar Hood Over the Viking 2 Site Prior to the First 1977 Dust Storm. J. Geophy. Res., vol. 84. no. B6. pp. 2947-2955.

Tillman, J. E.; 1985: Martian Meteorology and Dust Storms From Viking Observations.. Proceedings of The Case for Mars II conference, Boulder Colo., July 1984. Science and Technology series for American Astronautical Society by Univelt, Inc., San Diego, CA. Christopher P. Mckay, ed., vol. 62.

Tillman, J. E.; 1977: Dynamics of the Boundary Layer of Mars. Symposium on Planetary Atmospheres, Royal Society of Canada, Ottawa, Canada, Sept.

Tillman, J. E.; 1988: Mars Global Atmospheric Oscillations: Annually Synchronized, Transient Normal Mode Oscillations and the Triggering of Global Dust Storms. J. Geophys. Res., vol. 93, no. D8, August 20, pp. 9433-9451.

Tillman, J.E.; 1988: Personal communication.

Tillman, J. E.; Murphy, J. G.; and Johnson, N. C.; 1988: Viking Lander 1 Binned and Splined Product, version 2 for D. E. Pitts, Viking Computer Facility internal document and tape, 16 Feb.

Toon, O. B.; Pollack, J. B.; and Sagan, C.; 1977: Physical Properties of the Particles Composing the Martian Dust Storm of 1971-1972. Icarus, vol. 30, pp. 663-696.

Yen, C. L.; Blume, W. H.; 1986: Mars Observer Planetary Constants and Models. July 1, 1986, JPL D-3444.

Zurek, R.; 1988: Personal communication.

Zurek, Richard W.; 1982: Martian Great Dust Storms: An Update. Icarus, vol. 50, pp. 288-310.

ORIGINAL PAGE
COLOR PHOTOGRAPH

Viking Lander 1 photograph of Chryse Planitia.

Mars Surface Model[1]

3.1 INTRODUCTION

Important problems that confront future surface and scientific exploration of Mars are the physical and chemical properties of the surface materials, the topographic characteristics of various terrains, and the nature of the geologic processes that formed the materials and shaped the surfaces. The design of landing spacecraft and vehicles for the exploration of Mars, the selection of suitable landing sites and vehicle traverses, and the acquisition of samples of materials for scientific analyses require a resolution of these problems on a global scale and a good understanding of the surface of Mars at scale-lengths appropriate for landed spacecraft, vehicles, and sampling devices.

A description of the Viking landing sites is given below, and the chemical and mechanical properties of the surface materials at those sites are summarized. Comparisons of the relations between the physical properties of Viking landing sites' surface materials (e.g., dielectric constant and thermal inertia) with physical properties of other martian terrains (as inferred from radar observations of Mars from Earth and thermal observations of Mars from Viking Orbiters) suggests that the surface materials at the landing sites are good analogs for the materials of most places on Mars exclusive of the polar regions.

3.2 VIKING LANDING SITES

3.2.1 General Physical Description

Panoramic views of Chryse Planitia obtained by Viking Lander 1 (VL-1)[2] reveal large tracts of dune-like drifts that are superposed on a rocky substrate and blocky rims of near and distant large impact craters that rise above the surroundings (Mutch et al., 1976a, b; Morris and Jones, 1980). A number of these impact craters are so near to the landing site that debris and rock fragments ejected from them must have reached the site (Moore et al., 1987). Unlike the lunar surface, craters smaller than a few tens of meters are conspicuously absent. On closer inspection, most of the dune-like drifts have been deflated by the wind and are seen to be cross-laminated, but there are two, smooth dune forms about 15 m from the lander that are not deflated. The drifts are present as large complexes (≈10 m), individual drifts (1-3 m), isolated patches (< 1 m), and windtails on the lee sides of rocks (Binder et al., 1977). Drift material is present in the lander sample field. Rocks of a variety of sizes, shapes, and morphologies are imbedded in or resting on the substrate; large rocks locally protrude through the superposed drifts. Sizes of nearby rocks range from a centimeter or so to several meters. Surfaces of the substrate between the rocks are covered with a thin veneer of fines or littered with small mm- to cm-size objects which are chiefly clods. Rock fragments and thinly veneered, littered surfaces occur in the sample field of the lander. The material of the substrate between the rocks and beneath the veneer of fines and littering clods is called blocky material because of its behavior during sampling (Moore et al., 1977, 1979, 1982). Probable outcrops of rock are present beyond the sample field (Mutch et al., 1976a; Binder et al., 1977).

Panoramic views of Utopia Planitia obtained by Viking Lander 2 (VL-2) reveal a rock-strewn surface and a monotonous, flat horizon (Mutch et al., 1977, 1976c). Rocks near the lander are generally larger and cover more area than those at Lander 1 (Moore et al., 1979); they range in size from a few centimeters to a meter and more in diameter. The rocks, along with finer debris, may have been derived locally by the dynamic deposition of ejecta from the crater Mie 180 km to the east (Moore et al., 1987). Drifts are both scarce and small. Areas between the rocks are commonly littered with centimeter-size and smaller clods. Smooth surfaces of crusts, transected by fractures, and mud crack-like mosaics of surface-material units that have been exposed and scoured by the wind are also common. The material between the rocks is called crusty to cloddy material because of its behavior during sampling (Moore et al., 1977, 1979, 1982).

There may be local accumulations of bright red dust superposed on the surfaces at both sites. Very thin layers of cohesionless dust from local dust storms are deposited on the surfaces and then whisked away by mild winds (Arvidson et al., 1983). Local accumulations of this dust that thicken to produce unstable layers (≈1 cm thick) offer an explanation for the formation of the miniature landslides at the VL-1 site (Moore, 1986).

---

[1] Most materials of part 3 are excerpted from the document, "Viking Landing Sites, Remote Sensing Observations, and Physical Properties of Martian Surface Materials," by H.J. Moore and B.M. Jakosky. Preliminary draft, 1988. (Minor editorial changes have been made for consistency of format with other parts of the present document.)

[2] Lander 1 was renamed the Mutch Memorial Station in honor of Dr. Thomas A. Mutch. However, Lander 1 or VL-1 will be used for simplicity.

3.2.2 Chemical Properties of Surface Materials[3]

The Viking landers were not designed or instrumented to conduct a broad survey of the chemical properties of the martian surface. Nonetheless, Viking returned several very specific results that have been used to infer the nature of the martian soil and its geochemical history. The X-ray Fluorescence experiment analyzed the elemental composition of the loose material at the Viking lander sites. Unfortunately, from the exobiology perspective, the instrument could only detect elements with atomic number greater than 12 (Baird et al., 1977); thus, there was no direct measurement of the elements oxygen (O), nitrogen (N), carbon (C), or hydrogen (H).

In addition to the lander cameras (which would show the presence of any obvious macroscopic life-forms) and the gas chromatograph-mass spectrometer (GCMS) (which searched for organics in the soil), the Viking landers contained three experiments specifically designed to search for indications of life on Mars: the Gas Exchange Experiment (GEX) (Oyama and Berdahl, 1977), designed to determine if martian life could metabolize and exchange gaseous products in the presence of water vapor and in a nutrient solution; the Labeled Release Experiment (LR) (Levin and Straat, 1977), which sought to detect life by the release of radioactively labeled carbon (^{14}C) initially incorporated into organic compounds in a nutrient solution; and the Pyrolytic Release Experiment (Horowitz and Hobby, 1977), based on the assumption that martian life would have the capability to incorporate radioactively labeled carbon dioxide in the presence of sunlight (photosynthesis). The results of all three experiments showed definite signs of chemical activity, but this was probably nonbiological in origin (Horowitz, 1977; Klein, 1978, Mazur et al., 1978).

The results of the Viking biology experiments have led to the widespread belief that there are oxidants in the martian soil. The three key results upon which this hypothesis is based are:

1. The GCMS failed to detect organics in surface samples and from samples below the surface (maximum depth sampled was about 10 cm) (Biemann et al., 1977; Biemann, 1979). Since there are at least two mechanisms that could produce organics on Mars, meteoritic infall and ultraviolet irradiance, (Biemann et al., 1977), the absence of organics suggests that a mechanism for destroying them is present.
2. The soil released O_2 upon humidification in the GEX (Oyama and Berdahl, 1977, 1979) in amounts ranging from 70 to 790 nanomoles per cm^3. Heating of the sample to 145 °C for 3.5 hrs reduced the amount of O_2 released by about 50 percent. There was a slow evolution of CO_2 when nutrient was added to the soil.
3. The LR indicated the rapid release of CO_2 followed by a prolonged, slow release of CO_2 from radioactively labeled carbon in a nutrient solution. The effect was completely removed by heating the solution to 160 °C for 3 hrs, partially destroyed at 40-60 °C, and relatively stable for short periods at 18 °C but lost after long-term storage at 18 °C.

The chemical activity and lack of organics has been interpreted to be caused by one or more oxidants in the martian soil (Klein, 1978). The standard mechanism to explain the chemical reactivity of the Mars soil is the presence of oxidants, such as H_2O_2 produced by an external energy source interacting with atmospheric gases and/or the soil (Hunten, 1979). In addition to peroxide (H_2O_2), alkali and alkaline, Earth superoxides and ozonides could be produced by a variety of energetic processes. The nature of these oxidants is not known. Based upon the GEX and LR results, Klein (1978, 1979) has offered an analysis to suggest that there are three oxidants in the Mars soil:

1. GEX oxidant: The GEX oxidant is a strong oxidant that is relatively thermally stable and capable of oxidizing water.
2. LR oxidant: A second strong oxidant must exist to explain the LR results. This oxidant differs from the GEX oxidant in that it is thermally unstable.
3. Weak oxidant: A third, weak oxidant (gamma-Fe_2O_3) is required to explain the slow oxidation of the nutrient in the GEX experiment and release of CO_2.

Possible oxidants for the GEX oxidant include KO_2 and ZnO_2 (Ponnamperuma et al., 1977) and CaO_2 (Ballou et al., 1978). If each mole of oxidant released approximately one mole of O_2, and assuming a soil density of 1.5 g/cm^{-3}, then the density of oxidant would be about 2 to 25 ppm by mass corresponding to the release of 70 to 790 nanomoles of O_2.

A possible oxidant for the LR oxidant is H_2O_2 which has been catalyzed in the surface by the soil mineral. The concentration of H_2O_2 required to explain the LR results is about 5 ppm by mass.

Alternative explanations for the results of the Viking biology experiments include: (1) intrinsically reactive clays (Banin and Rishpon, 1979; Banin and Margulies, 1983), or the production of radicals such as OH - due to a chemical

---

[3] The materials of section 3.2.2 were prepared by Dr. Christopher P. McKay of the NASA Ames Reaserch Center, 1988.

ORIGINAL PAGE
COLOR PHOTOGRAPH

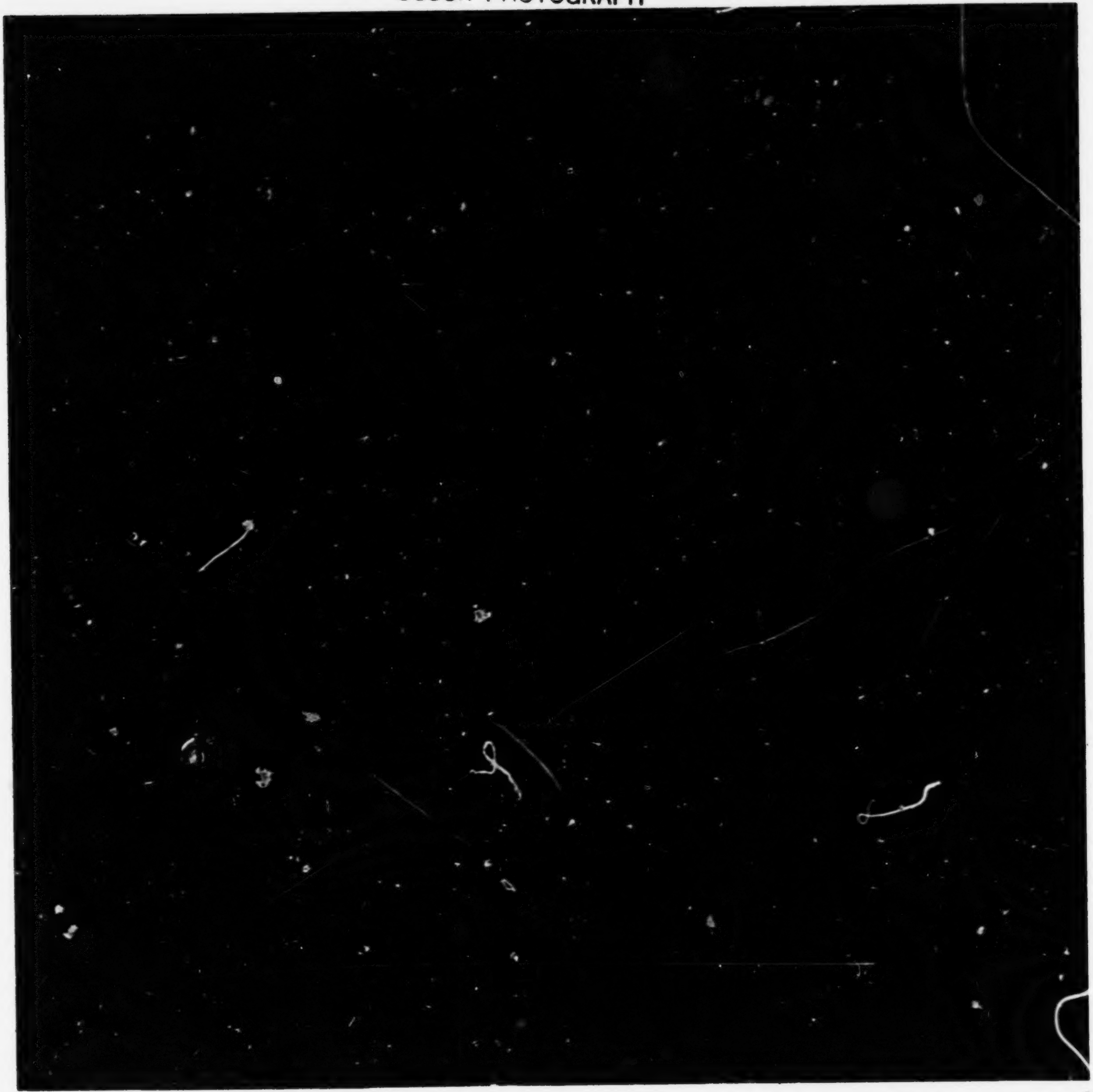

First color photograph of Utopia Planitia taken by Viking Lander 2; camera is facing northeast. (The spacecraft is tilted about 8° to the west, thereby causing the horizon to appear tilted.)

weathering process in the soil (Huguenin et al., 1979) without any ultraviolet excitation; and (2) release of physically absorbed gases in the martian soil with no chemical reactions necessary (Fanale et al., 1982). It has been suggested that the O_2 released in the GEX could be due to physically trapped O_2 within micropores (Nussinov et al., 1978).

There are also suggestions of oxides produced in the soil by the direct action of ultraviolet light (Chun et al., 1978; Oro and Holzer, 1979). Hunten, 1979, 1987, has suggested that H_2O_2 is produced in the atmosphere due to photochemical reactions at a rate of about 2 X 10^9 equivalent "O_2" molecules cm^{-2} s^{-1} and that this could be the source of the oxidants suggested by Klein, 1979. Another consideration is of the kinetics in the release and readsorbtion of the CO_2 within the LR; it has been suggested that the wetted soil would absorb the CO_2 formed unless the resulting solution was acidic (Ponnamperuma et al., 1977). Plumb et al., (work in progress) have suggested that the oxident is a peroxonitrite, which they claim can be produced by the action of ultraviolet radiation (at 253.7 n. mi.) on nitrates in the martian soil.

3.2.3 Physical Properties of Surface Materials

No Viking lander instruments were specifically designed or allotted, nor were engineering and scientific measurements specifically designed for the task of determining the physical properties of the martian surface materials (Moore et al., 1987). For this reason, information on the physical properties is gleaned from a variety of sources, such as the interaction of the landers and surface materials during landing, surface sampler activities and estimates of forces from motor-current records, and the results from other scientific investigations (Moore et al., 1987). Thus, some of the physical properties can only be crudely estimated.

There are four general classes of materials in the sample fields; in order of increasing overall strength, they are: (1) drift (VL-1), (2) crusty to cloddy (VL-2), (3) blocky (VL-1), and (4) rock (VL-1 and 2) (Moore et al., 1982). Relevant best estimates of the physical properties of these materials are given in table 3-1 and discussed below.

	Grain size (µm)	Bulk density (kg/m^3)	Cohesion (kPa)	Angle of internal friction (degrees)	Fraction of area covered	Thermal inertia 10^{-3} cgs units)	Dielectric constant
Lander 1							
Drift material	0.1 - 10.0	1150 ± 150	1.6 ± 1.2 0-3.7	18.0 ± 2.4	0.14	3	2.35 2.11 - 2.62
Blocky material	0.1 - 1500	1600 ± 400	5.5 ± 2.7 2.2 - 10.6	30.8 ± 2.4	0.78	9.3 ± 0.5[1]	3.27 2.43 - 4.50
Rocks	35 x 10^3 240 x 10^3	2600	1000 - 10 000	40 - 60	0.08	40	8
Sample field		1624 1298 - 1850	—	—	1	—	3.33 2.61 - 4.32
Remote sensing		1612 1292 - 1857	—	—		9.0 ± 0.5	3.3 ± 0.7
		1486 1857 - 2026					3.0 4.0-4.6
Lander 2							
Crusty to cloddy material	0.1 - 10.0	1400 ± 200	1.1 ± 1.2 0 - 3.2	34.5 ± 4.7	0.86	6.3 ± 1.5[2]	2.81 2.43 - 3.27
Rocks	35 x 10^3 450 x 10^3	2600	1000 - 10 000	40 - 60	0.14	40	8
Sample field		1568 1396 - 1740	—	—	1		3.19 2.81 -3.64
Remote sensing			—	—	0.20 ± 0.10	8.0 ± 1.5 8.3 - 8.8	2.8 - 12.5

[1] Thermal inertia is 8.2 ± 1.4 if fraction of area covered by rock is taken as 0.15 ± 0.5 (see text)

[2] Thermal inertia is 5.6 ± 1.4 if fraction of area covered by rock is taken as 0.20 (see text)

N803200m

TABLE 3-1.- Estimates Mechanical Properties and Remote Sensing Signatures of the Surface Materials in the Sample Fields at the Viking Landing Sites.

3.2.3.1 Drift Material

Drift material, which occupies about 14 percent of the sample field of VL-1, has the characteristics of very fine-grained, porous materials with low cohesions; see figure 3-1(a). It has a consistency somewhat like baking flour. Sample trenches in drift material are typically 0.04 to 0.06 m deep and characterized by (1) steep walls along much of their lengths and at their tips, which have small, slumped units, (2) lumpy-appearing tailings and floors, (3) large amounts of tailings, (4) highly reflective surfaces on the floors and tailings where the sampler has tamped, rubbed, and compressed the material, and (5) smooth, domed surfaces around their tips.

Individual mineral or mineraloid grains in drift material are very small. Analyses of N_2 gas desorbed from a humidified sample in the biology GEX indicate that the specific area of drift material is 17 m^2/g (Ballou et al., 1978). This specific area implies that the sizes of individual mineral grains are about 0.14 mm, but geometrical sizes of the grains may be 10 to 100 times larger than those inferred from surface areas (Fanale et al., 1971). Quartz crushed to pass a 10 mm sieve and some natural clays have specific areas near 17 m^2/g (Brown et al., 1960; Mooney et al., 1952). A very fine grain size is also implied by the lack of erosion of drift material by engine exhausts during landing (Hutton et al., 1980; Moore et al., 1987). For erosion depths less than about 0.7 cm (Hutton et al., 1980), theory indicates particle sizes less than about 10 mm (Romine et al., 1973). Additionally, the smooth, highly reflective surfaces in trenches and tailings produced by the sampler indicate that the grains of drift material are very fine (Moore et al., 1977). Thus, the physical grain sizes of drift material may be estimated to be 0.1 to 10 mm. The lumps or very weak clods of disturbed drift material are aggregates of these very fine grains.

Large porosities, or low bulk densities, for undisturbed drift material are implied by the low bulk densities of the disturbed material estimated with the x-ray fluorescence spectrometer (XRFS), the reaction of the material to foot-

▲ (a) VL-1 sampler inserted in drift material (near center). Note lumpy objects of drift material next to sampler and smooth, but deformed surface beyond. Rock 3 (Sponge), at upper left, is about 0.23 m wide. Magnet cleaning brush is at lower left. Sun is at upper left (Frame 11H187/612).

(b) VL-2 sampler inserted in crusty material (near center). Note disrupted and tilted tabular units of crust to left of sampler. Rocks surround sampler on all sides; small rock to left of sampler is about 0.08 m wide. Dark band at right is sampler boom. Sun is at left (Frame 21H031/595). ▼

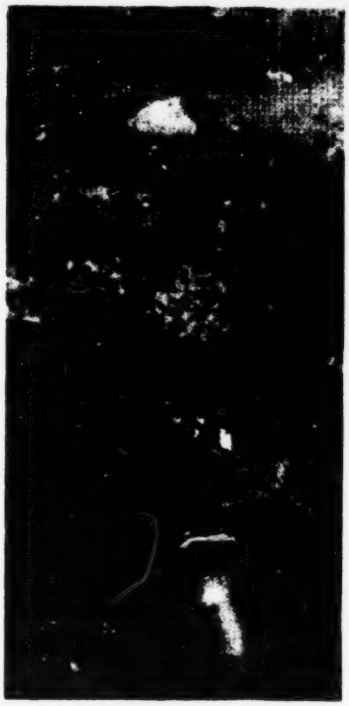

▲ (c) Trenches excavated in blocky material. Note blocky units of clods at tips of trenches. Far trench is 0.09 m wide; largest clods are 0.04 m across. Sun is at upper right (Frame 12B188/093).

Figure 3-1.- Photographs illustrating surface materials at the Viking landing sites.

ORIGINAL PAGE IS
OF POOR QUALITY

of internal friction estimated from surface deformations in front of the sampler during trenching. For the disturbed state, the bulk density of drift material in the XRFS analysis chamber is near 1100 ± 150 kg/m^3 (Clark et al., 1977). For the undisturbed state, an interpretation of full- and $^3/_8$-scale dynamic footpad penetration tests indicate that the strength properties of drift material are consistent with a lunar nominal test material that has a bulk density near 1300 kg/m^3 (Moore et al., 1977), but other materials may have similar strength properties at smaller bulk densities (Moore et al., 1987). The large penetration of, deformation around, and the infilling of the deeply buried footpad 2 are consistent with a porous, low-density, soil-like material that has a small angle of internal friction. Similarly, the small angles of internal friction (18.0 ± 2.4°) deduced from analyses of the sample trenches and surface bearing tests (Moore et al., 1987, 1982) are consistent with a low bulk density. As a best estimate, the bulk density of undisturbed drift material may be taken as 1150 ± 150 kg/m^3. Porosities for these bulk densities range between about 0.50 and 0.62 if the density of the individual mineral grains is 2600 kg/m^3.

Drift material possesses cohesion which may be, in part, due to cementation. The average cohesion of drift material is near 1.6 ± 1.2 kPa; the cohesions range between 0 and 3.7 kPa (Moore et al., 1987, 1982). The variations of cohesions may be related to planes of weakness between cross-laminations or fractures.

3.2.3.2 Crusty to Cloddy Material

Crusty to cloddy material, which occupies about 86 percent of the sample field of VL-2, has the characteristics of moderately dense soils; see figure 3-1(b). Sample trenches in crusty to cloddy material are typically 0.04 - 0.05 m deep and are characterized by (1) steep and irregular slopes at their tips and moderate slopes elsewhere, (2) generally fine-grained tailings interspersed with moderate size (0.02 m) equidimensional clods and slabs of crust, (3) modest amounts of tailings, (4) large (~0.04 m) clods and slabs of crust that have fallen into the trenches, and (5) disrupted areas around their tips. In contrast with the smooth, domed surfaces at the tips of trenches in drift material, the disrupted areas at the tips of trenches in crusty to cloddy material are composed of mixed fines and broken slabs of crust that have been displaced upward or regular polygonal prisms that have separated along fractures and been displaced upward. The polygonal prismatic forms of broken crusts and clods in the tailings are quite different from the irregular-shaped weak lumps in the tailings of trenches in drift material.

Individual mineral or mineraloid grains in the crusts and clods, like those in drift material, are very fine. The amounts of gases desorbed from humidified samples of crusty to cloddy material in the biology GEX are only slightly smaller than those of drift material, but this could be due to larger amounts of adsorbed water (Oyama and Berdahl, 1977). Thus, the sizes of the grains are near 0.1 to 10 mm. It is possible that millimeter-sized clodlets or aggregates of these very fine mineral-mineraloid grains are abundant in crusty to cloddy material because moderate increases in comminutor motor currents were observed while crushing the material (Moore et al., 1987). The presence of small, porous fragments or clodlets are also required to account for the rather low bulk densities estimated with the XRFS (Clark, B. C.; Weldon, Ray; and Castro, A. J., person. comm., 1978). The relatively large amount of erosion by the engine exhaust gases during landing is related to the presence of fractured crusts, prismatic clods, and clodlets which produce a larger "effective grain size" than that of drift material. During endeavors to collect samples of "rock" fragments between 0.2 and 1.25 cm in diameter, no samples were delivered for analyses in the XRFS chamber. Thus, strong pieces of crusts, clods, or rock fragments in this size range that are capable of surviving the sieving procedures used to collect the coarse fraction are not present in crusty to cloddy material. The crusts and clods could be disaggregated with finger pressure.

The average angle of internal friction of crusty to cloddy material is 34.5° ± 4.7° and is consistent with a soil-like material that has an undisturbed bulk density near 1400 ± 200 kg/m^3. This estimate of bulk density is taken as the best estimate for crusty to cloddy material (but it should be realized that dielectric constants (discussed later) were considered in making this estimate (Moore et al., 1987, 1982)).

Layers of crust in crusty to cloddy material clearly suggest that cementation of the very fine grains is partly responsible for the cohesion. The average cohesion of crusty to cloddy material is 1.1 ± 1.2 kPa; cohesions range from 0 - 3.2 kPa (Moore et al., 1987, 1982). Although the average cohesions of crusty to cloddy and drift materials from the analyses of a number of trenches are about the same, the contrasts between the tabular crusts and prismatic clods of disrupted crusty to cloddy material and the weak lumps of disrupted drift materials suggest that the cohesions of crusty to cloddy materials are typically larger than those of drift material — especially near the surface.

3.2.3.3 Blocky Material

Blocky material, which occupies 78 percent of the sample field of VL-1, has the largest overall strength of the three soil-like materials at the sites; see figure 3-1(c). Sample trenches in blocky material are typically 0.03 - 0.04 m deep and characterized by (1) moderately to steeply sloping walls at their tips but moderately sloping elsewhere, (2) tailings and floors that appear rubbly because they are littered with distinct fragments and clods, (3) walls at their tips that generally appear blocky, and (4) surfaces around their tips that are displaced upward and appear blocky in places.

The grain size of blocky material is unknown because the material was never analyzed by the GEX (Oyama aud Berdahl, 1977; Moore et al., 1987). The similarities in the chemical composition of blocky, drift, and crusty to cloddy materials and the fact that some surfaces that were tamped and rubbed by the sampler are smooth and reflective argue for a very fine grain size. On the other hand, the very large increases in comminutor motor currents while crushing blocky material are consistent with abundant millimeter-size fragments of materials like silicates, heavy metal oxides, or indurated shales. It is clear that strong, cohesive clods and fragments are present in blocky materials because samples of the coarse fraction were delivered for analyses in the XRFS chamber and large fragments of blocky material clogged the XRFS sample delivery port by the end of the extended mission. Most of the clods and fragments that clogged the delivery port were reddish in color like the VL-1 soil-like materials, but others are darkly colored like the rocks (Dale-Bannister et al., 1988).

Bulk densities of the clods and fragments of blocky material could be quite large. Samples of the coarse fraction in the XRFS chamber had estimated bulk densities of 570 to 940 kg/m^3 (Clark, B. C.; Weldon, Ray; and Castro, A. J.; person. comm., 1978). On Earth, tests indicate that coarse objects in the XRFS analysis chamber occupy about 50 percent of the volume of the chamber, but experience with drift material suggests that 62 percent is possible on Mars. For the first porosity, bulk densities of the coarse objects or clods would range between 1140 and 1940 kg/m^3 and, for the second, they would range between 1500 and 2474 kg/m^3. The penetration of footpad 2 into blocky material during landing is consistent with a lunar nominal material that has a bulk density near 2300 kg/m^3 (Moore et al., 1977). Thus, a large bulk density appears probable for blocky material in the undisturbed state and 1600 ± 400 kg/m^3 is taken as a best estimate. However, the angle of internal friction is about 30.8° ± 2.4° and somewhat smaller than would be expected for a soil-like material with a bulk density of 1600 kg/m^3.

The cohesion of blocky material is probably related to cementation by some sulfur and chlorine compounds because chemical analyses of the coarse fraction show an enrichment of these elements (Clark et al., 1982). The cohesion of blocky material is the largest of the three soil-like materials and averages 5.5 ± 2.7 kPa with a range between 2.2 and 10.6 kPa.

An appreciation for the relative strengths of drift and blocky materials can be gained by inspection of figure 3-2.

3.2.3.4 Rocks

Rocks with diameters of 0.035 to 0.23 m occupy 8 percent of the sample field of VL-1, and rocks with diameters of 0.035 to 0.45 m occupy 14 percent of the sample field of VL-2. Little is known about the rocks. Some of the rocks appear to be dense and fine-grained, others appear to be vesicular, and others may be breccias (Sharp and Malin, 1984; Garvin et al., 1981). The Viking surface sampler did not chip, scratch, or spall the surfaces which were exposed to the atmosphere of those rocks that it pushed or scraped, so it is apparent that they do not have weak, punky rinds (Moore et al., 1987, 1977). Rock surfaces are gray in color where not covered by a few micrometers of dust (Adams et al., 1986). Because demonstrable rock fragments were never analyzed with the XRFS, rock compositions are unknown. Most scientists believe that they are mafic rocks (Guinness et al., 1987) such as basalts, basaltic andesites, or andesites (Adams et al., 1986). Because so little is known about the rocks, a bulk density of 2600 kg/m^3 can be assigned to the rocks and rock fragments by analogy with common dense terrestrial rocks, but there could be some variations due to variations in porosity. Cohesions are probably on the order of 10^3-10^4 kPa and angles of internal friction in the range of 40-60°, also by analogy with common terrestrial rocks.

The size-frequency distributions of the rock fragments and blocks in the sample fields are understood and small rock fragments are conspicuously absent. Despite some 65 attempts to collect and deliver the coarse fraction (0.2 - 1.25 cm) for analyses in the XRFS chambers (Moore et al., 1987), no sample was ever received by VL-2 and the coarse fractions analyzed by VL-1 had chemical compositions that were remarkably similar to those of drift and crusty to cloddy materials (Clark et al., 1982). Apparently, the dark fragments on the XRFS delivery port either were similar in composition to the soil-like materials, were not abundant enough to be detected, were previously unsampled, or were masked by fines in the analysis chamber. There was no evidence for a coarse fraction in drift material other than weak lumps. If significant concentrations of small, unaltered rock fragments are present at the sites, they must be buried by the soil-like materials to depths greater than the deepest trenches excavated by the samplers, which were near 0.1 - 0.2 m deep.

Although size-frequency distributions of rocks in the sample field are well established, those in the far field are not well established. The abundance of rocks, the viewing conditions, and the complicated nature of the surface place severe restrictions on the ability to obtain meaningful size-frequency distributions of rocks. Distributions as seen within the sample field extend to rock diameters of about 0.2 m at the VL-1 site and 0.4 m at the VL-2 site (Moore et al., 1979; Binder et al., 1977) but there are clearly rocks larger than these in the far fields. If some of the large rocks beyond the sample field of VL-2 are included, the cumulative frequency distribution of the rocks down to a diameter of 0.14 m can be represented by:

$$N = 0.013\ D^{-2.66}$$

where N is the cumulative frequency of rocks per meter-squared with diameters of D and larger. This implies that

ORIGINAL PAGE IS
OF POOR QUALITY

(a) Footpad 3 resting on blocky material which it penetrated about 4 cm during landing. Note small rocks, but smallest objects are clods. Sun is at right. (Frame 12A001/000.)

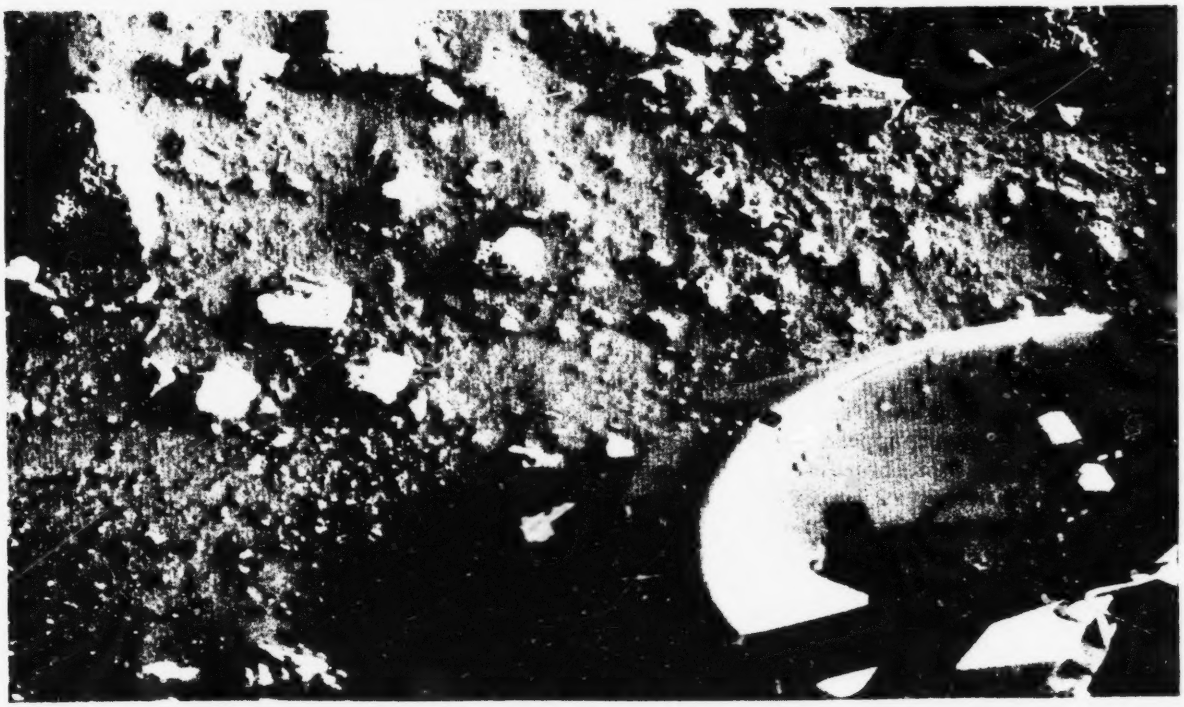

(b) Footpad 2 penetrated drift material 16.5 cm and became buried during landing. Undisturbed drift material lies beyond steep scarp at upper left; subtle depression in disturbed area lies above the buried perimeter of footpad 2. Lander 1 touched down at about 2.3 m/s. Radius of footpad is about 0.2 m. Sun is towards the top. (Frame 11A138/023.)

Figure 3-2.- VL-1 photographs illustrating relative strengths of blockly and drift materials.

the cumulative fraction of area (A) covered by assumed circular rocks with diameters of D and larger is:

$$A = 0.0408\ D^{-0.66}$$

With this relation, the cumulative fraction of area covered by rocks 0.14 m and larger comes out to be 0.148. From the sample field data, the additional area covered by rock fragments between 0.1 and 0.14 m is 0.016, and for rocks .035 to 0.1 m the additional area is 0.04. Thus, all rocks and rock fragments could cover 18.8 percent of the area and those greater than 0.1 m could cover 16.4 percent of the area. The VL-1 size frequency distribution presents a problem because the fraction of area covered by rock fragments in logarithmic diameter bins is nearly constant within the sample field (Moore et al., 1979) and the upper limit of rock diameters is difficult to assess.

3.2.4 Average Bulk Density

Average bulk densities for the entire sample fields can be calculated from the fractions of areas occupied by each component and their estimated bulk densities. For the three components of VL-1, the bulk density of the entire sample field is 1624 kg/m^3 (range: 1298- 1950).[4] For VL-2, the bulk density is 1568 kg/m^3 (range: 1396-1740); using a fraction of area covered by rocks of 0.188, instead of 0.14, would change the bulk density of the general area to 1625 kg/m^3 (range: 1463 - 1788).

3.2.5 Dielectric Constants

Dielectric constants for the landing sites have been estimated with the lander-orbiter radio relay links, and they have been estimated from radar reflectivities of quasi-specular echoes for the general areas of the landing sites. For VL-1, the dielectric constant from the lander-orbiter radio link is 3.3 ± 0.7 (Tang et al., 1977). For this determination, radar waves with 78.7-cm wavelengths (381 MHz) were transmitted by the lander and echoes from the surface were received by the orbiters. The antennae are located on the back-left side of the landers so that the reflections did nor come from the sample field but from an area behind the lander which appears similar to the sample field. The echoes came from a broad area 1.7 to ≈10 m from the lander and from the upper 2.5 m of the surface (Tang et al., 1977). Because of the large area and depths sampled, the derived dielectric constant is likely to represent an average for the entire sample field. The derived dielectric constant can be compared with those computed with reflectivities from broad areas (≈600 km in diameter) in the general vicinity of the site that was obtained by terrestrial-based radars. During the Viking site certification efforts that employed 12.6-cm wavelength continuous-wave radio transmissions, a reflectivity near 0.074 is estimated for the general area of VL-1 (Simpson et al., 1978; Tyler et al., 1976), and this corresponds to a dielectric constant near 3.0. Here, the diffuse component of the radar echo is not separately evaluated. About 460 km to the east and west of the VL-1 landing site, reflectivities from continuous wave spectra between 0.11 and 0.13 are estimated using a technique that accounts for the diffuse component of the echo (Harmon and Ostro, 1985), and these reflectivities correspond to dielectric constants of 4.0 and 4.6, respectively.

Dielectric constants of the materials in the sample fields can be estimated from their bulk densities using laboratory data on rocks and dry rock powders (Campbell and Ulrichs, 1969). Such estimates are model dependent because dielectric constants depend on the compositions of the materials and their bulk densities. It should also be realized that the dielectric constant is related to the bulk density of the material and independent of mechanical properties such as cohesion and grain size. Strong cohesive rocks such as porous vesicular basalts or pumice with variable bulk densities would suffice as well as powders provided that the pores or vesicles are much smaller than the radar wavelength. For example, the dielectric constants of a basalt powder or sand and a strong vesicular basalt would be the same when their bulk densities are the same. However, the soil-like materials of Mars are akin to powders and not vesicular rocks. Most dry rock powders with bulk densities near 1000 kg/m^3 have dielectric constants between 1.8 and 2.1, but those produced from silicic rocks, such as granite, tend to be near 1.8 and those produced from mafic rocks, such as basalts, tend to be near 2.0. Dielectric constants of dry rock powders with 40 percent porosity range from about 2.6 for silicic (granite) powders to about 3.4 for mafic (basalt) powders. The dense rocks have dielectric constants that range from 5 (granite) to 9 (basalt). The mafic chemical compositions of the soil-like materials on Mars (Toulmin et al., 1977; Clark et al., 1982) suggest that a model for basalt and basalt powders is more likely than one for silicic rocks. Here, it is assumed that the soil-like materials are composed of powders derived from basaltic rocks with zero porosity, a bulk density of 2600 kg/m^3, and a dielectric constant of 8. The Rayleigh mixing formula (Campbell and Ulrichs, 1969) is then used to calculate the dielectric constants using the estimated bulk densities and vice versa; see figure 3-3.

Using the procedures above, the bulk density for the lander-orbiter dielectric constant (3.3 ± 0.7) is 1612 kg/m^3 (range: 1292 - 1857). For the Earth-based radar data, bulk densities are 1486, 1857, and 2026 kg/m^3 for dielectric constants of 3.0, 4.0, and 4.6, respectively. These bulk densities compare well with the 1624 kg/m^3 (range: 1298 - 1950) estimated for the entire sample field (see section 3.2.3) and earlier results that use a less constrained model

---

[4] Here, and elsewhere, calculated bulk densities are given to four figures for illustrative purposes, but they are only significant to about two figures.

(Moore et al., 1987). It is noteworthy that the range of estimated bulk densities of drift material is essentially excluded from the range of bulk densities calculated because the fraction of area covered by drift material and its bulk density are small.

The problem can be turned around to estimate the dielectric constants of the soil-like materials from their bulk densities. Drift material, according to the model, has a dielectric constant of 2.35 (range: 2.11 - 2.62)[5] and that of blocky material is 3.27 (range: 2.43 - 4.50).

Radar data on the VL-2 site are either lacking or of poor quality. The site is not accessible to the terrestrial-based radars. Additionally, the nearest Viking orbiter bistatic radar ground track is some 10° or so to the south, and no reflectivities are reported. Dielectric constants obtained using the lander-orbiter relay link range from 2.8 to 12.5 (Tang et al., 1977). This range of values is so large that it provides little useful information. The low estimate of the dielectric constant gives a bulk density of 1393 kg/m^3 which is consistent with the large angle of internal friction of crusty to cloddy material. The upper limit of 12.5 is more consistent with some meteorites than with dense mafic igneous rocks (see for examples, Campbell and Ulrichs, 1969). Based on the densities of the components, the dielectric constant of the sample field should be near 3.19 (range: 2.81 - 3.64), or slightly smaller than that of VL-1. For crusty to cloddy material, the value is 2.81 (range: 2.43 - 3.27).

There are several reasons why the estimates above should be viewed with some caution. First, it is not possible to settle on a unique model from the data because there are other plausible materials and values that could be used. Some of these variables are embodied in the data on rocks and dry rock powders (Campbell and Ulrichs, 1969). The mineralogy of the soil-like materials is unknown so that materials other than dry rock powders are possible. One such material is clay (Banin and Rishpon, 1979). Dry, clayey soils with bulk densities of 1200 -1300 kg/m^3 have dielectric constants near 3 when measured at 7.5-cm and 60-cm wavelengths (Hoekstra and Delaney, 1974). Dielectric constants near 2.5 have been obtained at 10 and 100-cm wavelengths for dry, sandy, silty, and clayey soils with unspecified bulk densities (Von Hippel, 1954). However, for plausible geologic materials, dielectric constants near 2 imply low bulk densities that are near 1000 kg/m^3 (fig. 3-3). Second, the problem of diffuse scattering of the radio waves by surface and subsurface discontinuities that are about the same size as the wavelength of the radar (such as rocks, crater forms, and irregularities along contacts between depositional units) has not been fully addressed. This is probably more important at the 12.6-cm wavelength of the Earth-based radar than at the 78.7-cm lander wavelength because smaller rocks are commonly more abundant than larger rocks. Third, the Earth-based radar footprint is large compared to the landing site and to the size of the sample field, so that other materials not represented at the landing sites and in the sample field could be present along with the materials in the sample fields and at the landing sites. Fourth, the analyses compare inferred properties of materials from the uppermost 0.1 - 0.3 m with radar properties which may apply to materials at depths measured in meters.

3.2.6 Thermal Inertias

Bulk thermal inertias for broad areas (60 km x 60 km) that include the Viking landing sites are 9.0 ± 0.5 (VL-1) and 8.0 ± 1.5[6] (VL-2) (Kieffer, 1976). These thermal inertias are large when compared with those of most of Mars (Palluconi and Kieffer, 1981; Jakosky and Christensen, 1986a). Spectral differencing techniques allow estimates of the fraction of surface covered by "rocks" and of the thermal inertia of the remaining part (the fine component) (Christensen, 1982, 1986a,b; Kieffer et al., 1977). "Rocks" are assumed to have a thermal inertia of 30 which corresponds to a rock about 0.1 m across (see Kieffer et al., 1973). The actual situation is more complicated than most models assume for several reasons. First, the apparent thermal inertias of rocks vary depending on the size of the rock. For example, thermal inertias of rock outcrops and rocks larger than about 0.3 m have inertias near 55 and those smaller than 0.3 m have inertias that decrease in some way to a limiting value of 10 at the 0.01 - 0.03 m sizes (Jakosky, 1986). Second, thermal inertias of materials with uniform particles remain near 10 down to grain sizes near 500 - 1000 mm because of the thermal conductivity of the pore gas (Jakosky, 1986), rather than decreasing in a uniform manner. Below 500 mm, thermal inertias decrease in a uniform manner from 10 to 1 or 2 at the 1 - 10 mm sizes. Third, thermal inertias of finer-grained materials are uncertain but are probably near 1 - 3. Finally, although it appears reasonable to consider the VL-2 landing site a two component system of fines and rocks, the VL-1 site is clearly at least a three component system.

For the VL-1 site, the fraction of the surface covered by "rocks" is estimated to be about 0.15 ± 0.05 from the thermal data, and the thermal inertia of the remaining fraction is about 7.5; for the VL-2 site, the fraction of area covered by "rocks" is 0.20 ± 0.10 from the thermal data and the thermal inertia of the remaining components is about

---

[5] Here, and elsewhere, dielectric constants inferred from bulk densities are given in three figures for illustrative purposes, but they are only significant to about two figures.

[6] Thermal inertias are reported in units 10^{-3} cal cm^{-2} s$^{-1/2}$K^{-1}

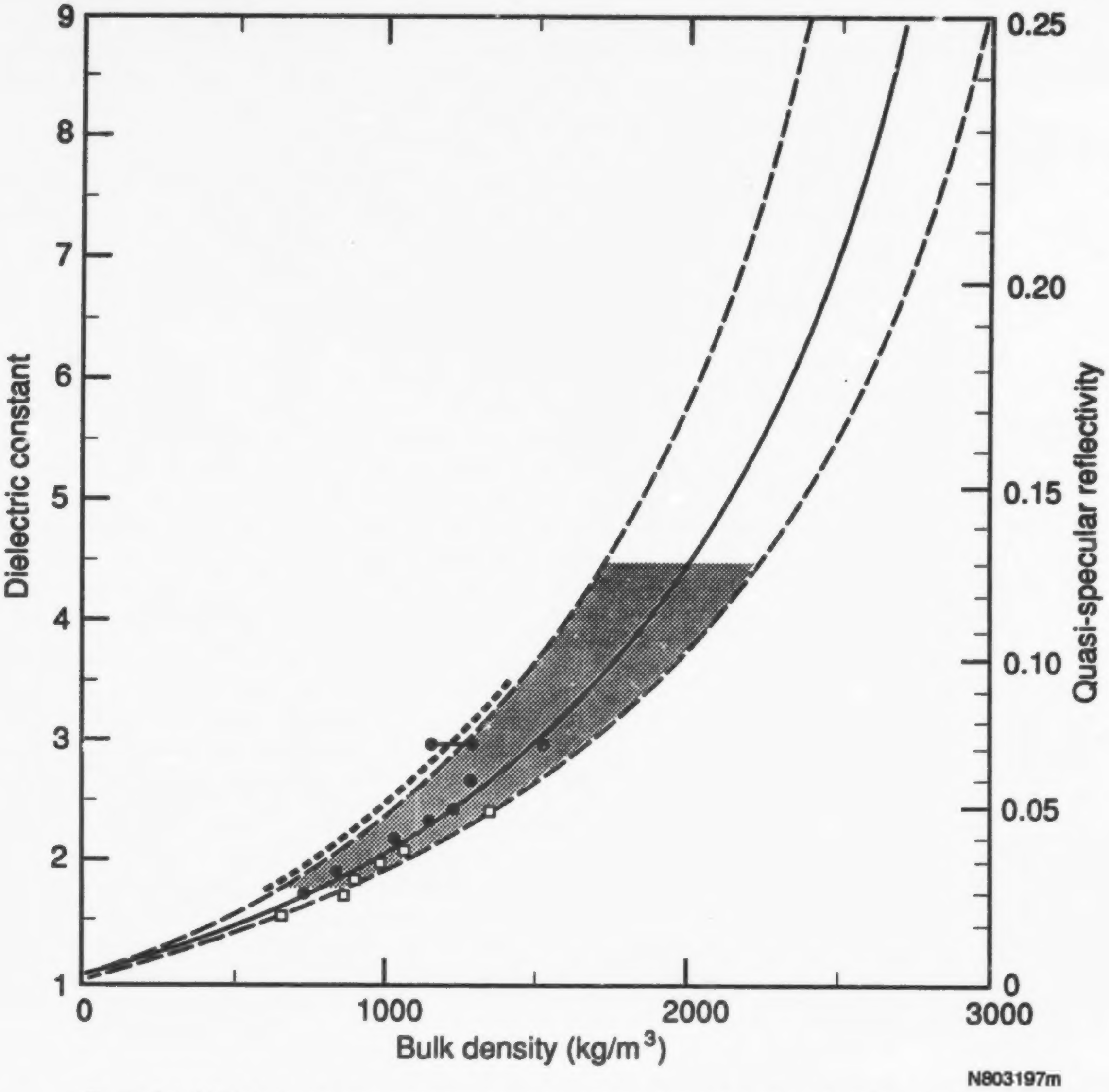

Figure 3-3.- Model relation between dielectric constant or quasi-specular echo reflectivity and bulk density (heavy solid line).

Dielectric constant is derived from reflectivity using the Fresnel reflection coefficient (see Tyler et al., 1976). Bulk density is calculated using the Rayleigh mixing formula (see Campbell and Ulrichs, 1969). A dielectric constant of 8 and a bulk density of 2600 kg/m^3 represents a "parent" basaltic rock. If the "parent" rock is powdered or becomes vesicular, the bulk density will decrease, and the porosity will increase, with a corresponding decrease in dielectric constant as described by the heavy solid line. Thus, a basalt powder or vesicular basalt with a bulk density of 1000 kg/m^3 will have a dielectric constant of 2.1. The soil-like materials of Mars are more akin to basalt powder than vesicular basalt. Dashed lines indicate the effect of a ± 25 percent error in reflectivity on the estimated bulk density. Cross-hatched area indicates the range of reflectivities for the northern latitudes of Mars (Harmon and Ostro, 1985; Harmon et al., 1982) and the corresponding dielectric constants and bulk densities. Heavy dashed line shows that a "parent" rock with a dielectric constant of 9 and a bulk density of 2700 kg/m^3 produces similar results. Data points (obtained graphically from Campbell and Ulrichs, 1969) for silicic powders of aplite granite (☐) and mafic powders of olivine basalt (dots) are shown for comparison with the model presented herein. Horizontal bar represents data for dry, clayey soil at 7.5-cm and 60-cm wavelengths (Hoekstra and Delaney, 1974); dotted line indicates calculated change of dielectric constant with bulk density. Note that a dielectric constant near 2 implies a bulk density near 1000 kg/m^3 for all materials.

8.0 (Christensen, 1982). These "rock" abundances are consistent with those observed at the landing site.

Estimates for the fine-component thermal inertias observed at the landing sites can also be made. This is done by assuming that the average thermal inertia of the entire rock population is 40 and the thermal inertias of the entire sample fields are the same as those obtained from orbit; then, the mixing curve presented in Kieffer et al., (fig. 10, 1977) is used. This analysis is similar to one by Moore et al., 1987. For the sample field of VL-1 with a thermal inertia of 9.0 ± 0.5 and the observed rock abundance (0.08), the fine-component inertia is about 8.0 ± 0.5. This fine component actually consists of drift and blocky materials. If the thermal inertia of drift material is taken to be 3, then the blocky material has a thermal inertia of about 9.3 ± 0.5. If the "rock" abundance (0.15 ± 0.05) is used, the fine-component inertia becomes 7.2 ± 1.0, and that of blocky material is 8.2 ± 1.4.

The low thermal inertia for drift material is based on several lines of evidence. First, the particle size is in the range of 0.1-10 mm. Second, the bulk density is very low and near 1150 kg/m^3. Third, the cohesion is very small. For fine-grained, unconsolidated, loose particulate materials, thermal inertias should be about 1 - 3 in martian conditions of temperature and atmospheric pressure (Kieffer et al., 1973; Jakosky, 1986). Laboratory measurements of the effects of particle size, compaction or bulk density, and cohesion on thermal conductivities at martian atmosphere pressures again show that fine-grained, low density materials with small cohesions are expected to have low thermal inertias (Wechsler and Glaser, 1965; Wechsler et al., 1972; Fountain and West, 1970). It is well established that thermal conductivities (and, hence, thermal inertias of particulate materials with moderate bulk densities that are more or less constant, and that have very small cohesions) decrease with decreasing particle size (see, for example, Jakosky, 1986), but data on loose to moderately dense materials with small cohesions and 0.1 - 10 mm particles are lacking. Perhaps the best available analog for drift material at this time is loose pumice powder, crushed to pass a 44 mm sieve, which has a bulk density of 880 kg/m^3 (Wechsler and Glaser, 1965). For nominal specific heats in the range of 0.16 - 0.20 cal $g^{-1}K^{-1}$, the thermal inertia of this powder would be near 2 to 2.5 at martian atmospheric pressures. Compaction of loose, fine-grained particulate materials increase their thermal inertias, bulk densities, and cohesions. The data of Fountain and West, 1970, for particulate basalt (37 - 62 mm) at martian pressures and temperatures suggest a weak dependence of thermal conductivities on bulk densities that range from 790 to 1500 kg/m^3. Thermal inertias calculated from their data are near 2.0 to 3.2 with lower thermal inertias corresponding to the lower bulk densities. Horai, 1979, calculated thermal inertias of 2 - 3 for loose (densities of 790 - 1500 kg/m^3) and 5 - 6 for dense, compacted (densities of 1700 - 1850 kg/m^3) lunar soil simulants from his data on thermal conductivities. There is also an increase in cohesion with compaction or increased bulk densities of lunar-like simulants (Mitchell et al., 1972).

For the sample field of VL-2 with a thermal inertia of 8.0 ± 1.5, the observed rock abundance (0.14) suggests that the fine component of the surface has a thermal inertia of 6.3 ± 1.5 (see Moore et al., 1987). As there is little or no drift or blocky materials, this value is the thermal inertia estimate for crusty to cloddy material. If the "rock" abundance (0.20 ± 0.10) is used, the thermal inertia of the fine component is 5.6 ± 1.4.

3.2.7 Surface and Soil Temperatures[7]

The annual temperature range for the martian surface at the Viking lander sites has been computed by Kieffer, 1976, on the basis of thermal parameters derived from observations made with the infrared thermal mappers (IRTM) on the Viking orbiters. Surface temperatures at the two sites for a martian year were computed and are presented in figure 3-4. Because the model parameters are derived from remote sensing observations, the temperature profiles represent an area-weighted average of the soil and rocks.

At midday, the temperature reaches a maximum near the autumn equinox (areocentric longitude $L_s = 180°$), rather than at midsummer, and has a secondary peak near the spring equinox ($L_s = 0°$). This large semiannual behavior results from the eccentricity of the orbit of Mars, tending to offset the effect of its polar tilt in the Northern Hemisphere (the effects add in the Southern Hemisphere).

The thermal behavior of the two sites is quite different. The VL-1 site is near the latitude which experiences the smallest annual variation of temperature. The VL-2 site, in contrast, has well-defined seasons. The maximum temperatures occur in the late summer and decrease steadily until midwinter.

With the Viking lander images used to estimate the rock component on the thermal emission, the daily temperature behavior of the soil alone was computed over the range of depths accessible to the landers. When the VL-1 and VL-2 sites were sampled, the daily temperature ranges at the top of the soil were 183 to 263 K and 183 to 268 K, respectively.

The computed range of subsurface temperatures for the Viking soils is shown in figure 3-5. The diurnal variation

---

[7] The materials of section 3.2.7 are excepted from "Soil and Surface Temperatures at the Viking Lander Sites," by H.H. Keiffer, 1976.

Figure 3-4.- Daily maximum, minimum, and average surface temperatures at the two Viking landing sites through a martian year. The maximum temperature occurs about 1 hr after noon; the minimum occurs at dawn (Kieffer, 1976).

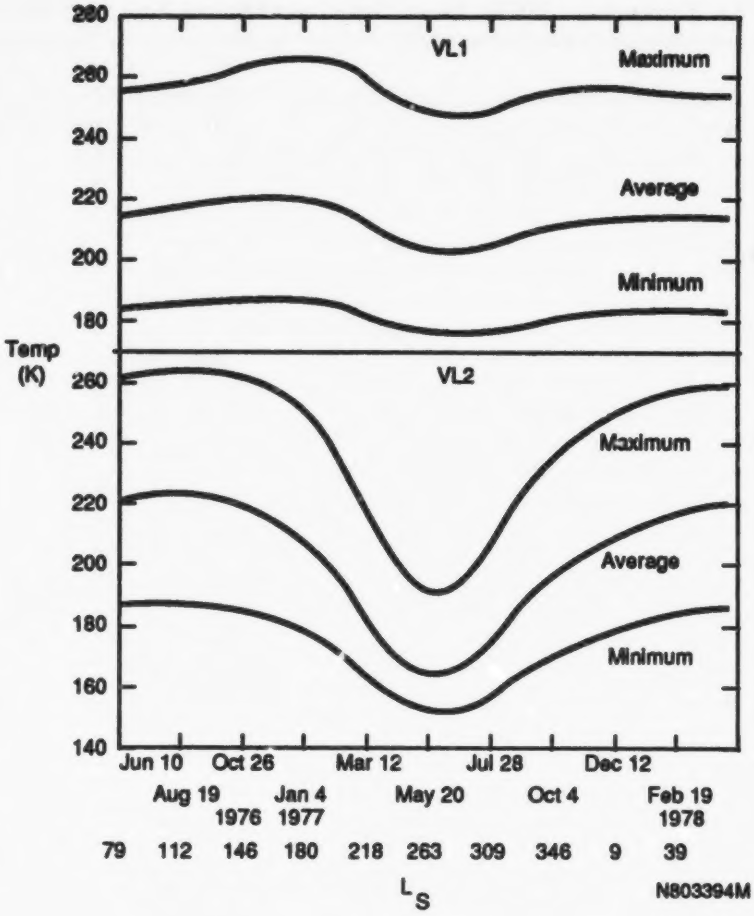

Figure 3-5.- Temperatures for the soils at the Viking lander sites. The two envelopes (right) show the temperature extremes as a function of depth for the average VL-1 (22° N) and VL-2 (48° N) soils. The subsurface temperature profiles for somewhat finer-grained material at the VL-1 site are shown at 4-hour (4/24 of a martian day) intervals (left) (Kieffer, 1976).

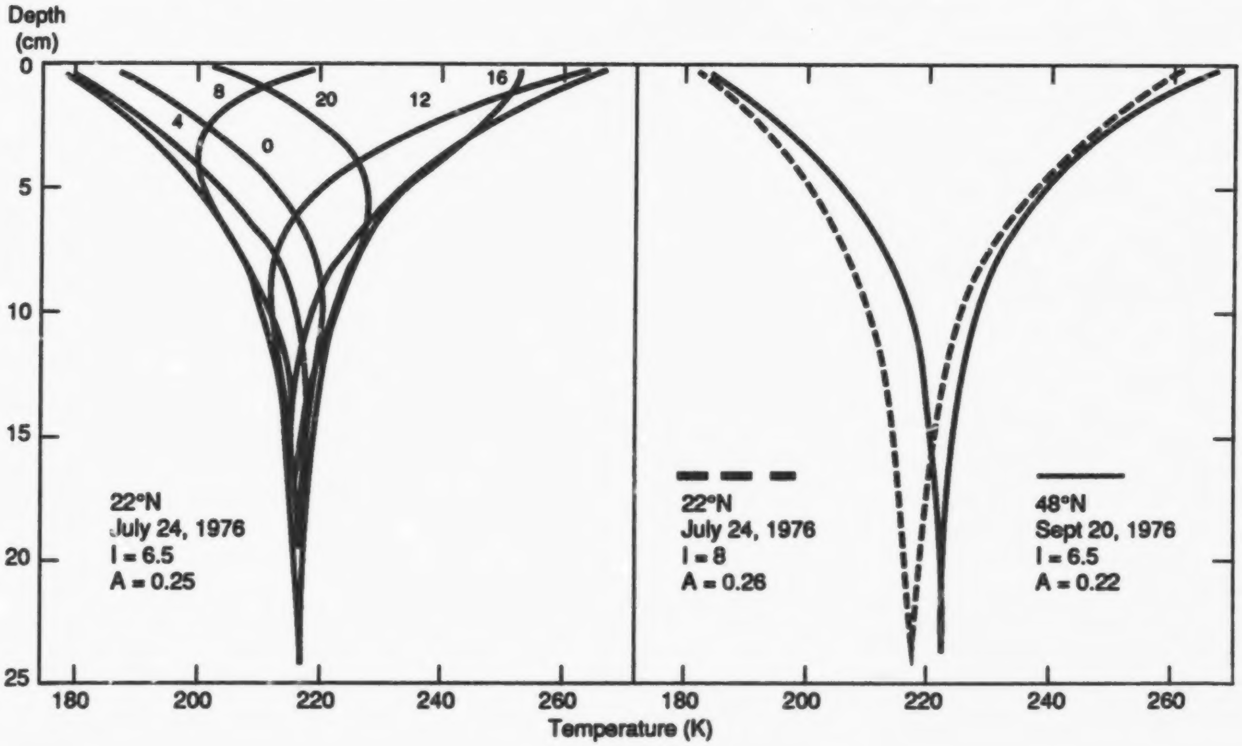

decreases with depth with an exponential scale of about 5 cm. The temperatures at a depth of 24 cm differ negligibly from the average surface temperatures, 217 and 222 K at VL-1 and VL-2, respectively. The maximum temperature of the soil sampled from beneath rocks at the VL-2 site was calculated to be 230 K.

3.3 GLOBAL COMPARISONS

In this section, the estimated values of dielectric constants and thermal inertias at the Viking landing sites are compared with values measured on a more global basis using remote sensing techniques.

To recapitulate, the landing sites contain four materials at the surface:

(1) Drift material is a loose, unconsolidated dust with a particle size in the range of 0.1 - 10 mm, a bulk density near 1150 kg/m^3, a dielectric constant near 2.4, and a thermal inertia in the range of 1 - 3. (2) Crusty to cloddy material has small, but variable cohesions, a moderate bulk density near 1400 kg/m^3, a dielectric constant near 2.8, and a thermal inertia near 4 - 7. The cohesion is, in part, related to cementation by some sulfur- and chlorine-bearing compounds. This cementation is responsible for the crusts and prismatic clods. (3) Blocky material has the largest cohesion of the soil-like materials, a bulk density near 1600 kg/m^3, a dielectric constant near 3.3, and a thermal inertia near 7 to 9. The cohesion of blocky material is partly related to cementation of grains by salts of sulfur and chlorine. (4) Rocks have very large cohesions, bulk densities near 2600 kg/m^3, dielectric constants near 8, and thermal inertias between 30 - 60.

The estimated dielectric constants for the components observed at the landing sites can be compared with those derived for larger areas on a regional and global basis. The literature on radar echoes report the reflectivities of the quasi-specular echoes. Hence, when dielectric constants are presented herein, the reflectivities of the quasi-specular echoes immediately follow in parentheses.

The average dielectric constant for Mars is about 3.0 (0.07) at 12.6-cm wavelength (Downs et al., 1975), but there are considerable variations in magnitudes. For the Tharsis region (near 22° N), the average reflectivity and standard deviation of reflectivity (0.041 ± 0.015) from analyses of echoes from continuous-wave dual polarization observations (Harmon et al., 1982) imply an average dielectric constant of 2.3 and a standard deviation of about 0.4. Elsewhere in the north, the average is about 3.7 (0.101 ± 0.023) (Harmon and Ostro, 1985). In the southern latitude band (14° S - 22° S), delay-Doppler observations indicate that below-average dielectric constants chiefly are found in the Tharsis region south of Arsia Mons, near Mangala Vallis, and near Eos Chasma, while they are above average between 0° and 110° W (Downs et al., 1975, 1973). Some dielectric constants that are near 7 (0.20) (Downs et al., 1975) suggest that there are large rocks or extensive rock units at or near the surface. Some reflectivities from the delay-Doppler observations are less that 1 to 2 percent (Downs et al., 1975), corresponding to dielectric constants less than 1.5 to 1.8, but these low values may not represent the values for the actual surfaces (Downs et al., 1975). For this reason, the lower bound for martian dielectric constants may be considered to be about 2.3 ± 0.4 (figs. 3-3 and 3-6).

As mapped between ±60° latitude at a scale of approximately 120 km, the thermal inertia is seen to vary geographically with large expanses of nearly constant thermal inertia; the probability density of the inertia values is bimodal with modes at about 3 and 7 and a total range of about 1 to 15 (Palluconi and Kieffer, 1981). Low thermal inertia (1 - 4) areas, which occupy 20 percent of the area sampled, include Amazonis Planitia, the Tharsis region, around Elysium Mons, and Arabia. High thermal inertia (8 - 15) areas, which also occupy 20 percent of the area sampled, include Argyre, Hellas, Isidis, Utopia, Acidalia Planitia, and Valles Marineris. The remaining 60 percent of the area sampled has intermediate thermal inertia.

Dielectric constants and thermal inertias at the same locations on Mars are positively correlated (Jakosky and Christensen, 1986a,b; Jakosky and Muhleman, 1981). For example, between 14° and 22° S, a correlation of quasi-specular reflectivities obtained with 12.5-cm radar and thermal inertias (Jakosky and Christensen, 1986a) is bimodal with one mode near a dielectric constant of 1.8 (0.015) and a thermal inertia of 2.2, and a second mode near a dielectric constant of 3.0 (0.07) and a thermal inertia of 6. This second mode is stronger than the first and implies that most of the materials in this region have these properties. Similar results are obtained near 22° N (Jakosky and Muhleman, 1981). Comparisons of more recent radar data (Harmon and Ostro, 1985; Harmon et al., 1982) and thermal inertia maps (Palluconi and Kieffer, 1981; Christensen, 1986a) support the positive correlation between dielectric constants and thermal inertias (fig. 3-6).

Low values of thermal inertias are inferred to be large areas of fine-grained dust deposits (Kieffer et al., 1977). The particle size is less than 50 mm, and probably in the range 1-20 mm (Kieffer et al., 1973; Jakosky, 1986). Small thermal skin depths require that these deposits are at least several centimeters thick (Jakosky, 1986), and analysis of image and radar data suggest dust mantling more than 1-2 m thick (Christensen, 1986a). This interpretation is consistent with bulk densities inferred from radar reflectivity data (Jakosky and Christensen, 1986). Because of the small particle size of airborne dust (e.g., Toon et al., 1977; Pollack et al., 1979), regions of low-inertia probably represent deposits of airfall dust (Zimbelman and Kieffer, 1979; Christensen, 1986a), but airfall dusts and reworked airfall dusts from volcanic eruptions cannot be excluded because

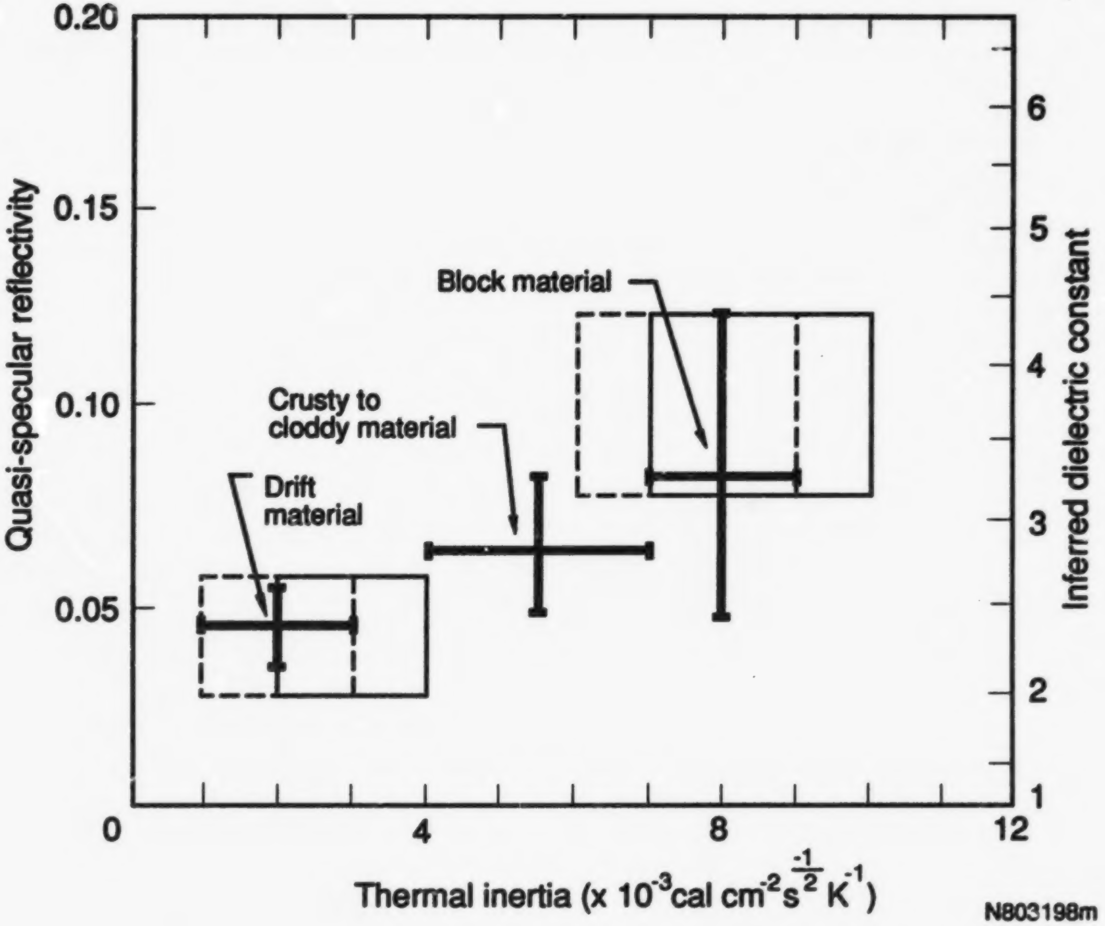

Figure 3-6.- Correlation between quasi-specular echo reflectivity (and dielectric constant) and thermal inertia.

Rectangles represent algebraic standard deviations of reflectivities (from Harmon and Ostro, 1985, and Harmon et al., 1982) and ranges of thermal inertias (obtained graphically from Paluconi and Kieffer, 1981). Fine component thermal inertias (dashed boxes) would displace boxes about one abscissa unit to the left (Christensen, 1982). Crosses represent estimates for surface materials at the Viking landing sites (except rocks). Range for crusty to cloddy material includes the principal mode described by Jakosky and Christensen (1986a).

small dielectric constants and low inertias are associated with the volcanos and volcanic terrains of the Tharsis and Elysium regions. The relatively large amounts of sulfur and chlorine in the lander soil-like material would support this contention (Settle, 1979). The small dielectric constants and low thermal inertias are very similar to those of drift material at the VL-1 site so it is inferred that material on a global scale with small dielectric constants and low thermal inertias are similar to drift material in mode of origin as well as mechanical properties. The lack of thicker and more extensive drift deposits at the VL-1 site is probably related to a general deflation of the region (Mutch et al., 1976b; Arvidson et al., 1979) or to the occasional removal of dust (Arvidson et al., 1983; Moore, 1985; Jakosky and Christensen, 1986), combined with the meteorological control of regions of deposition of new dust (Zurek, 1987).

Thus, the combination of a low thermal inertia and a small dielectric constant suggests the presence of a significant thickness of a porous, compressible, soil-like material with a low cohesion and small angle of internal friction. It is estimated that the dielectric constant of drift material is between 2.1 and 2.5, corresponding to a bulk density between about 1000 and 1300 kg/m^3. The thermal inertia is estimated to be within the range from 1 to 3. Footpad 2 of VL-1 penetrated drift material some 0.16 m upon landing at 2.3 m/s. Because vast expanses of materials with small dielectric constants and low thermal inertias, such as the Tharsis and Arabia regions, are thought to be similar to this material, the surfaces in those regions could present serious problems to landing spacecraft and other vehicles that are not suitably designed.

The interpretation for regions of high thermal inertia is more problematical. While only loose, fine dust can have a low thermal inertia, a higher value can result from: (1) cementation, which bonds fine particles together, (2) compaction, which will increase both the bulk density, conductivity, and cohesion of fine particles, (3) a matrix of larger particles with a correspondingly larger bulk thermal conductivity, or (4) the presence of coarse particles within a matrix of fine particles. Based on a comparison of the thermal and radar properties on a global basis, cementation or bonding is a likely cause of high thermal inertias (Jakosky and Christensen, 1986); certainly, however, many regions will depart from this general trend. Both crusty to cloddy and blocky materials have cohesions that are partly due to cementation and they have bulk densities that are relatively large; both of these properties would contribute to a high thermal inertia. Blocky material also contains relatively coarse particles along with fine particles. The difference in bulk density between the materials at the lander sites is not sufficient to account for the large variations in thermal inertia so that cementation is required. It is imagined that surfaces consisting predominantly of moderately dense, cemented or bonded materials, analogous to crusty to cloddy and blocky materials at the lander sites and comprising the bulk of the regions of high thermal inertia and moderate dielectric constant, would represent no serious problems to landing spacecraft and traversing vehicles. Both the radar and thermal data indicate that these types of materials are more prevalent on Mars than the compressible materials with low bulk densities, small dielectric constants, and low thermal inertias.

In summary, drift material at the VL-1 site is probably a good analog for materials in the Tharsis region of Mars and elsewhere where dielectric constants are small and thermal inertias are low because drift material has a small dielectric constant and a low thermal inertia. Crusty to cloddy material is probably a good analog for much of the materials of Mars because its dielectric constant and thermal inertia are nearly the same as the principal modal value of Jakosky and Christensen (1986a). Blocky material represents a denser and better cemented soil-like material because its dielectric constant and thermal inertia are larger and higher than the principal modal value described in Jakosky and Christensen (1986a).

There are, of course, problems related to the interpretation of thermal inertia and dielectric constant values on a global basis. The thermal inertia values apply, in a bulk sense, to the uppermost 0.01-0.1 m of the surface materials because this is the depth to which energy can conduct over the course of a day. The radar reflectivities apply to materials to much greater depths below the surface. Calculations for the power attenuation of 12.6-cm radar (Von Hipple, 1954) in materials with loss tangents and dielectric constants consistent with dense and powdered basalt (Campbell and Ulrichs, 1969) indicate that the uppermost 0.3 m of a dense basalt would be sampled by the radar; for rock powders with a dielectric constant of 2, the uppermost 6 m would be sampled. Variations in the correlations between these properties can then be explained by the variations in vertical structure of the surface such as layering or by the presence of multiple components comprising the surface in varying fractions, both of which are seen at the lander sites.

The issue of multiple components of materials is complex. Clearly, the Viking lander sites can be described by the presence of several components at each site, with a total of four different materials at both sites. Materials at each site have variable areal dimensions, thicknesses, and spatial distributions. The global remote-sensing data only allow for the determination of overall properties and do not allow the abundance of as many components as this to be determined. The relative abundances of patches of each component, as well as the size of each patch, cannot be determined from the presently available data at a spatial scale finer than approximately 100 km. Higher resolution information, from Mars Observer for example, would provide more-detailed results.

3.3.1 Thermal Model[8]

On the basis of observations made by the Viking Orbiter IRTM instruments, Kieffer et al., 1977, have developed a model of surface temperatures on Mars. The objective of this model is to account for the best-understood and largest terms in the heat equation: the diurnal and annual variation of insolation and the conduction into the ground. The thermal model is intentionally simple and does not include a variety of geophysical processes which certainly occur but whose quantitative behaviors are not well known.

The thermal model assumes that surface physical properties are homogeneous with depth and are uniform over the planet. The atmospheric properties are taken to be constant, with no cloud formation of any kind at any time. A CO_2 polar cap forms, and the surface radiometric albedo is asumed to change discontinuously when any frost is present. The CO_2 condensation temperature is fixed at 149 K rather than following the predicted surface pressure variation. There is no latitudinal transport of heat. No slopes are included. The absorption of sunlight is Lambertian, an ideal blackbody surface emission is assumed, and no heat flows across the lower boundary.

Using this model, the annual variation of daily extreme and daily average temperatures is shown in figure 3-7. The range of surface temperatures is 150 to 290 K.

3.4 SPECIAL CASES[9]

Several special cases need to be considered when discussing the surface of Mars. Some of the cases may be important because they represent hazards during landing, or traverse vehicles may have difficulty negotiating them. Fortunately, the cases below that are hazardous generally represent uncommon situations.

3.4.1 Canyons and Valleys

Some martian canyons are huge by terrestrial standards, and both the canyons and the valleys can present severe problems for landers and for vehicles. The problems accrue from both slopes and the materials of the slopes. The severity of the problems are not always clear because of the natural variables involved.

A profile of a landslide in Ius Chasma illustrates the some of the problems with canyons and valleys; see figure 3-8. Relief from the chasma floor to its rim is about 6.5 km. Slopes on the landslide of the chasma floor are generally moderate, but, locally, they are as large as 22° at a scale length of 2 km. There will be slopes larger than on the chasma floor at scale lengths appropriate to landers and vehicles. The relief of the chasma wall is about 3.7 km and the mean slope is 29°. Locally, the slopes exceed 32° and inspection of the images suggest that there are local outcrops of rock with slopes that may exceed 45°.

Some of the slopes are probably formed of talus or scree at or near the angle of repose. The grain sizes of the rocks or materials in the talus depend on the condition of the source rocks. The sizes could be uniformly fist-size (or smaller) or there could be a spectrum of sizes that includes large blocks. Whatever the size of the materials in the talus or scree slopes, they may be difficult or impossible to negotiate. This is particularly true when the slopes are near or at the angle of repose of the materials, and these can range from 30° to 45° depending on the shapes and sizes of the fragments in the talus.

3.4.2 Blocky Craters and Crater Blockfields

Fresh, blocky impact-craters can be very rough. Their mean slopes, which arise from blocks in their ejecta, may be as large as 25°. Similar things can be expected for local block fields around impact craters. Slope angles of the interior walls of impact craters may also be large and may exceed 40°.

3.4.3 Sand Dunes

Based on terrestrial experience, mean slopes of sand dune fields may be taken as 6.7° (Viking Project Office, 1974). Locally, leeward slopes of the dunes are 30° to 35° and at or near the angle of repose of cohesionless sand.

3.4.4 Lava Flows

Lava flow surfaces can be smooth to extremely rough, and weak to strong. Each lava flow surface must be judged on an individual basis. Pahoehoe flows are generally relatively smooth, but those of a'a and blocky flows can be as rough, or rougher than blocky craters. Rock and block surfaces of a'a and blocky flows are commonly jagged and sharp. In general, the materials of lava flows are strong, but the shelly and slabby pahoehoe flows are composed of voids surrounded by thin shells and slabs which collapse when loaded.

3.4.5 Polar Regions

The results from the Viking Orbiter Bistatic Radar Experiment indicate that variations of slopes or roughnesses in the north polar region are comparable to those observed near the equator (Simpson and Tyler, 1981). Interpretation of the dielectric properties of the north polar cap are uncertain, but dusts, ices, and snow may occur at the surface.

---

[8] The materials of section 3.3.1 are excerpted from "Thermal and Albedo Mapping of Mars During the Viking Primary Mission," by H.H. Kiefer, T.Z. Martin, A.R. Peterfruend, B.M. Jakosky, E.D. Miner, and F.D. Palluconi, 1977.

[9] The materials of section 3.4 are excerpted from "Preliminary Mars Surface Models," by Henry J. Moore, 1988, unpublished.

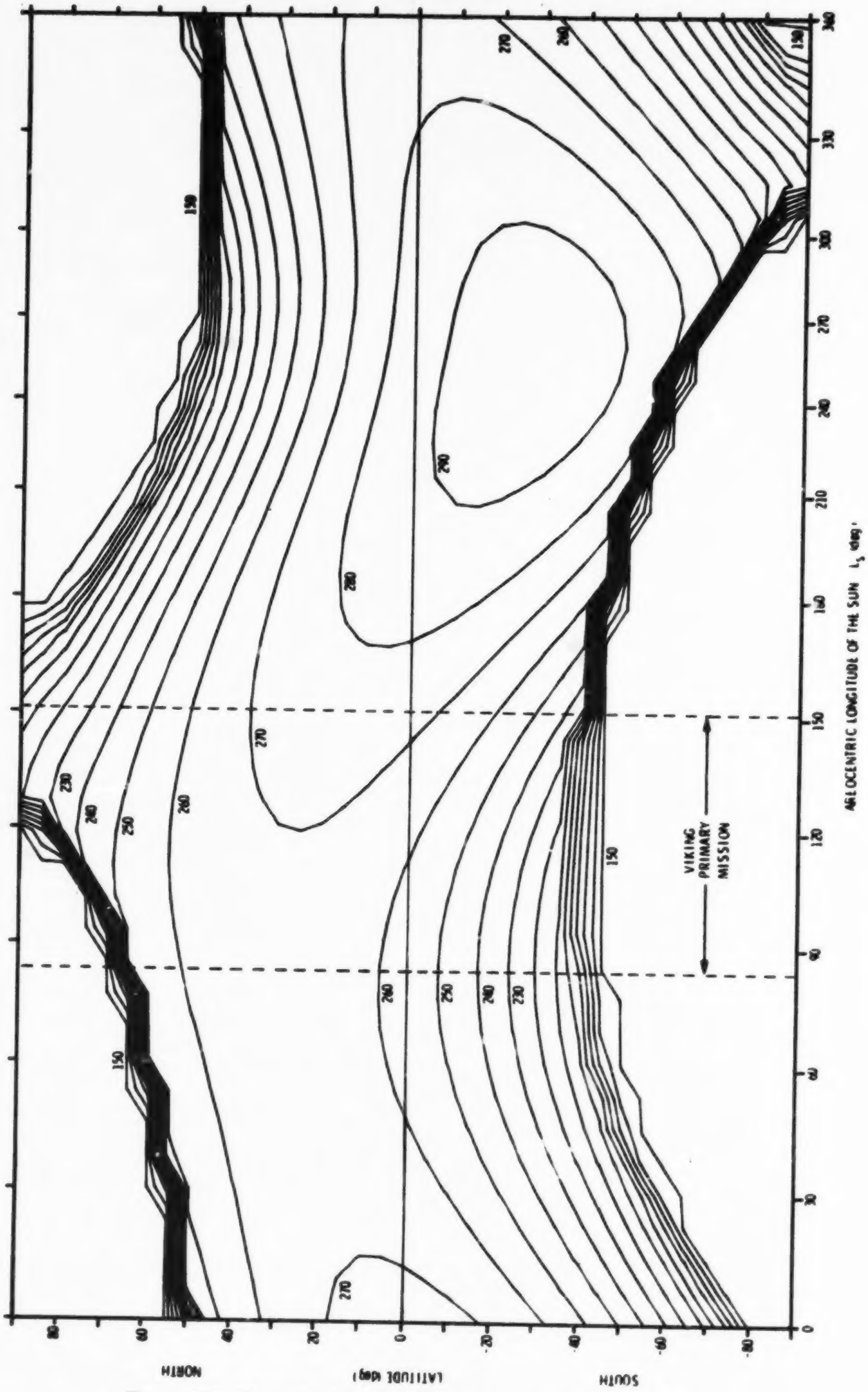

Figure 3-7.- Diurnal surface temperature mean and extremes for the primary Viking thermal model (Kieffer et al., 1977).

(a) Maximum temperatures.

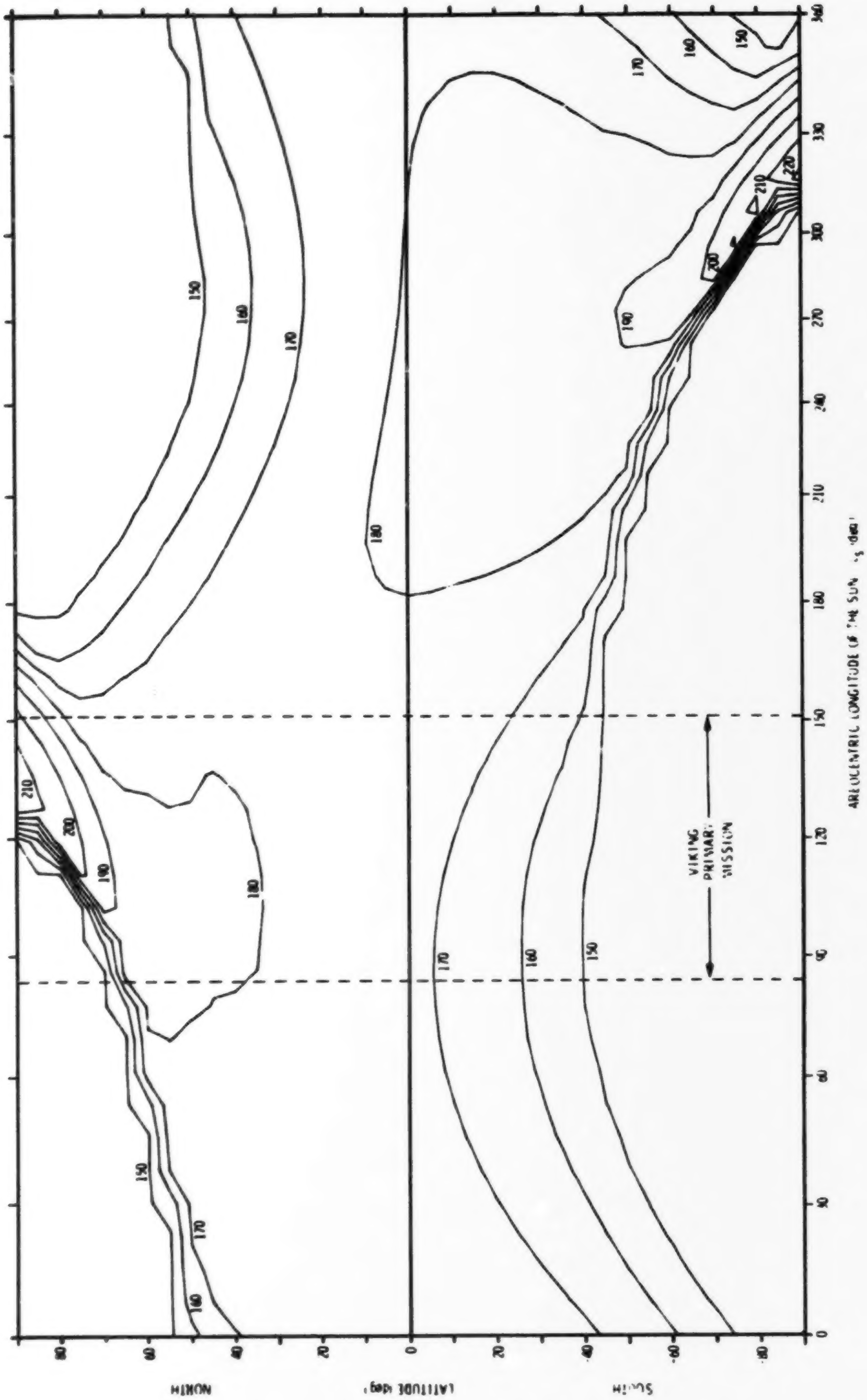

Figure 3-7.- Diurnal surface temperature mean and extremes for the primary Viking thermal model (Kieffer et al., 1977).

(b) Mininum temperatures.

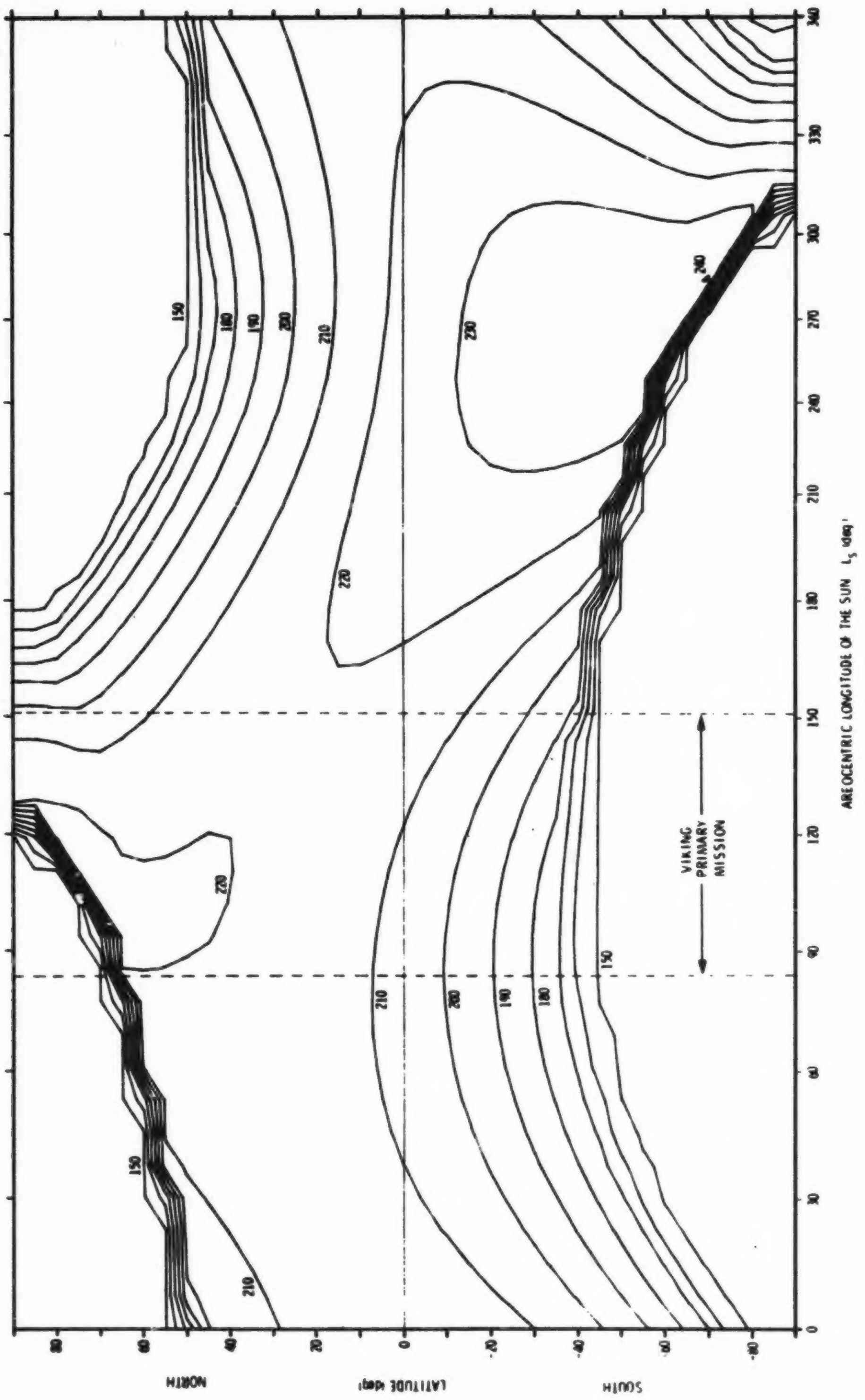

Figure 3-7.- Diurnal surface temperature mean and extremes for the primary Viking thermal model (Kieffer et al., 1977).

(c) Mean temperatures.

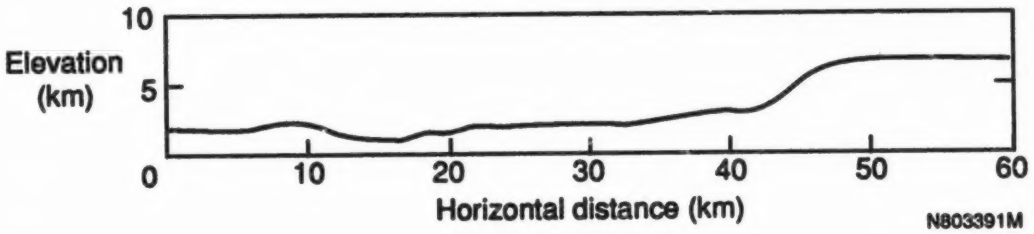

Figure 3-8.- Profile of Ius Chasm; (Moore, 1988).

3.5. REFERENCES

Adams, J. B.; Smith, M. O.; and Johnson, P. E.; 1986: Spectral Mixture Modeling: A New Analysis of Rock and Soil Typesat the Viking Lander 1 Site. J. Geophys. Res., vol. 91, pp. 8098-8112.

Arvidson, R.E.; Guinness, E.A.; and Lee, S.; 1979: Differential Aeolian Redistribution Rates on Mars. Nature, vol. 278, pp. 533-535.

Arvidson, R. E.; Guinness, E. A.; Moore, H. J.; Tillman, J.; and Wall, S. D.; 1983: Three Mars Years: Mutch Memorial Station (Viking Lander 1) Imaging Observations. Science, vol. 222, pp. 463-468.

Baird, A.K.; Castro, A.J.; Clark, B.C.; Toulmin III, P.; Rose, Jr., H.; Keil, K.; and Gooding, J.L.; 1977: The Viking X Ray Fluorescence Experiment: Sampling Strategies and Laboratory Simulations. J. Geophys. Res., vol. 82, pp. 4595-4624.

Ballou, E. V.; Wood, P. C.; Wydeven, T.; Lehwalt, M. E.; and Mack, R. E.; 1978: Chemical Interpretation of Viking Lander 1 Life Detection Experiment. Nature, vol. 271, pp. 644-645.

Banin, A.; and Rishpon, J.; 1979: Smectite Clays in Mars Soil: Evidence for their Presence and Role in Viking Biology Experimental Results. J. Molecular Evolution, vol. 14, pp. 133-152.

Banin, A.; and Margulies, L.; 1983: Simulation of Viking Biology Experiments Suggests Smectites not Palagonite, as Martian Soil Analogs. Nature, vol. 305, pp. 523-526

Biemann, K.; Oro, J.; Toulmin III, P.; Orgel, L.E.; Nier, A.O.; Anderson, D.M.; Simmonds, P.G.; Flory, D.; Diaz, A.V.; Rushneck, D.R.; Biller, J.E.; and LaFleur, A.L.; 1977: The Search for Organic Substances and Inorganic Volatile Compounds in the Surface of Mars. J. Geophys. Res., vol. 82, pp. 4641-4658.

Biemann, K.; 1979: The Implications and Limitations of the Findings of the Viking Organic Analysis Experiment. J. Mole. Evol, vol. 14, pp. 65-70

Binder, A. B.; Arvidson, R. E.; Guinness, E. A.; Jones, K. L.; Morris, E. C.; Mutch, T. A.; Pieri, D. C.; and Sagan, C.; 1977: The Geology of the Viking Lander 1 Site. J. Geophys. Res., vol. 82, pp. 4439-4451.

Brown, J. H.; Mitchell, S. R.; and Weissman, M.; 1960: Energy-Size Reduction Relationship for the Grinding of Quartz. Transactions of the American Institute of Mining Engineers, vol. 217, pp. 203-206.

Campbell, M.H.; and Ulrichs, J.; 1969: Electrical Properties of Rcks and Their Significance for Lunar Radar Observations. J. Geophys Res., vol. 74, pp. 5867-7881.

Christensen, P. R.; 1982: Martian Dust Mantling and Surface Composition: Interpretation of Thermophysical Properties. J. Geophys. Res., vol. 87, pp. 9985-9998.

Christensen, P.R.; 1986a: Regional Dust Deposits on Mars: Physical Properties, Age, and History. J. Geophys. Res., 91, pp. 3533-3545.

Christensen, P.R.; 1986b: The Spatial Distribution of Rocks on Mars. Icarus, vol. 68, pp. 217-238.

Chun, S.F.S.; Pang, K.D.; Cutts, J.A.; Ajello, J.M.; 1978: Photocatalytic Oxidation of Organic Compounds on Mars. Nature, vol. 274, pp. 875-876.

Clark III, B. C.; Baird, A. K.; Rose, Jr., H. J.; Toulmin III, Priestley; Christian, R. P.; Kelliher, W. C.; Castro, A. J.; Rowe, C. D.; Keil, K.; and Huss, G. R.; 1977: The Viking X-ray Fluorescence Experiment: Analytical Methods and Early Results. J. Geophys. Res., vol. 82, pp. 4577-4594.

Clark, B. C.; Baird, A. K.; Weldon, R. J.; Tsusaki, D. M.; Schnabel, L.; and Candelaria, M. P.; 1982: Chemical Composition of Martian Fines. J. Geophys. Res., vol. 87, pp. 10,059-10,067.

Dale-Bannister, M. A.; Arvidson, R. E.; and Moore, H. J.; 1988: On the Presence of Unweathered Lithic Fragments in Viking Lander 1 Soil. Lunar and Planetary Science, vol. XIX, pp. 239-240.

Downs, G.S.; Goldstein, R.M.; Green, R.R.; Morris, G.A.; and Reichley, E.; 1973: Martian Topography and Surface Properties as Seen by Radar: The 1971 Opposition. Icarus, vol. 18, pp. 8-21.

Downs, G. S.; Reichley, P. E.; and Green, R. R.; 1975: Radar Measurements of Martian Topography and Surface Properties: The 1971 and 1973 Oppositions. Icarus, vol. 26, pp. 273-312.

Fanale, F. P.; Nash, D. R.; and Cannon, W. A.; 1971: Lunar Fines and Terrestrial Rock Powders: Relative Surface Areas and Heats of Adsorption. J. Geophys. Res., vol. 76, pp. 6459-6461.

Fanale, F.P.; Salvail, J.R.; Banerdt, W.B.; and Saunders, R.S.; 1982: The Regolith-Atmosphere-Cap System and Climate Change. Icarus, vol. 50, pp. 381-407.

Fountain, J. A.; and West, E. A.; **1970**: Thermal Conductivity of Particulate Basalt as a Function of Density in Simulated Lunar and Martian Environments. J. Geophys. Res., vol. 75, pp. 4063-4069.

Garvin, J.B.; Mouginis-Mark, P.J.; and Head, J.W.; **1981**: Characterization of Rock Population on Planetary Surfaces: Techniques and a Preliminary Analysis of Mars and Venus, Moon and Planets. Vol. 24, pp. 355-387.

Guinness, E. A.; Arvidson, R. E.; Dale-Bannister, M. A.; Singer, R. B.; and Bruckenthal, E. A.; **1987**: On the Spectral Reflecrance Properties of Materials Exposed at the Viking Landing Sites. J. Geophys. Res., vol. 78, pp. 4291-4312.

Harmon, J. K.; and Ostro, S. J.; **1985**: Mars: Dual-Polarization Radar Observations with Extended Coverage. Icarus, vol. 62, pp. 110-128.

Harmon, J.K.; Ostro, S.J.; **1985**: Dual-Polarization Radar Observations of Mars: Tharsis and Environs. Icarus, vol. 52, pp. 171-187.

Hoekstra, P.; and Delaney, A.; **1974**: Dielectric Properties of Soils at UHF and Microwave Frequencies. J. Geophys. Res., vol. 79, pp. 1699-1708.

Horai, Ki-iti; **1979**: Loose and Compacted Soils: Two Basic Units Composing the Martian Surface. Lunar aud Planetary Science X, pp. 564-566.

Horowitz, N.H.; **1977**: The Search for Life on Mars. Scientific American, November 1977, pp. 52-61.

Horowitz, N.H.; and Hobby, G.L.; **1977**:. Viking on Mars: The Carbon Assimilation Experiments. J. Geophys. Res., vol. 82, pp. 4659-4662.

Huguenin, R.L.; Miller, K.J.; and Harwood, W.S.; **1979**: Frost-Weathering on Mars: Experimental Evidence for Peroxide Formation. J. Mole. Evol., vol. 14, pp. 103-132.

Hunten, D.; **1979**: Possible Oxidant Sources in the Atmosphere and Surface of Mars. J. Mol. Evol., vol. 14, pp. 57-64.

Hunten, D.M.; **1987**: Oxidants in the Martian Atmosphere and Soil. In Study of Martian Surface and Atmospheric Effects on Mars Rover, Lander and Ballons. JPL publication D-4657, pp. 4.7-4.13.

Hutton, R. E.; Moore, H. J.; Scott, R. F.; Shorthill, R. W.; and Spitzer, C. R.; **1980**: Surface Erosion Caused on Mars from the Viking Descent Engine Plume. The Moon and Planets, vol. 23, pp. 293-305.

Jakosky, B. M.; **1986**: On the Thermal Properties of Martian Fines. Icarus, vol. 66, pp. 117-124.

Jakosky, B. M.; and Christensen, P. R.; **1986a**: Are the Viking Landing Site Representative of the Surface of Mars? Icarus, vol. 66, pp. 125-133.

Jakosky, B.M.; and Christensen, P.R.; **1986b**: Global Duricrust on Mars: Analysis of Remote-Sensing Data. J. Geophys., Res., vol. 91, pp. 3547-3559.

Jakosky, B.M.; and Muhleman, D. O.; **1981**: A Comparison of Thermal and Radar Characteristics of Mars. Icarus, vol. 45, pp. 25-38.

Kieffer, H. H.; **1976**: Soil and Surface Temperatures at the Viking Landing Sites. Science, vol. 194, pp. 1344-1346.

Kieffer, H. H.; Chase, Jr., S. C.; Miner, E.; Munch, G.; and Neugebauer, G.; **1973**: Preliminary Report on Infrared Radiometric Measurements from the Mariner 9 Spacecraft. J. Geophys. Res., vol. 78, pp. 4291-4312.

Kieffer, H. H.; Martin, T. Z.; Peterfreund, A. R.; Jakosky, B. M.; Miner, E. D.; and Palluconi, F. D.; **1977**: Thermal and Albedo Mapping of Mars During the Viking Primary Mission. J. Geophys. Res., vol. 82, pp. 4249-4291.

Klein, H.P.; **1978**: The Viking biological experiments on Mars. Icarus, vol. 34, pp. 666- 674.

Klein, H.P.; **1979**: The Viking Mission and the Search for Life on Mars. Rev. Geophys. and Space Phys., vol. 17, pp. 1655-1662.

Levin, G.V.; and Straat, P.A.; **1977**: Recent Results from the Viking Labeled Release Experiment on Mars. J. Geophys. Res., vol. 82, pp. 4663-4667.

Mazur, P.; Barghoorn, E.S.; Halvorson, H.O.; Jukes, T.H.; Kaplan, I.R.; and Margulis, L.; **1978**: Biological Implications of the Viking Mission to Mars. Space Sci. Rev., vol. 22, pp. 3-34.

Mitchell, J. K.; Houstou, W. N.; Scott, R. F.; Costes, N. C.; Carrier III, W. D.; and Carrier III, L.; Bromwell, G.; **1972**: Mechanical Properties of Lunar Soil: Density, Porosity, Cohesion, and Angle of Internal Friction. Proc. Third Lunar Sci. Conf., Suppl. 3, Geochimica et Cosmochimica Acta., vol. 3, pp. 3235-3253.

Mooney, R. W.; Keenan, A. G.; and Wood, L. A.; **1952**: Adsorption of Water Vapor by Montmorillonite. I. Heat of Desorption and Application of BET Theory. J. Amer. Chem. Soc., vol. 74, pp. 1367-1371.

Moore, H.J.; and Jakosky, B.M.; **1988**: Viking Landing Sites, Remote Sensing Observations, and Physical Properties of Martian Surface Materials. Submitted to Icarus.

Moore, H.J.; 1988: Preliminary Mars Surface Models. Unpublished.

Moore, H. J.; 1985: The Martian Dust Storm of Sol 1742. Proc. Lunar Planet. Science Conf., 16th Supplement, J. Geophys. Res., vol. 90, D163-D174.

Moore, H. J.; 1986: Miniature Slope Failures, Mutch Memorial Station. In MECA Workshop on Dust in Mars, Lunar and Planetary Institute, technical report no. 86-09, pp. 53-55.

Moore, H. J.; Hutton, R. E.; Scott, R. F.; Spitzer, C. R.; and Shorthill, R. W.; 1977: Surface Materials of the Viking Landing Sites. J. Geophys. Res., vol. 82, pp. 4497-4523.

Moore, H. J.; Spitzer, C. R.; Bradford, K. Z.; Cates, P. M.; Hutton, R. E.; and Shorthill, R. W.; 1979: Sample Fields of the Viking Landers Physical Properties, and Aeolian Processes. J. Geophys. Res., vol. 82, pp. 8365-8377.

Moore, H. J.; Clow, G. D.; and Hutton, R. E.; 1982: A Summary of Viking Sample-Trench Analyses for Angles of Internal Friction and Cohesions. J. Geophys. Res., vol. 87, pp. 10,043-10,050.

Moore, H. J.; Hutton, R. E.; Clow, G. D.; and Spitzer, C. R.; 1987: Physical Properties of the Surface Materials of the Viking Landing Sites on Mars. U.S. Geol. Survey Prof. Paper 1389, 2 plates, p. 222.

Morris, E. C.; and Jones, K. L.; 1980: Viking 1 Lander on the Surface of Mars: Revised Location. Icarus, vol. 44, pp. 217-222.

Mutch, T. A.; Arvidson, R. E.; Binder, A. B.; Huck, F. 0.; Levinthal, E. C.; Liebes, Jr.,S.; Morris, E. C.; Nummedahl, D.; Pollack, J. B.; and Sagan, C.; 1976a: Fine Particles on Mars: Observation with the Viking 1 Lander Cameras. Science , vol. 194, pp. 87-91.

Mutch, T. A.; Binder, A. B.; Huck, F. 0.; Levinthal, E. C.; Liebes, Jr., S.; Morris, E. C.; W. R. Patterson, J.; Pollack, B.; Sagan, C. and Taylor, G. R.; 1976b: The Surface of Mars: The View from the Viking 1 Lander. Science, vol. 193, pp. 791-801.

Mutch, T. A.; Grenander, S. V.; Jones, K. L.; Patterson, W. R.; Arvidson, R. E.; Guinness, E. A.; Avrin, P.; Carlston, C. E.; Binder, A. B.; Sagan, C.; Dunham,E. W.; Fox, P. L.; Pieri, D. C.; Huck, F. 0.; Rowland, C. W.; Taylor, G. R.; Wall, S. D.; Kahn, R.; Levinthal, E.C.; Liebes, Jr., S.; Tucker, R. B.; Morris, E. C.; Pollack, J. B.; Saunders, R. S.; and Wolf, M. R.; 1976c: The Surface of Mars: The View from the Viking 2 Lander. Science, vol. 194, pp.1277-1283.

Mutch, T. A.; Arvidson, R. E.; Binder, A. B.; Guinness, E. A.; and Morris, E.C.; 1977: The Geology of the Viking Lander 2 Site. J. Geophys. Res., vol. 82, pp. 4452-4467.

Nussinov, M.D.; Chernyak, Y.B.; and Ettinger, J.L. ; 1978: Model of the Fine-Grain Component of Martian Soil Based on Viking Lander Data. Nature, vol. 274, pp. 859-861.

Oro, J.; and Holzer, G.; 1979: The Photolytic Degradation and Oxidation of Organic Compounds under Simulated Martian Conditions. J. Mol. Evol., vol. 14, pp. 153-160.

Oyama, V. I.; and Berdahl, B. J.; 1977: The Viking Gas Exchange Experiment Results from Chryse and Utopia Surface Samples. J. Geophys. Res., vol. 82, pp. 4669-4676.

Oyama, V.I.; and Berdahl, B.J.; 1979: A Model of Martian Surface Chemistry. J. Mol. Evol., vol. 14, pp. 199-210.

Palluconi, F. D.; and Kieffer, H. H.; 1981: Thermal Inertia Mapping of Mars from 60° S to 60° N. Icarus, vol. 45, pp. 415-426.

Pollack, J. B.; Colburn, D. S.; Flasar, F. M.; Kahn, R.; Carlston, C. E.; and Pidek, D.; 1979: Properties and Effects of Dust Particles Suspended in the Martian Atmosphere. J. Geophys. Res., vol. 84, pp. 2929-2945.

Ponnamperuma, C.; Shimoyama, A; Yamada, M.; Hobo, T.; and Pal, R.; 1977: Possible Surface Reactions on Mars: Implications for Viking Biology Results. Science, vol. 197, pp. 455-457.

Romaine, G.L.; Reisert, T.D.; and Gliozzi, J.; 1973: Site Alteration Effects from Rocket Exhaust Impingement During a Simulated Viking Mars Landing. Part 1 of 2, Nozzle Development and Physical Alteration. U.S. National Aeronautics and Space Administration (NASA) contractor report 2252, 155 pages. Settle, M.; 1979: Formation and Deposition of Volcanic Sulfate Aeriosols on Mars J. Geophys. Res., vol. 84, pp. 8343-8354.

Sharp, R. P.; and Malin, M. C.; 1984: Surface Geology from Viking Landers on Mars: A Second Look. Geol. Soc. Am. Bull., vol. 95, pp. 1389-1412.

Simpson, R.A.; and Tyler, G.L.; 1981: Viking Bistatic Radar Experiment: Summary of First-Order Results Emphasizing North Polar Data. Icarus, vol. 46, pp. 361-389.

Simpson, R. A.; Tyler, G. L.; and Campbell, D. B.; 1978: Arecibo Radar Observations of Martian Surface Characteristics in the Northern Hemisphere. Icarus, vol. 36, pp. 153-173.

Tang, C. H.; Boak III, T. I. S.; and Grossi, M. D.; 1977: Bistatic Radar Measurements of Electrical Properties of the Martian Surface. J. Geophys. Res., vol. 82, pp. 4305-4315.

Toon, O.B.; Pollack, J.B.; and Sagan, C.; 1977: Physical Properties of Particles Comprising the Martian Dust Storm, 1971-1972. Icarus, vol. 30, pp. 663-696.

Toulmin III, P.; Baird, A. K.; Clark, B. C.; Keil, K.; Rose, Jr., H. J.; Christian, R. P.; Evans, P. H.; and Kelliher, W. C.; 1977: Geochemical and Mineralogical Interpretation of the Viking Inorganic Chemical Results. J. Geophys. Res., vol. 82, pp. 4625-4634.

Tyler, G. L.; Campbell, D. B.; Downs, G. S.; Green, R. R.; and Moore, H. H.; 1976: Radar Characteristics of Viking 1 Landing Sites. Science, vol. 193, pp. 812-815.

Von Hippel, A. R.; 1954: V - Tables of dielectric materials. In Von Hippel, A. R., ed., Dielectric Materials and Applications. New York, John Wiley and Sons, Inc., p. 430.

Wechsler, A. E.; and Glaser, P. E.; 1965: Pressure Effects on Postulated Lunar Materials. Icarus, vol. 4, pp. 335-352.

Wechsler, A.E.; Glaser, P.E.; and Fountain, J.A.; 1972: Thermal Properties of Granulated Materials. Astronautics and Aeronautics, vol. 28, pp. 215-241.

Zimbelman, J. R.; and Kieffer, H. H.; 1979: Thermal Mapping of the Northern Equatorial and Temperate Latitudes of Mars. J. Geophys. Res., vol. 84, pp. 8239-8251.

Zurek, R. W.; 1987: Topographically and Thermally Generated Planetary Waves on Mars. Paper presented at the Internar. Union Geodesy-Geophysics Meeting, Vancouver, Canada, Aug.

ORIGINAL PAGE
COLOR PHOTOGRAPH

Artwork by Ron Miller (from "Pioneering the Space Frontier: The Report of the National Commission on Space,"1986)

Mars Astrodynamic Model[1]

4.1 INTRODUCTION

The astrodynamic data described herein is intended to be a source of reference for Mars. Definitions, models, and values of astrophysical quantities are presented which are required to perform: (1) flight path design, (2) navigation design, and (3) science observation design.

A detailed Mars model is emphasized. Astronomical constants, time scales, and reference coordinate frames are presented. The Earth model is given only to the extent necessary. Gravitational constants of other planets and general astrodynamic constants are included.

4.2 GENERAL CONSTANTS[2]

4.2.1 Time Systems

Ephemeris time (ET) is the mathematically uniform time scale used as the independent variable in the gravitational theories of the motion of the Sun, the Moon, and the planets and in the argument for the ephemerides of these bodies. For navigation and trajectory work, ephemeris time is the reference time scale used.

For civil time keeping, Coordinated Universal Time (UTC) is referenced. The UTC is the time scale actually used in most parts of the world, and it is obtained from various radio time services. The UTC is an approximation of universal time (UT), but it is actually measured with respect to atomic time. The rate of UTC is therefore constant, but periodic step adjustments are made by the Bureau International de l'Heure to maintain an approximation to UT. Transformations between ET and UTC are defined by time-varying offsets that are determined from coordinated measurements of the astronomical and atomic time scales. As of January 1, 1986, the DET (i.e., ET-UTC) is measured at 55.185 sec (refer to Supplement to the Astronomical Almanac, 1984). The value of DET has been increasing steadily over the 20th century, but it cannot be predicted accurately.

4.2.2 Standard Reference Coordinate Systems

The fundamental inertial coordinate systems used for representing astrodynamic quantities in this document are EME50 and EMO50. These systems are defined by the mean orbit and the rotation pole orientations of Earth on the standard epoch. The standard epoch used to establish inertial reference systems for all cataloging of astrodynamic quantities until 1984 has been the beginning of the Besselian year, which is 1950.0 ET. This date is also designated B1950, which corresponds to December 31, 1949 at 22 hr, 9 min, 38.076827797 sec, and this is equal to Julian Ephemeris date (JED) 2433282.423357370692. (The 0 Julian date is Greenwich noon on January 1, 4713 B.C.)[3].

4.2.2.1 Earth Mean Equator and Equinox of 1950.0 (EME50)

The EME50 system is defined by the z-axis in the direction of the mean rotation pole of Earth on the standard epoch. The x-axis is in the direction of the vernal equinox defined by the ascending intersection of the mean orbit plane on the mean equatorial plane. The y-axis completes the right-handed orthogonal system.

4.2.2.2 Earth Mean Ecliptic and Equinox of 1950.0 (EMO50)

The z-axis of the EMO50 system is defined by the mean orbit pole of Earth on the standard epoch. The x-axis is equal to the vernal equinox and the y-axis completes the right-handed orthogonal system.

The EMO50 system is obtained from the EME50 system by a single rotation about the x-axis by an angle equal to the mean obliquity at the B1950 epoch; specifically,

$$\varepsilon_{50} = 23.4457888889 \text{ deg}$$

4.2.3 Table of General Constants

The fundamental constants which contribute to the definitions of gravitational forces are the definitive Gaussian constants, the 1-AU light time, and the mass ratios of planets to the Sun. These fundamental constants and the derived constants (GM's) are summarized in table 4-1. These are Jet Propulsion Laboratory (JPL) adopted numbers and are consistent with the IAU (1976) values except for small adjustments made to fit observations (Lieske, 1985). The inherent uncertainties in the knowledge of the mass ratios result in only a few significant digits in the GM values (significant digits are underlined in the table), however, the DE118 ephemerides created at JPL use the full 18-digit numbers given in the table.

---

[1] The materials of part 4 are excerpted from the document: "Mars Observer: Planetary Constants and Models — Preliminary," by C.L. Yen and W.H. Blume, JPL Document D-3444, Jet Propulsion Laboratory, July 1986. Where appropriate, updates and corrections have been incorporated into the present document.

[2] The International Astronomical Union (IAU) (1976) System of Astronomical Constants (ref. 44-1) was adopted by the General Assembly of the IAU at Grenoble (ref. 44-2). Additional resolutions concerning time scales and the astronomical reference systems were adopted by the IAU in 1979 at Montreal and in 1982 at Patras. A complete list of these resolutions with constants, formulae, and explanatory notes is available in the Supplement to the Astronomical Almanac for 1984 (ref. 44-3). The sources just listed provide the basic constants contained in this document. However, principal ephemerides of planets are based on the computations made at JPL, and they include slight modifications to the IAU (1976) System of Astronomical Constants in order to ensure a best fit of the ephemerides to the observational data.

[3] Beginning in 1984, the IAU (International Astronomical Union) has introduced a new system of astronomical constants, time scales, and reference coordinate frames into the Astronomical Almanac. This new system, termed J2000, uses a standard epoch of January 15, 2000 ET, corresponding to the Julian date JED 2451545.0.

Solar constant $W_{(Sun)}$ (i.e., the flux of total radiation received at 1 AU) given is consistent with the value used by the JPL DPTRAJ code (Georgevic, 1971).

Other planetary constants of Earth and Mars are also included in table 4-1. Earth pole and prime meridian orientations depicted are based on the model of Sturms, 1971. Recent IAU recommendations (Davies et al., 1986) are adopted for the Mars rotational elements (see section 4.4.2.3).

4.2.4 Planetary Ephemerides

Two sources of planetary ephemerides are available. For high precision trajectory propagation and navigational analyses, JPL Developmental Ephemerides (DE) can be used. For medium accuracy mission design analyses, simple conic orbital elements might be used. Both of these two types of data are discussed here.

4.2.4.1 Precision Planetary Ephemerides

Each numbered version of the JPL DE is a computer file of data for computing the position of the Sun and of the barycenters of the nine planetary systems relative to the solar system barycenter. (A geocentric lunar ephemeris (LE) is also included.) The file gives Chebyshev polynomial coefficients for evaluating the position of each body over a specified period of time (Standish, 1982).

The ephemeris coordinates given for Mars are of the barycenter of the martian system (Mars plus Phobos and Deimos).If positions of the center of mass of Mars or of the satellites are required, a compatible satellite ephemeris must be used (see section 4.5.2). Because of the small size of the satellites, the barycenter to center-of-mass correction is never greater than .25 m, and can usually be ignored.

4.2.4.2 Analytical Ephemerides of Mars and Earth

Analytical expressions for the mean orbital elements of the planets can be used for efficient and moderately accurate ephemeris computations. A particular model, using polynomial expressions for the mean orbital elements, was defined by Sturms, 1971. These expressions are used in JPL navigation software to define the mean orbit plane of the planet. The heliocentric orbit elements are referenced to the Earth mean orbit and equinox of the 1950.0 (EM050) coordinate system. Mean orbital elements of Earth and Mars as a function of time are listed in table 4-2.

4.3 EARTH MODEL

4.3.1 Earth Gravitational Field

Zonal harmonic coefficients up to J_4 of Earth gravitational field:

J_2	0.00108263
J_3	-0.254E-5
J_4	-0.161E-5

4.3.2 Earth Topographic Sites

4.3.2.1 Launch Site

The coordinates for the launch site at the Kennedy Space Center are:

latitude	28.45°
longitude	279.4°

4.3.2.2 Deep Space Network Station Sites

Geocentric spherical coordinates of the Deep Space Network station sites are listed below in table 4-3. (These are the calculated values and not verified by actual measurements.)

4.4 MARS MODEL

4.4.1 Shape

The surface figure of Mars is more irregular than that of the Earth, where a simple oblate spheroid model provides the reference surface (an excellent approximation to mean sea level). For Mars, two different reference surfaces are used for different purposes.

4.4.1.1 Equatorial Radius

The standard for measuring radial distances from Mars is the equatorial radius defined by the IAU in 1976 (Seidelmann, 1977).

$$R_M = 3397.2 \pm 1 \text{ km}$$

The surface of Mars deviates substantially from a circle at the equator and this represents an average value. The equatorial radius should be used for defining distances from the center of mass of Mars in "martian radii". Also, for the near-circular mapping and quarantine orbits, the term "orbit altitude" will be defined as the difference between the mean semi-major axis, $\bar{a}$ of the orbit and the equatorial radius of Mars.

$$\text{Orbit Altitude} = \bar{a} - R_M$$

Symbol	Value	Units	Comments
k	0.01720209895		Gaussian constant
c	299792.458 ± 0.0012	km/s	Velocity of light
t	499.0047837 ± 0.000002	sec	1-AU light time
AU	149,597,870.66 ± 2	km	AU = c * t
$W_{(sun)}$	1348.	w/m**2	Solar flux at 1 AU
GMS	.132712439935484068D12	km**3/sec**2	GMS=AU**3*k**2/(86400)**2 GM of Sun
GM(1)†	.220320804727213072D5		Mercury
GM(2)	.324858765616871651D6		Venus
GM(3)	.398600448073446286D6		Earth
GM(4)	.428282865887688960D5		Mars
GM(5)	.126712597081794544D9		Jupiter
GM(6)	.379395197088299637D8		Saturn
GM(7)	.578015853359771834D7		Uranus
GM(8)	.687130777147952364D7		Neptune
GM(9)	.102086492070628559D4		Pluto
GMM	.490279914059472027D4		Moon
GMB	.403503247214041006D6		Earth-Moon system
† GM is for planetary system including its satellites.			
RPL(3)	6378.14 ± 0.005	km	Equatorial radius of Earth
RPL(4)	3397.2 ± 1	km	Equatorial radius of Mars
f_E	.00335281 ± 0.00000002		Earth flattening
f_M	.0051865		Mars flattening
RS(3)	2.5D6	km	Sphere of influence for Earth
RS(4)	2.0D6	km	Sphere of influence for Mars

Planet pole orientations: Declination and right ascension in EME5O system.

d_E = 89.9999988317 - 0.5567500297*T + 0.0001185607*T**2 (deg) ←Earth

a_E = -0.0000013435 - 0.6402780091*T - 0.0000839481*T**2 ←Earth

d_M = 52.711 - 0 061*T ←Mars

a_M = 317.342 - 0.108*T (deg) ←Mars

where T = (JED - 2433282.5)/36525.

Prime meridians: Hour angles of the mean equinoxes

V_E = 100.0755426042 + 360.98564734584*(d - DUT††/86400) (deg) ←Earth

V_M = 148.595 + 350. 89198566343*d (deg) ←Mars

where d = (JED - 2433282.5) = days from Jan. 1.0, 1950.

†† DUT = ET - UT (see section 4.2.2); tentatively use the value for DET.

Rot(4) 350.891985 ± . 000007		deg/day	Mars rotation rate

TABLE 4-1.- Table of general constants

4.4.1.2 Reference Mapping Surface

The reference mapping surface for Mars has been defined by the U.S. Geological Survey (USGS) in preparing the existing maps of Mars. It should be used to locate surface features on Mars and to define the nadir direction. The nadir direction is the fundamental pointing reference for science observations. The reference surface is an oblate spheroid centered at the center of mass of the planet. The equatorial and polar radii of the spheroid are defined as

r_e = 3393.4 km ←equatorial radius

r_p = 3375.7 km ←polar radius

This reference surface, also called the USGS mapping spheroid, is referenced to a particular pressure level in the atmosphere (6.1 mbar), and it has a smaller equatorial radius than the average of the solid surface.

Earth:			
a =	149597927. (km)		
e =	0.0167301085	- 0.000041926*T	- 0.000000126*T**2
i =		0.013076*T	- 0.00009*T**2 (deg)
Ω =	174.40956	- 0.24166*T	+ 0.00006*T**2 (deg)
ω=	287.67097	+ 0.56494*T	+ 0.00009*T**2 (deg)
M =	358.000682	+ 0.9856002628*d	- 0.000155*T**2
			+ 0.0000033333*T**3 (deg)
Mars:			
a=	227941040. (km)		
e =	0.09335891275	+ 0.000091987*T	- 0.000000077*T**2
i =	1.850-0.00821*T	- 0.00002*T**2 (deg)	
Ω=	49.17193-0.2947*T-	0.00065*T**2 (deg)	
ω=	285.96668	+ 0.73907*T	+ 0.00047*T**2 (deg)
M=	169.45872	+ 0.5240207716*d	+ 0.0001825972*T**2
			+ 0.0000011944*T**3 (deg)

Where:

d=ephemeris days from reference date (Jan. 1.0 1950.
ET = JED 2433282.5)
which differs from the B1950 epoch.
T= d/36525.

TABLE 4-2.- Analytic ephemerides of Earth and Mars

4.4.2 Orientations

4.4.2.1 Mean Orbit Pole

Computation of the mean orbit pole of Mars as a function of time is based on the analysis of Sturms,1971. The mean orbital inclination(i) and node(Ω), as described in section 4.2.4.2, provides the vector of the orbit pole.

4.4.2.2 Mean Rotation Pole

The IAU has defined the declination and right ascension of the pole as a linear function of time in the EME50 coordinate system (Davies et al., 1983) as follows:

$$\alpha_M = 317.342 - 0.108{*}T \quad \text{(deg)}$$

$$\delta_M = 52.711 - 0.061{*}T$$

where: $T = (\text{JED} - 2433282.5)/36525$ (Julian century from Jan. 1, 1950)

4.4.2.3 Prime Meridian

Station	Coordinates		
	Radius km	Latitude degrees	Longitude degrees
DSS15	6371.96	35.2403	243.1120
DSS45	6371.68	-35.2170	148.9788
DSS65	TBD		

TABLE 4-3.- Coordinates of deep space network sites

4.4.2.3.1 IAU specification of prime meridian.- The IAU defines prime meridian by specifying the angle W that is measured along the martian equator eastward from the ascending node of the martian equator on the EME50 equatorial plane to the point where the prime meridian crosses the planet's equator (see fig. 4-1). The value for W derived by Sweetser, 1988, from Davies et al., 1986, is:

$$W = 11.578 + 350.891983{*}d$$

where: d is the number of days measured from the standard epoch.

4.4.2.3.2 Hour angle of equinox specification of prime meridian.- The JPL mission software uses the hour angle of martian equinox, V_M, (see fig. 4-2) to specify the prime meridian. The IAU definition for the prime meridian may be converted to the JPL format (Blume, 1986a). The result is the following expression for the hour angle of equinox V_M (also given in table 4-1). The value for V_M derived by Sweetser, 1988, from Davies et al., 1986, is:

$$V_M = 148.5948 + 350.89198566343{*}d \quad \text{(deg)}$$

where: $d = (\text{JED} - 2433282.5)$

4.4.2.4 Rotation Rate

The rotation rate of Mars as measured with respect to the martian vernal equinox is (Michael, 1979):

$$\text{ROT} = 350.891985 \pm 0.000007 \text{ deg/day}$$

4.4.3 Gravitational Field

4.4.3.1 Gravitational Harmonics

The current knowledge of the gravity field is obtained mainly from the analysis of the Mariner 9 and Viking 1 and 2 radio tracking data. A variety of global gravity field models of order 6, 12, and 18 are published in the literature (Balmino et al., 1982; Christensen and Balmino, 1979; Christensen and Williams, 1978).[4]

4.4.3.2 Gravity Anomalies

Gravity anomalies (MASCONS) are known to exist on Mars and are considered to be important sources of perturbation for low altitude orbits. The current knowledge is summarized in table 4-4 (Sjogren, 1985). Note the large uncertainties associated with the anomalies in the high latitude regions. This is due to the fact that the previous orbiters were only able to probe those regions from high altitude orbits. At JPL, the disk model (Christensen and Williams, 1978) is used to account for the dynamic effects of the MASCONS.

4.4.4 Martian Time Systems

4.4.4.1 Martian Seasonal Time

The seasons of Mars are measured by the longitude of the Sun, L_s, with respect to the vernal equinox of the planet. The L_s is the planetocentric longitude of the Sun measured eastward in the orbital plane of Mars. The vernal equinox is defined by the instantaneous orbital and equatorial planes. This definition follows the one used in The Astronomical Almanac, 1986. The L_s differs slightly from the areocentric right ascension of the Sun. Figure 4-3 shows the definition of L_s.

Table 4-5 shows the beginning dates of the martian seasons for the time period 1995 through 2005.

4.4.4.2 Martian Solar Time

Two types of martian solar time, local true solar time and local mean solar time can be used to express the time of day at a point on the surface of Mars. Local true solar time (LTST) is measured relative to the true position of the Sun. The LTST of a point on the surface of Mars is defined by the difference in areocentric right ascension between that point and the true Sun, as shown in figure 4-4. The right ascension difference, measured eastward, is measured in degrees and converted to true solar hours, minutes, and seconds past local noon. The units of this equivalent clock time are not constant, but are defined by analogy with the Earth on the basis of 24 "true-solar-hours" per true solar day. The true solar day for Mars varies in length by about 50 sec between perihelion and aphelion.

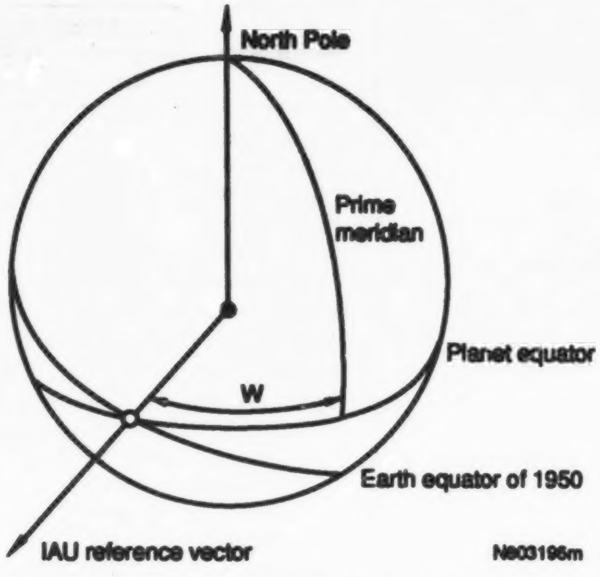

Figure 4-1.- IAU specification of prime meridian.

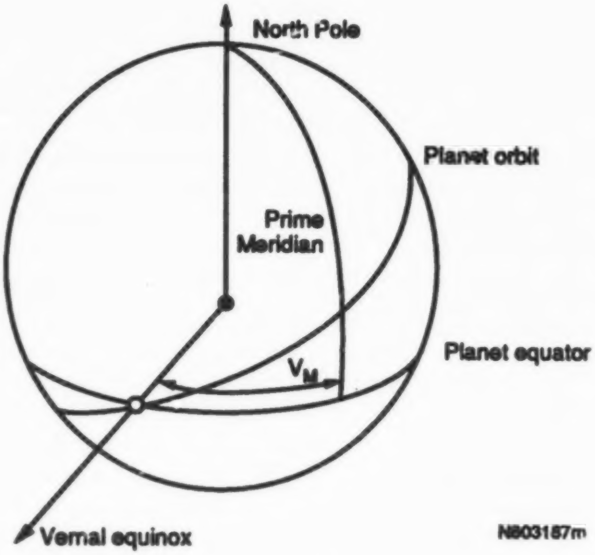

Figure 4-2.- Hour angle of equinox for specifying prime meridian.

Local mean solar time (LMST) is defined similarly, as shown in figure 4-5, by the areocentric right ascension difference between a point on the surface and the fictitious mean Sun (FMS). The FMS is a mathematically defined concept, a point that moves on the celestial equator of Mars, which represents the average motion of the Sun over

---

[4] The Mars Observer navigation team has adopted the Balmino 18x18 field (Balmino et al., 1982) as nominal.

Identification	Areocentric Longitude (deg)	Areocentric Latitude (deg)	Radius (km)	GM (km^3/sec^2)	3σGM %
Hessas Planitia	69.7	-42.	900.	-0.4	30
Isidis Planitia	89.0	12.	240.	0.1	
Utopia Planitia	95.0	42.	700.	0.25	
Elysium Mons	146.5	25.	300.	0.15	
Olympus Mons	226.5	18.	300.	0.6	
Arsia Mons	239.5	-9.	180.	0.15	
Pavonis Mons	247.5	0.	180.	0.15	
Alba Patera	251.0	40.5	450.	0.2	
Ascraeus Mons	256.0	11.	200.	0.15	
Argyre Planitia	317.0	-51.	400.	-0.1	
Hesperida	98.0	-15.	900.	0.1	70
Elysium (West)	110.0	18.	600.	-0.1	
Arcadia	209.0	49.	600.	0.05	
Alba Patera (East)	276.0	39.	660.	0.1	
Valles Marineris	289.0	-4.	540.	-0.03	
Acidalta (West)	310.0	45.	720.	-0.07	
Valles Marineris	332.0	-2.	600.	-0.04	
North Polar Cap	0.0	87.5	540.	0.14	100
South Polar Cap	180.0	-85.0	600.	0.14	

TABLE 4-4.- Mars gravity anomalies and error assessment

the martian year. A similar concept is used to define universal time for the Earth. The right ascension of the FMS is defined by the following equation (Beerer, 1985; Blume, 1986b):

$$\text{R. A. of FMS} = -28.217^\circ + 0.524041^\circ \Delta T_p \quad \text{(deg)}$$

$$\text{where:} \quad \Delta T_p = \text{JED} - 2449200.5$$

$$= \text{JED} - \text{August 1, 1993 00:00 ET}$$

The equation of time (EOT) for Mars is the difference in right ascension between the mean Sun and the true Sun.

$$\text{EOT} = \text{(R. A. of FMS)} - \text{(R. A. of true Sun)}$$

The value of EOT in degrees is usually converted to solar-minutes to give the correction to mean solar time to obtain true solar time. True solar time varies 40 solar min ahead to 51 solar min behind mean solar time. That is, the true Sun varies from 10.0 deg west to 12.8 deg east of the FMS.

The length of a mean solar day (sol) for Mars can be computed from the rotation rate for Mars with respect to its vernal equinox (Michael, 1979) and the rate of motion of FMS. The value obtained is:

$$1 \text{ sol} = 88775.245 \pm .002 \text{ sec}$$

4.5 MARTIAN SATELLITES

4.5.1 Phobos and Deimos Physical Data

The two satellites of Mars, Phobos and Deimos, were discovered by Asaph Hall during the 1877 opposition.

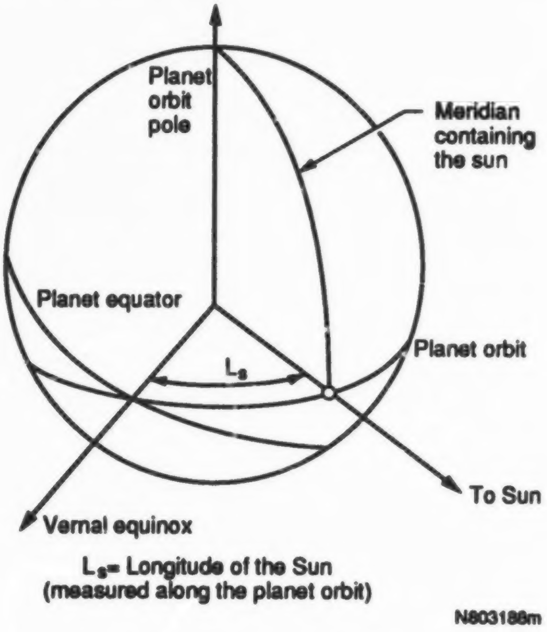
Planet orbit pole
Meridian containing the sun
Planet equator
L_s
Planet orbit
To Sun
Vernal equinox
L_s= Longitude of the Sun (measured along the planet orbit)
N803186m

Figure 4-3.- Longitude of Sun (L_s).

Both satellites are in near-equatorial orbits that are very nearly circular. The orbital radius of Deimos is 6.91 R_M with a sidereal period of 30.30 hr. The Phobos orbital radius is 2.76 R_M with a sidereal period of 7.65 hr. Phobos orbits inside the synchronous orbit radius (6.02 R_M), and it

Season	Epoch at beginning of season		Ls value
Northern Spring	October 9, 1994	2016 ET	0
Northern Summer	April 26, 1995	1042 ET	90
Northern Autumn	October 26, 1995	2157 ET	180
Northern Winter	March 21, 1996	1337 ET	270
Northern Spring	August 26, 1996	1935 ET	0
Northern Summer	March 13, 1997	0956 ET	90
Northern Autumn	September 12, 1997	2121 ET	180
Northern Winter	February 6, 1998	1303 ET	270
Northern Spring	July 14, 1998	1853 ET	0
Northern Summer	January 29, 1999	0911 ET	90
Northern Autumn	July 31, 1999	2044 ET	180
Northern Winter	December 25, 1999	1229 ET	270
Northern Spring	May 31, 2000	1811 ET	0
Northern Summer	December 16, 2000	0824 ET	90
Northern Autumn	June 17, 2001	2007 ET	180
Northern Winter	November 11, 2001	1154 ET	270
Northern Spring	April 18, 2002	1729 ET	0
Northern Summer	November 3, 2002	0739 ET	90
Northern Autumn	May 5, 2003	1930 ET	180
Northern Winter	September 29, 2003	1647 ET	270
Northern Spring	March 5, 2004	1647 ET	0
Northern Summer	September 20, 2004	0653 ET	90
Northern Autumn	March 22, 2005	1853 ET	180
Northern Winter	August 16, 2005	1046 ET	270

TABLE 4-5.- Table of martian seasons

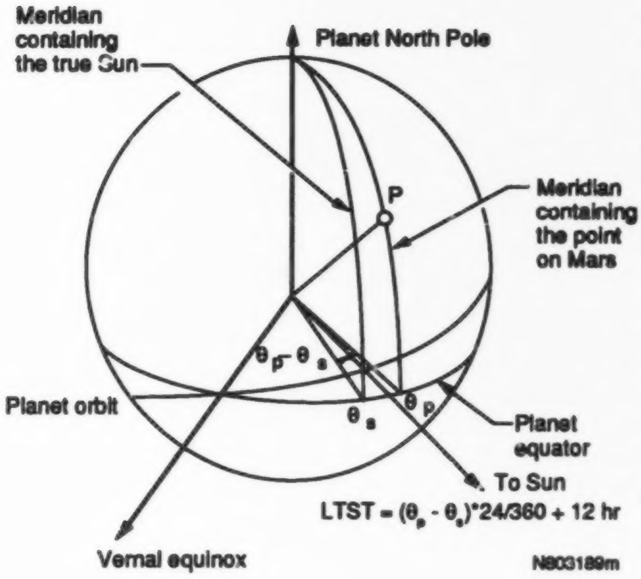
Meridian containing the true Sun
Planet North Pole
P
Meridian containing the point on Mars
$\theta_p - \theta_s$
Planet orbit
θ_s
θ_p
Planet equator
To Sun
LTST = $(\theta_p - \theta_s)$*24/360 + 12 hr
Vernal equinox
N803189m

Figure 4-4.- Local true solar time.

is believed that the orbit is decaying due to tidal action (Born and Duxbury, 1974).

Physical date (Williams et al., 1981; Born, 1974) for the two satellites are shown in table 4-6. The irregular shape of each satellite is approximated by a tri-axial ellipsoid. The rotation of both satellites is synchronous with the long axis pointed toward Mars and the short axis (maximum moment of inertia) normal to the orbit plane.

4.5.2 Satellite Ephemerides

Orbital elements of the satellites (from Born, 1974) are reproduced in table 4-7.

4.6 COORDINATE SYSTEMS

4.6.1 Introduction

Various coordinate systems are used to present engineering and science data during the many phases of a mission. Types of coordinate systems considered are generally cartesian or spherical, but sometimes they are used with

	Phobos	Deimos
Shape (km)	13.5 x 10.8 x 9.4	7.5 x 6.1 x 5.5
GM (km**3/s**2)	(.84 ± .07*E)-3	(.12 ± .01*E)-3
Rotation Rate (deg/day)	1128.592	285.253

TABLE 4-6.- Physical data of Phobos and Deimos

slight variations. A coordinate system is either inertial or time varying. An inertial system of reference is defined by two reference directions fixed in time (e.g., orbit and body poles of a planet of B1950 or of other epoch). A non-inertial frame bases one or both of the reference directions with time varying fixes (e.g., of date quantities). The conventional method of coordinate system definition includes specifying the origin, the x-y plane, and the reference directions. This method will be employed throughout this section.

4.6.2 Mars-Centered Coordinate Systems

Generally, Mars-centered coordinate systems are defined relative to the Mars mean axis of rotation and various definitions of the x-axis or longitude.

(Since the IAU does not define the mean orbit poles of planets, the coordinate systems built on the Mars vernal equinox and pole given in section 4.5.2.1 must rely on additional independent mean orbit pole specifications, such as made by Sturms, 1971.)

4.6.2.1 Mars Equator and Equinox of Epoch

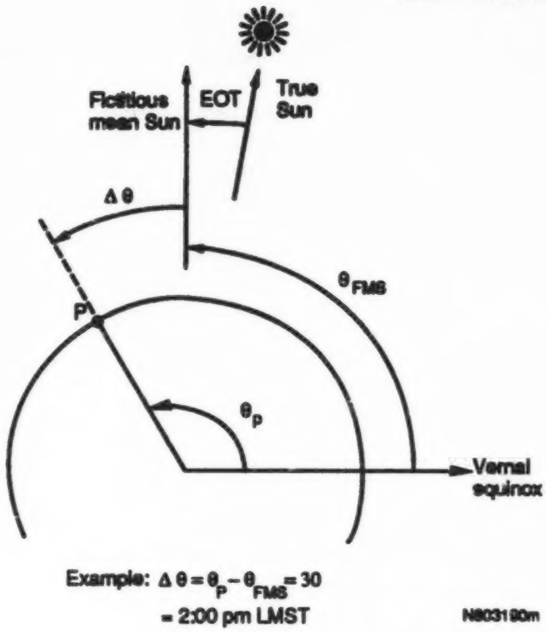

Figure 4-5.- Local mean solar time definition.

This coordinate system is an inertial reference and is defined by the orientations of the Mars mean body pole and mean orbit pole at a given epoch. This is a primary coordinate system used to represent trajectories. The equatorial plane is the x-y plane of this coordinate system. The z-axis is in the body pole direction and the x-axis is in the direction of the vernal equinox (ascending node of Mars orbit in the Mars equator). Spherical coordinates for this system are radius, declination, and right ascension.

4.6.2.2 Mars Equator and Prime Meridian of Date

This is the standard body-fixed rotating coordinate system with the z-axis in the pole direction and the x-axis along the direction of the prime meridian vector (a vector in the equatorial plane from the center of the planet to the prime meridian). Spherical coordinates for this system are radius, areocentric latitude, and areocentric longitude (measured eastward).

Element	Phobos	Deimos
a (km)	9378.529 ± 0.01	23458.906 ± 0.03
e	.0150 ± .0001	.00080 ± .0001
i (deg)	1.04 ± 0.012	2.79 ± 0.02
Ω (deg)	100.509 ± 0.8	10.913 ± 0.2
ω (deg)	269.873 ± 0.9	235.625 ± 7
M_e (deg)	311.818 ± 0.36	232.565 ± 7
$\lambda_e = \Omega + \omega + M_e$ (deg)	322.20 ± 01	118.9 ± 0.1
n (deg/day)	1128.4069	285.1438
$\dot{\Omega}$ (deg/day)	-0.43744	-0.0181
$\dot{\omega}$(deg/day)	0.87481	0.03610
$\overline{n} + \dot{\Omega} + \dot{\omega}$ (deg/day)	1128.84430 ± .0001	285.16178 ± 0.0001

Note: Epoch JD = 2441266.500, November 11, 1971. Angles referred to Mars true equator and vernal equinox of date.

TABLE 4-7.- Orbit of Phobos and Deimos

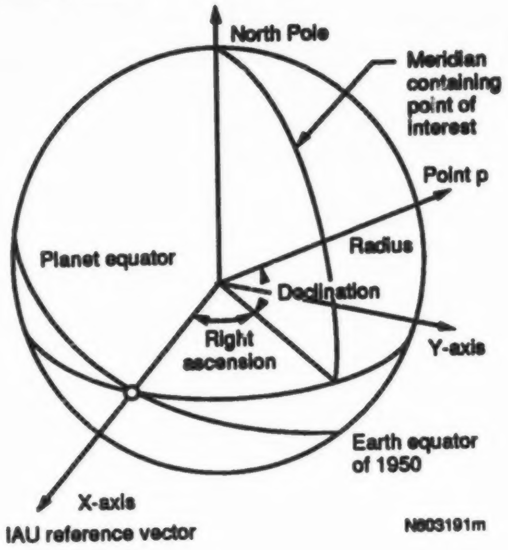
North Pole
Meridian containing point of interest
Point p
Radius
Planet equator
Declination
Right ascension
Y-axis
Earth equator of 1950
X-axis
IAU reference vector
N803191m

Figure 4-6.- Mars mean equator and IAU-vector of epoch coordinate system.

4.6.2.3 Mars Mean Equator and IAU-Vector of Epoch (or Date)

This inertial coordinate system, shown in figure 4-6, is defined by the mean equator of Mars of epoch (or date) and the standard Earth equator of B1950. The x-y plane is the Mars equatorial plane. The x-axis is defined by the ascending node of Mars equator of epoch (or date) on the standard Earth equatorial plane. This unit vector (see fig. 4-1) is used in the IAU definition of the prime meridian and henceforth will be termed as IAU-vector in this document. Z-axis is in the direction of the Mars north pole.

4.6.2.4 Areographic Coordinate System

This cartographic coordinate system is originally used to define the latitude and longitude of surface features on Mars. The cartesian reference of this coordinate system is the same as the body fixed (equator and prime meridian) system. However, the definition of latitude and longitude differs from the standard spherical system definition because this system deals with an oblate planet rather than a spherical one. It refers to the oblate spheroid reference surface as given in section 4.4.1. The areographic altitude instead of the radius from the center of planet is used for coordinate specification. A pictorial of the system is shown in figure 4-7. Specifically, the following coordinates have been used:

Areographic altitude = Distance from the planet surface point along the local vertical of the planet to the point of interest.

Areographic longitude = Measured in the same way as a spherical coordinate, but it is measured westward from the prime meridian direction.

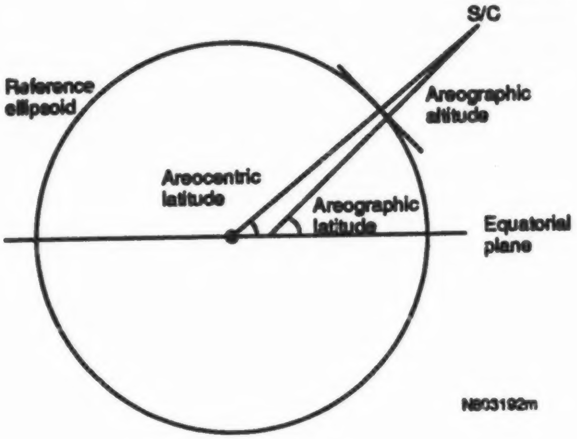
S/C
Reference ellipsoid
Areographic altitude
Areocentric latitude
Areographic latitude
Equatorial plane
N803192m

Figure 4-7.- Areographic coordinate system.

Areographic latitude = Angle formed by the local normal and the equatorial plane.

4.6.2.5 In-Orbit Radial-Crosstrack-Downtrack System

During the orbiting phase of a mission, orbit determinations are made using the Radial-Crosstrack-Downtrack coordinate system. The system is defined by the instantaneous areocentric position and velocity of the spacecraft. The radial vector from Mars to the spacecraft is the radial-axis. The crosstrack axis is aligned with the spacecraft orbit pole and the downtrack-axis is chosen to complete the right-handed orthogonal system. Figure 4-8 displays the system.

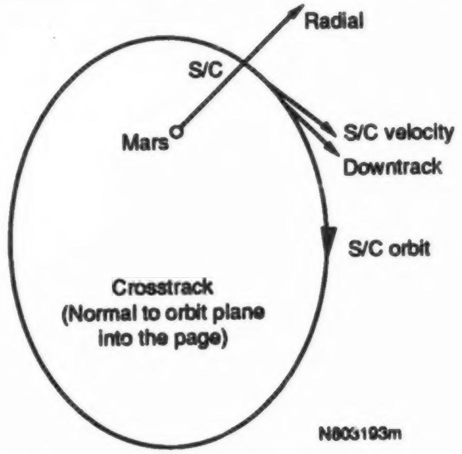
Radial
S/C
Mars
S/C velocity
Downtrack
S/C orbit
Crosstrack
(Normal to orbit plane
into the page)
N803193m

Figure 4-8.- In-orbit radial-crosstrack-downtrack coordinate system.

4.6.3 Spacecraft-Centered Reference System

4.6.3.1 Orbital Phases Nadir Coordinate System

This "orbital reference coordinate system" is used to define instrument pointing requirements during the orbiting phase of a mission. The system is defined with respect to the nadir direction and the spacecraft orbital velocity as shown in Figure 4-9.

The nadir direction (+Z axis) has been defined by the line passing through the spacecraft perpendicular to the Mars mapping reference spheroid. The y-axis is chosen normal to the nadir and velocity vector (cross product of Z vector and velocity). The x-axis is chosen to complete the orthogonal right handed system. The cone and clock angles are the polar coordinates of the object observed with the clock angle measured clockwise in the longitude.

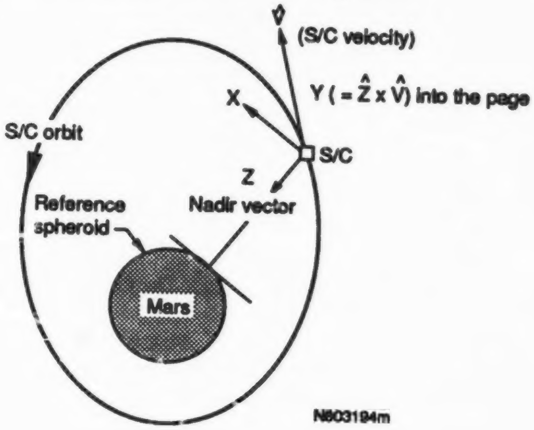

Figure 4-9.- Nadir coordinate system.

4.7 REFERENCES

Astronomical Almanac; 1986: Her Majesty's Stationary Office, London.

Balmino, G. et al.; 1982: Gravity field of Mars in Spherical Harmonics Up To Degree and Order Eighteen. J. Geophys. Res., vol. 87, p. 9735.

Beerer, J. G.; 1985: Locating the Fictitious Mean Sun at Mars. JPL IOM 312/85.1-31, Feb. 27.

Blume, W. H.; 1986a: MASL Inputs for New Martian North Pole and Prime Meridian. JPL IOM 312/85.5-2378, Feb. 3.

Blume, W. H.; 1986b: Computing the Fictitious Mean Sun for Mars and Defining Martian Time Scales. JPL IOM 312/85.5-2397, Feb. 27.

Born, G. H. and Duxbury, T. C.; 1974: The Motion of Phobos and Deimos from Mariner 9 TV Data. Celestial Mechanics, vol. 12, p. 77.

Born, G. H.; 1974: Mars Physical Parameters As Determined From Mariner 9 Observations of The Natural Satellites and Doppler Tracking. J. Geophys. Res., vol. 79, pp. 4837-4844.

Christensen, E. J.; and Balmino, G.; 1979: Development and Analysis of a Twelfth Degree and Order Gravity Model for Mars. J. Geophys. Res. vol. 84, p. 7943.

Christensen, E. J.; and Williams, B. G.; 1978: Mars Gravity Field Derived from Viking-1 and Viking-2. Paper 78-1432, AIAA/AAS Astrodynamic Conference, Aug.

Davies, M. E. et al.; 1983: Report of the IAU Working Group on Cartographic Coordinates and Rotational Elements of the Planets and Satellites: 1982. Celestial Mechanics, vol. 29, pp. 309-321.

Davis, M.E. et al.; 1986: Report of the IAU/IAG/COSPAR Working Group on Cartographic Coordinates and Rotational Elements of the Planets and Satellites: 1985. Celestial Mechanics, vol. 39, pp 103-113.

Georgevic, R.; 1971: Mathematical Model of The Solar Radiation Force and Torques Acting on The Components of A Spacecraft. JPL Technical Memorandum, Oct. pp. 33-494.

Lieske, J.H.; 1985: Astronomical Constants for Galileo. JPL IOM-314.6-600, Aug. 27.

Michael, W. H.; 1979: Viking Lander Tracking Contributions to Mars Mapping. The Moon and Planets, vol. 20, pp. 149-152.

Report of the IAU/IAG/COSPAR Working Group on Cartographic Coordinates and Rotational Elements of the Planets and Satellites, 1985.

Seidelmann, P.K.; 1977: Numerical Values of the Constants of the Joint Report of the Working Group of the IAU Commission 4. Celestial Mechanics, vol. 16, pp. 165-177.

Sjogren, W.; 1985: Mars Gravity Anomalies. JPL IOM 314.10-560, Jet Propulsion Laboratory, Apr. 4.

Standish, E.M.; 1982: Orientation of JPL Ephemerides, DE200/LE200, to the Dynamical Equinox of J2000. Astro. and Astrophy., vol. 114, pp. 297-302.

Sturms, F.S.; 1971: Polynomial Expressions for Planetary Equators and Orbit Elements With Respect to the Mean 1950.0 Coordinate System. NASA Technical Report 32-1508.

Supplement to The Astronomical Almanac, 1984.

Sweetser, T.; 1988: Personal communication. Jet Propulsion Laboratory.

Williams, B.G.; Callahan, J.D.; Hildebrand, C.E.; and Duxbury, T.C.; 1981: Improved Determination of the Phobos and Deimos Masses from Viking. Presentation at fall meeting of the American Geophysical Union (abstract G2-1-A-11), San Francisco, Dec.

Yen, C.L.; and Blume, W.H.; 1986: Mars Observer: Planetary Constants and Models. Preliminary, JPL document D-3444, Jet Propulsion Laboratory, Pasadena, California, July.

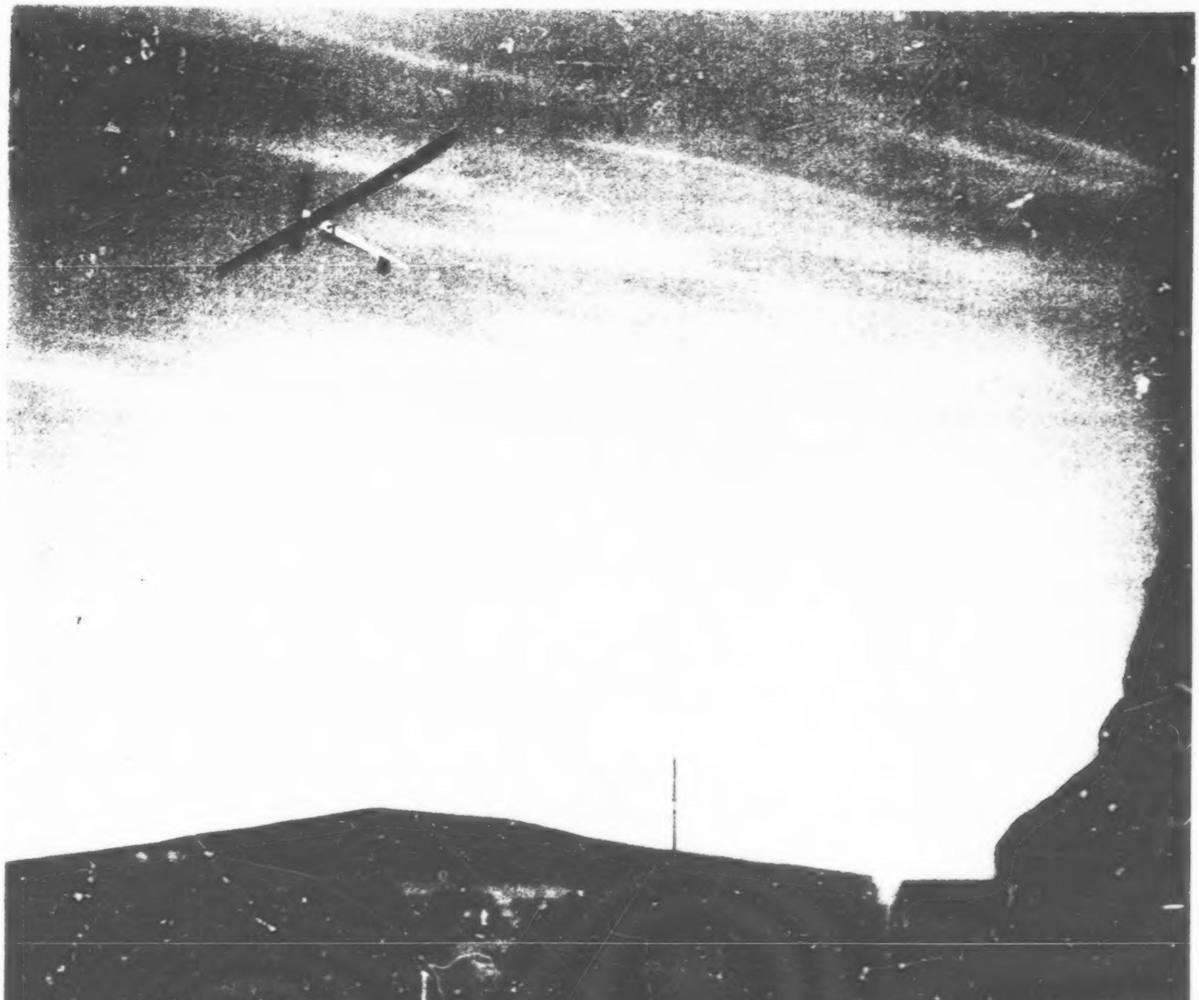

Artwork by Pat Rawlings; Eagle Engineering

ORIGINAL PAGE
COLOR PHOTOGRAPH

1. Report No.
NASA TM 100470

2. Government Accession No.

3. Recipient's Catalog No.

4. Title and Subtitle
Environment of Mars, 1988

5. Report Date
October 1988

6. Performing Organization Code

7. Author(s)
David I. Kaplan, Compiler

8. Performing Organization Report No.
S-587

10. Work Unit No.
075-01-00-00-72

9. Performing Organization Name and Address
Lyndon B. Johnson Space Center
Houston, Texas 77058

11. Contract or Grant No.

13. Type of Report and Period Covered
Technical Memorandum

12. Sponsoring Agency Name and Address
National Aeronautics and Space Administration
Washington, D.C. 20546

14. Sponsoring Agency Code

15. Supplementary Notes

16. Abstract

This document provides a compilation of scientific knowledge about the planet Mars. Information is divided into three categories: atmospheric data, surface data, and astrodynamic data.

The discussion of atmospheric data includes the presentation of nine different models (profiles of density, temperature, etc.) of the Mars atmosphere. Also discussed are martian atmospheric constituents, winds, clouds, and solar irradiance. The "great" dust storms of Mars are presented.

The section on Mars surface data provides an in-depth examination of the physical and chemical properties observed at the two Viking landing sites. Bulk densities, dielectric constants, and thermal inertias across the planet are then described and related back to those specific features found at the Viking landing sites.

The astrodynamic materials provide the astronomical constants, time scales, and reference coordinate frames necessary to perform flightpath analysis, navigation design, and science observation design.

17. Key Words (Suggested by Author(s))
Mars
Mars atmosphere
Mars surface
Mars astrodynamics
Mars environment
Mars models

18. Distribution Statement
Unclassified - Unlimited

Subject Category: 88

19. Security Classif. (of this report)
Unclassified

20. Security Classif. (of this page)
Unclassified

21. No. of pages
71

22. Price*

*For sale by the National Technical Information Service, Springfield, Virginia 22161

JSC Form 1424 (Rev Nov 75)